R-04-76

Alternative DFN model based on initial site investigations at Simpevarp

C Darcel, Itasca Consultants SA

P Davy, O Bour, J-R De Dreuzy
Géosciences Rennes

December 2004

Svensk Kärnbränslehantering AB
Swedish Nuclear Fuel
and Waste Management Co
Box 5864
SE-102 40 Stockholm Sweden
Tel 08-459 84 00
+46 8 459 84 00
Fax 08-661 57 19
+46 8 661 57 19

ISSN 1402-3091
SKB Rapport R-04-76

Alternative DFN model based on initial site investigations at Simpevarp

C Darcel, Itasca Consultants SA

P Davy, O Bour, J-R De Dreuzy
Géosciences Rennes

December 2004

Abstract

In this report, we provide a first-order analysis of the fracture network at the Simpevarp site.

The first order model is the fracture distribution function, noted, fdf, which provides the number of fractures having a given orientation and length, and belonging to a given volume of observation. The first-order distribution model does not describe higher-order correlation between fracture parameters, such as a possible dependency of fracture length distribution with orientations. We also check that most of the information is contained in this 1st-order distribution model, and that dividing the fracture networks into different sets do not bring a better statistical description.

The fracture distribution function contains 3 main distributions: the probability distribution of fracture orientations, the dependency on the size of the sampling domain that may exhibit non-trivial scaling in case of fractal correlations, and the fracture-length density distribution, which appears to be well fitted by a power law. The main scaling parameters are the fractal dimension and the power-law exponent of the fracture length distribution. The former was found to be about equal to the embedding dimension, meaning that fractal correlations are weak and can be neglected in the DFN model. The latter depends on geology, that is either lithology or grain size, with values that ranges from –3.2 for granite-like outcrops to –4 for diorite or monzodiorite outcrops, as well as for the large-scale lineament maps.

When analyzing the consistency of the different datasets (boreholes, outcrops, lineament maps), we found that two different DFNs can be described: the first one is derived from the fdf of the outcrop with fine-grained size lithology, and is valid across all scales investigated in this study, from the highly-fractured cores to large-scale maps; the second one is derived from the fdf of the outcrops with coarse-grained size lithology, and is found consistent with cores that present the smallest fracturing intensity. The latter model is not found to hold at large scale, which implies a transition scale above which the distribution parameters should change.

Contents

1 Introduction

The objective of this study is first to perform an analysis of the fracture systems observed on the Simpevarp site, and to deliver a conceptual 3D fracture network model with statistical distributions types and corresponding parameters derivations. The DFN model is based on the analysis of all available datasets (boreholes, outcrops, and large-scale maps), which are each representative of both local conditions and a given scale range (Figure 1-1). Considering the large heterogeneity of geological rocks, of fracturing processes, and thus of the resulting fracture networks, it is illusive to find a single model that can encompass all data at all scales. The DFN is thus the most likely model through scales. But we also discuss all kind of differences, or variability, which can be revealed from the available dataset.

Despite the exceptional fracture database, if compared to other studies, it is not possible to constrain some basic elements of the fracture distribution, like for instance the fracture shape. We thus assess the simplest description of the fracture system (first order description), which provides the number of fractures, present within a given volume of characteristic length L, that have a typical size l and an orientation (θ,φ). When dealing with the stereology problem – i.e. the way to extract a 3D distribution from 1D or 2D ones – we assume that fractures have a planar disc-shape.

This density description is fundamentally scale dependent. For building a first order fracture network model, the presence of fractures over a large range of scales and also the absence of any obvious characteristic length scale are two arguments in favor of testing power laws first. Such a model for fracture lengths coupled with a fractal fracture density distribution is characterized by two scaling exponents, the power law length exponent noted a and the fractal dimension noted D plus a term α that fixes the density at a given scale of observation /Bour et al. 2002/. The approach has been recently successfully applied to an analysis of the fracture system of the Äspö HRL /Darcel, 2003/.

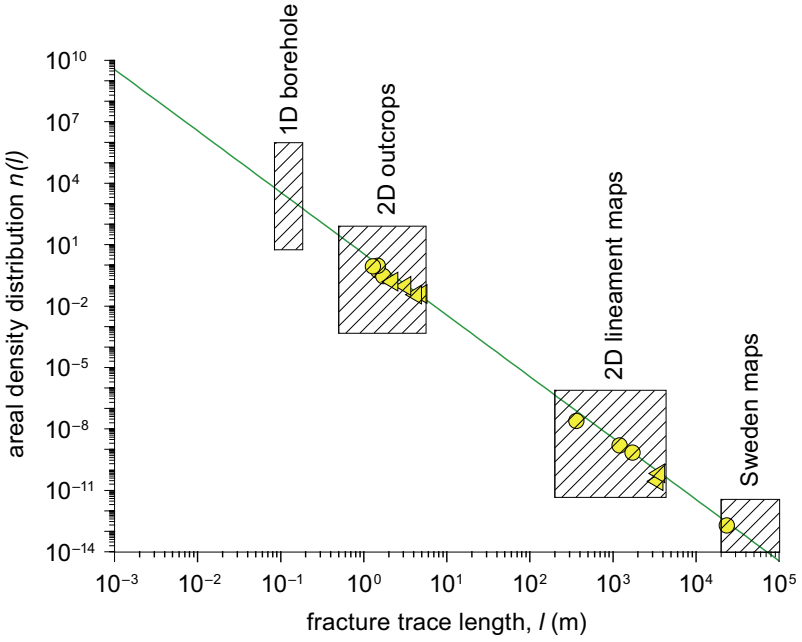

Figure 1-1. *Schema illustrating the range of scales covered by the available datasets.*

Although it catches fundamental internal characteristics of the fracture system, the first order model remains a simplification of the real fracture system complexity. Indeed, the fracture parameters can depend on each other or vary in correlation with variations in lithology. Nevertheless, making the exercise to define a mean DFN model is useful to precise the nature and extent of this variability in DFN parameters. The first order multiscale approach, supplemented by the investigation of variability, is therefore most appropriate for the study of "inherently multiscale" fracture networks.

The work presented here is mainly directed towards the first order characterization, and its own possible variability from a dataset to another. We especially focus on the laws that make the statistical model consistent through scales. For different reasons that are explained in the text, the complete fracture population is not divided into distinct fracture sets, but the orientation issue is fully treated in a way consistent with the 1st-order assumption. The analysis is developed from the 2*d* datasets and subsequent length distribution analysis; then all 2*d* datasets are inter-compared before considering the 3*d* scaling model and analysis of consistency between 2*d* and 1*d* information.

The report is organized as follows: the main text contains the general development of the study. To keep it light, full set of figures, notations used and additional information on the methods used are moved in a set of 8 appendices at the end of the report.

In the main part, field observations (Section 2) and available datasets are first reviewed. Then the statistical method used is described in details (Section 3) before entailing analysis of the local dataset (Section 4). In particular methods used to analyze the density distribution function of fractures and to calculate the density scaling parameters are explained in details. The synthesis and multiscale analysis is treated in Section 5.

Since the notations for representing the statistical model are slightly different from the one recommended by SKB, the correspondence between the ones and the others is explained precisely in Appendix 0. Also, a summary of notations and definitions is given. The Appendix 1 gathers a systematic overview of each 2d dataset, presented as some kind of identification sheets (one sheet per dataset, identical layout for each one). To avoid having to much figures in the principal part, stereoplots for both 1*d* and 2*d* datasets are provided in the following Appendix 2. Discrete, contoured, corrected and not corrected Schmidt diagrams are provided, so that the reader can find there all the non interpreted orientation related information, with crude data (discrete plots) and contoured data. The Appendix 3 contains details (and duplicated large figures) related to the analysis in fracture sets made for two outcrops, *ASM000025* and *ASM000205*. The Appendix 4 recalls the fracture intercepts "status" through the definition of fields "open_frac" to "sealed_network". Values of P_{10}, averaged over borehole full extensions, local variations along boreholes, distinction between the sealed or opened fracture intercepts, are provided. Local variations of fracture intensity are also represented in diagrams coupled with rock lithology variations. The Appendix 5 recall the simple method used to simulate fracture orientations during the validation simulations performed. The Appendix 6 contains, for the 1*d* borehole datasets, all the figures arising from the spatial analysis performed by the integral of correlation performed. Finally Appendix 7 compiles different remarks about data understanding and possible contradictions noted.

2 Field observations

2.1 The site investigated

A regional and a local model domain are defined. This corresponds to the largest scale of the DFN model to be built.

The local model area has a size of 3,200 by 7,800 meters, the regional model area has a size of 13 by 21 km. Note that all the data used in the present study (see next section for a complete list) are located within the regional model area. Almost all the boreholes considered are located within the Simpevarp sub area except for boreholes KLX01 and KLX02 which belong to the Laxemar subarea.

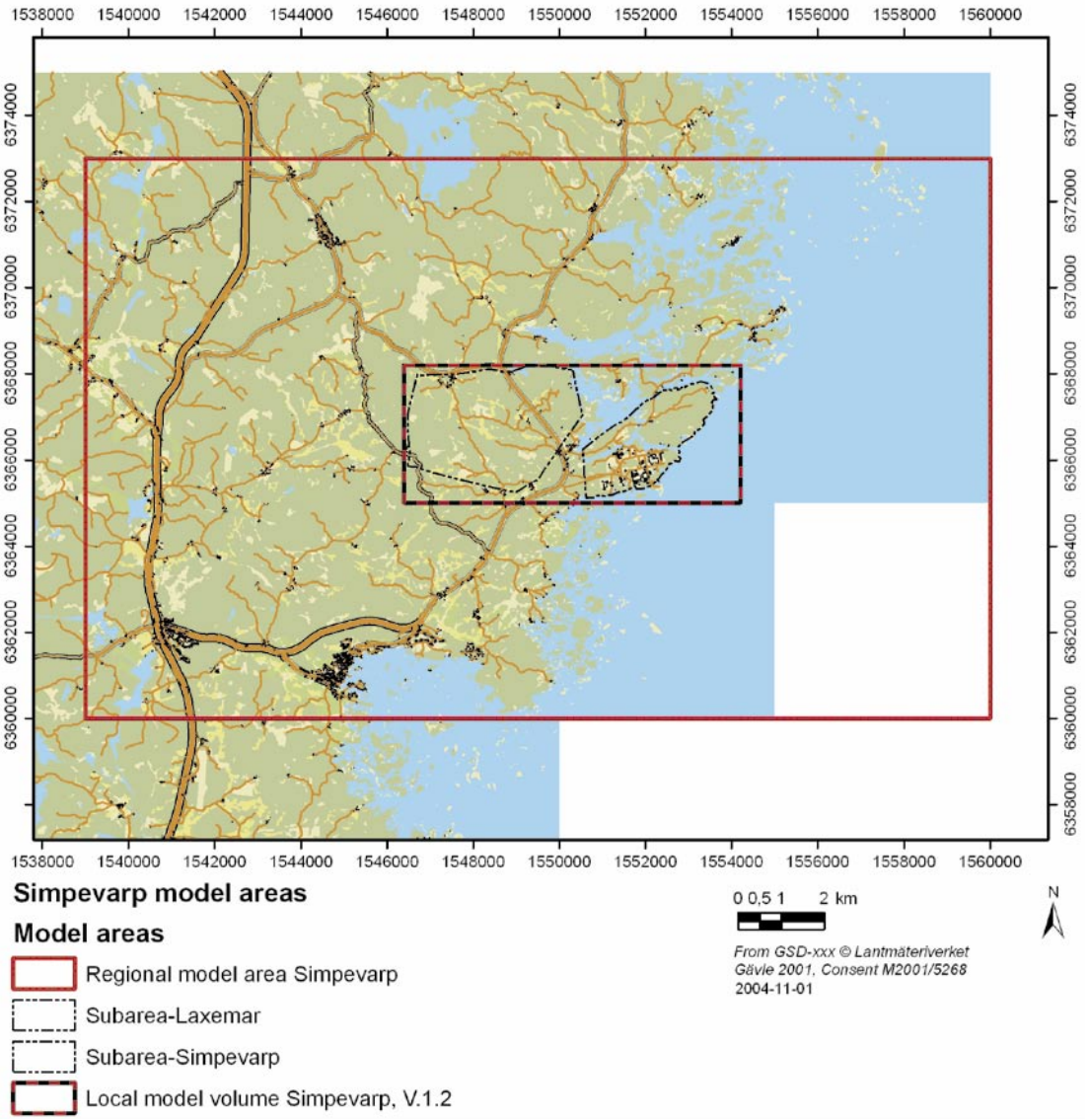

Figure 2-1. *The model limits: regional model (thick red line), subareas of Simpevarp (on the right, dashed grey line) and Laxemar (on the right, dashed grey line) and the local model volume Simpevarp V1.2. (dashed black and red line).*

2.2 Data references

The Table 2-1 contains references to all the data sets mentioned in the report. Three main types of data are available: fracture intercepts along boreholes, referred as “1d-borehole”, fracture traces or lineaments on maps, referenced as “2d-outcrop” or “2d-lineament” depending on the nature of the mapping, and “1d/2d-scanline” corresponding to fracture intercepts positions, and corresponding fracture traces, along outcrop scanlines.

For 1d boreholes an element is a fracture intercept (see below), for 2d maps an element is a fracture trace or a lineament, and for 1d/2d scanlines it corresponds to a fracture intercept plus the fracture trace length.

Note that the full database provided for the analysis is much larger than the one cited in the table below.

Boreholes are core-drilled (named K-) or percussion drilled (named H-).

Table 2-1. References to data sets cited or used in the present work.

Reference name	type
HAV09	1d, borehole
HAV10	1d, borehole
HSH01	1d, borehole
HSH02	1d, borehole
HSH03	1d, borehole
KAV01	1d, borehole
KLX01	1d, borehole
KLX02	1d, borehole
KSH01A	1d, borehole
KSH01B	1d, borehole
KSH02	1d, borehole
KSH03A	1d, borehole
KSH03B	1d, borehole
SDEADM_GOL_OH_GEO_1921	2d, outcrop *ASM000025*
SDEADM_GOL_OH_GEO_1918	2d, outcrop *ASM000026*
SDEADM_GOL_OH_GEO_1915	2d, outcrop *ASM000205*
SDEADM_GOL_OH_GEO_1924	2d, outcrop *ASM000206*
LSM000092	1d/2d scanline
LSM000092	1d/2d scanline
LSM000093	1d/2d scanline
LSM000093	1d/2d scanline
LSM000094	1d/2d scanline
LSM000094	1d/2d scanline
LSM000095	1d/2d scanline
LSM000095	1d/2d scanline
LSM000096	1d/2d scanline
LSM000096	1d/2d scanline
LSM000097	1d/2d scanline
LSM000097	1d/2d scanline

Reference name	type
SDEADM_GV_SM_GEO_2028	2d, Lineament lin_2028
SDEADM_GV_SM_GEO_2027	2d, lineament, lin_2027
lin_topo	2d, lineament

2.3 The four sampled outcrops

2.3.1 Description

The four outcrops are located within the Simpevarp peninsula (Figure 2-2). They cover surfaces comprised between 215 and almost 525 square meters and are representative of different lithologies, from Ävrö granite (code 501044) to fine-grained dioritoid (intermediate magmatic rock, code 501030). Fracture traces have been mapped over the whole surfaces with a lower cut-off length of about 50 cm. In addition, fractures along two ten meters long perpendicular scanlines have been sampled at a lower resolution scale (equal to 20 cm). An overview of data analyses for the outcrops, as well as respective positions of the scanlines on the outcrops, is provided in Appendix 1.

The fracture trace datasets contain detailed geometrical information (position, elevation, strike, dip, length, termination type, aperture, width) as well as rock type, structure, colour and filling material and alteration, for each fracture registered. However, not all the fields are systematically filled.

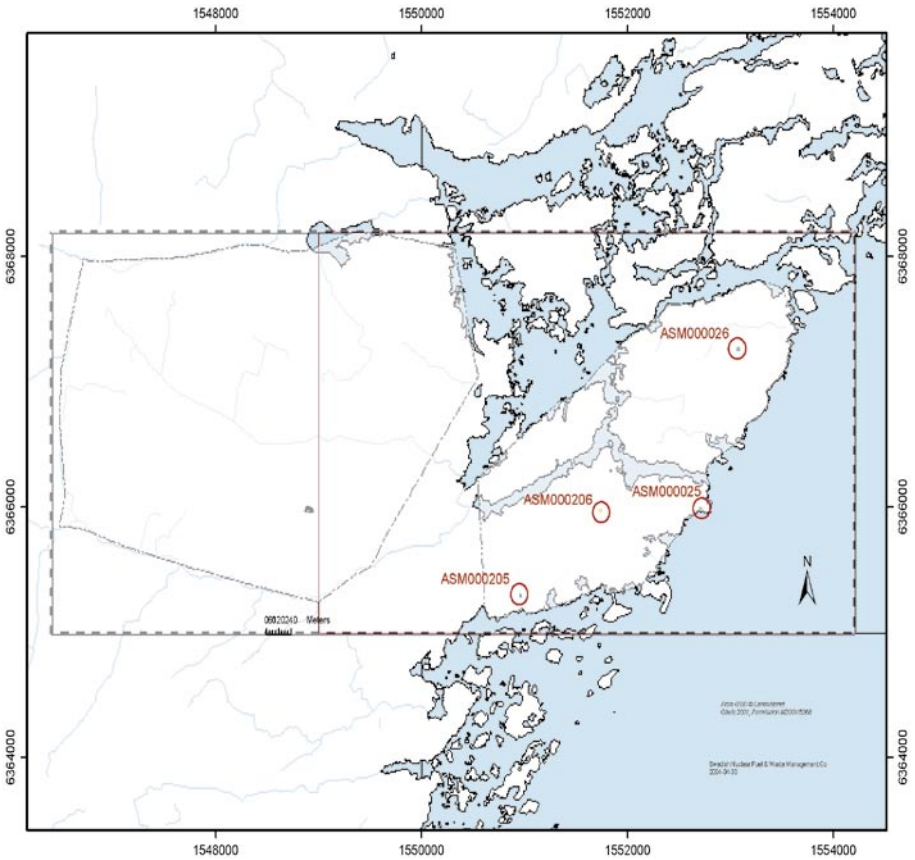

Figure 2-2. *The four outcrops, ASM000025, ASM000026, ASM000205 and ASM000206, spatial localization.*

Direct geological observations on the field complete the dataset information. The apparent density of fracturing is clearly different from one sample to another. In the outcrop *ASM000205* (diorite with very small grain size), we observe a high density of very small fractures, even at scales much smaller than the resolution scale of the mapping (Figure 2-3). A similar observation, although not as striking, can be made on the outcrop *ASM000206*. In contrast, small scale fractures seem to be sparser on outcrops *ASM000025* and *ASM000026* (Figure 2-4). This is apparently correlated to the rock lithology, *ASM000025* and *ASM000026* being characteristic of Ävrö porphyritic granite, and the two remaining rather fine-grained dioritoid.

In terms of fracturing typology, we have observed both faults at different stages of their formation, and other fractures which are likely joints (Figure 2-5). The different types of fractures coexist on all outcrops, even if the faulting process – as opposed to jointing – is especially encountered in the granitic outcrops *ASM000025* and *ASM000026*.

Figure 2-3. *Photographs of the diorite encountered in the outcrop ASM000205 (close to the CLAB), and of the small-scale fracture density.*

Figure 2-4. *Photograph of the outcrop ASM000026, which emphasizes the small density of small fractures in contrast with Figure 2-3.*

Figure 2-5. *Left) An incipient fault propagating on the granite in outcrop ASM000025. We can observe the Riedel-type en-echelon fractures crosscut by the eventual fault. Right) The N10 fracture family of outcrop ASM000206 corresponds to faults with visible offset, although most of the fractures do not present significant offset.*

The orientation distributions seem also to contain a discriminative signature of the fracture pattern (see section on orientations Figure 4-13).

We first have evaluated the fracture mapping of the 4 outcrops with respect to field observations. The sampling appears consistent with observations except for two points:

- Some large structures, straight and well connected, are mapped as several disconnected segments. Detailed field observation shows that these segments are effectively bounded by fractures whose length is smaller than the chosen resolution scale, and thus which are not recorded according to the sampling strategy. Segmenting these fracture zones or not is an arbitrary choice since one could also have considered that all the segments form one large fracture, which is intersected by a few small ones. This sampling strategy would give a larger number of large fractures.
- For some reasons, a few large fractures that clearly exist on outcrops are not mapped, especially along ponds and grass bands, or at the border of pegmatite veins.
- In general, the sampling in conjunction with pegmatite veins is not totally satisfactory. It consists of a number of disconnected fracture segments delimitating (or close to) the vein borders. This obviously produces large correlation in position and orientations since these segments are more or less parallel and forming a large connected fracture zone. These correlations cannot be described by the 1st-order part of the DFN distribution model, and thus should require complex, and even local, 2nd-order constraints to the DFN model. We do not propose to follow this (although it could be done) because the spirit of building a DFN model is to provide a statistical generator for which objects are not, or weakly, correlated two by two. In that sense, it is more consistent to connect these segments first, and to count them as a single well-connected object.

2.4 Borehole observations

The borehole lengths range from a hundred of meters up to a thousand of meters. The mean borehole orientations, taken as the direction defined by the first and last fracture intercept, are mostly close to vertical.

Core observations and borehole logging provide information about rock matrix properties and fractures occurrences and complexity. Indeed, at the core scale, the complexity of the fracture system arises (see Figure 2-6). Some fracture intercepts are clearly identified; some other portions are crushed so that single fracture intercepts cannot be identified. Therefore crush zones are specifically registered (see a Figure 2-6). For instance, the density of fractures within a crush zone is deduced from the size of the crushed blocks. Also, some sealed parts of the fracture system are characterized as “sealed network” instead of well defined and identified single intercepts (ex borehole KSH03A). When fracture intercept identification is possible, the following informations are simultaneously recorded:

- relative position along borehole,
- absolute position (geo-referenced),
- strike and dip of the fracture plane,
- broken or unbroken status,
- sealed to open (with intermediate cases) status,
- confidence level,
- visibility in BIPS,
- mineral filling,
- roughness.

Figure 2-6. *Picture of a cored borehole, KLX01, 1007–1020 meter.*

Note that for cored boreholes, information can be analyzed directly from the cores (Figure 2-6) and also compared to borehole imaging. This adds a level of confidence regarding the reality of some observed fractures (core accidentally broken for instance).

In addition to fracture intercepts, variations in rock lithology, structure and alteration are recorded along the boreholes.

From the available data, it is then possible to evaluate P_{10} (the number of fractures per unit length of core), either for the whole fracture set, or for sub-groups, according to sealed/open status, orientation, rock lithology etc.

2.5 Large-scale/lineament maps

Lineament maps cover the regional scale model area. Three datasets covering almost the same area are available, from simple topographic lineaments up to lineaments that have been checked for a high level of confidence. “Interpreted” and “linked” lineaments (referred as *lin_2027* and *lin_2028*) show the crucial importance of defining a fracture from drawn segments. Indeed these two maps contain exactly the same lineament segments, but with a higher degree of linkage for map *lin_2028*. The topographic lineaments are not linked and seem to have been mapped up to a higher resolution scale. Note that an additional dataset of topographic lineaments covering almost all Sweden is also considered.

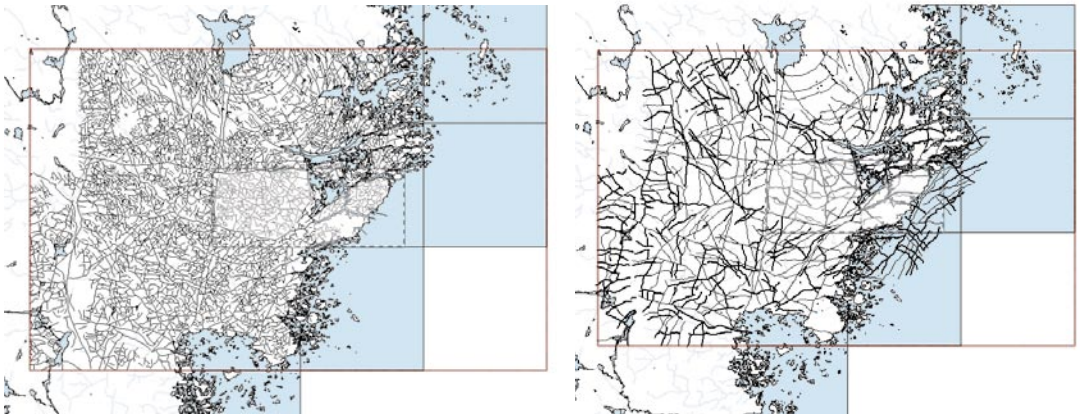

Figure 2-7. *Lineament maps, topographic lineaments (left) and interpreted lineaments (right).*

3 Statistical method

In this paragraph, we present the statistics derived from the datasets that were made available for this report. Basically we calculate the parameters of the 1st-order distribution model which gives the number of fractures whose fracture plane has a typical length in $[l, l + dl]$, orientation angles in $[\theta, \theta + d\theta]$ and $[\varphi, \varphi + d\varphi]$ in a system Σ:

$$n(l,\theta,\varphi,\Sigma)\cdot dl\cdot d\theta\cdot d\varphi = \left\{O_{pdf}(\theta,\varphi)\cdot d\theta\cdot d\varphi\right\}\cdot\left\{n_{ddf}(l)\,dl\right\}\cdot g(\Sigma) \quad (1)^1$$

This definition calls for several remarks:

- A fully-defined fracture distribution model should consider several parameters for defining the fracture plane since a fracture is not supposed to have a simple shape such as a disk. But despite its remarkable completeness, the database does not contain any information that could help us derive a generic 3d fracture shape. The only objective measure of the underlying fracture shape distribution is the length of fracture traces on outcrops or on outcrop scanlines. From a theoretical point of view, a fracture which is mechanically isolated from others in a simple medium is likely to grow as a 2d-ellipse /Cowie, 1998; Cowie and Scholz, 1992/. More complex situations have been studied but, except for a few numerical simulations obtained using massively parallel computers, either the model conditions were extremely simple if not simplistic or the available data were only fracture traces intersecting an observation plane. To our knowledge, there is no theoretical work that could help us to find out the shape of fractures which formed from complex mechanical interactions, in a heterogeneous geological medium, and during several tectonic episodes. We thus consider the fracture length l to be a "typical" fracture size consistent with observed fracture traces. This length fully defines the fracture shape only in the case of disks, an assumption that we will use when reconstructing the 3d fracture distribution model for its convenience. If new information is made available about fracture shape, we can refine this assumption.
- We consider the pair (θ, φ) to be the spherical angles that define the direction of the fracture-plane normal vector. These angles fully define the orientation of the fracture plane only if fractures have a disk shape. O_{pdf} is the probability density function of both orientation parameters.
- $g(\Sigma)$ is the normalization factor due to the dimension (2d for outcrops and maps, something between 1d and 3d for boreholes) and size of the sampling system Σ. $g(\Sigma)$ makes possible the comparison between system of different size. It can take non-trivial form if fractures are clustered in a fractal way. In the following, we may replace Σ by the typical size of the sampling domain noted L.
- n_{ddf} is the density distribution function for fracture length called *lddf* as length density distribution function thereafter. It is defined per unit system size, i.e. per unit volume, per unit area or per unit length, depending on the dimension of the sampling system. n_{ddf} takes account of all sampled fractures whatever their orientations. This is consistent with the 1st-order statistical model that we aim at defining; but this is a bit different from what it is generally done where the statistical parameters are defined for different fracture sets. This point is discussed below.
- $n(l,\theta,\varphi,\Sigma)$ is called the fracture distribution function *fdf* thereafter.

In the rest of this chapter, we describe the methods that we use for deriving the distributions from the database. In the next chapter, we give the results obtained from outcrops, scanlines and boreholes. At last, we give the 3D model(s) that we find consistent with all these results.

[1] The correspondence between our notation and those generally used by SKB is given in Appendix 0.

3.1 Length distribution function

The first analysis is the derivation of a length density distribution function (*lddf*) from a set of fractures[2]. In this paragraph we will detail the procedure that we have used, and which yields results as the one presented in Figure 3-1.

A common method consists in calculating the cumulative function (Figure 3-1, bottom right) which gives the number of observed fracture lengths larger than a given value. The drawback of this function is that it cannot be directly compared to a model distribution of an infinite system. Indeed elements larger than the system size are obviously not taken into account, which means we underestimate systematically the whole cumulative distribution compared to the model function (Figure 3-1). Note that truncation effects due to the finiteness of the sampling window can be even more complex /Laslett, 1982/.

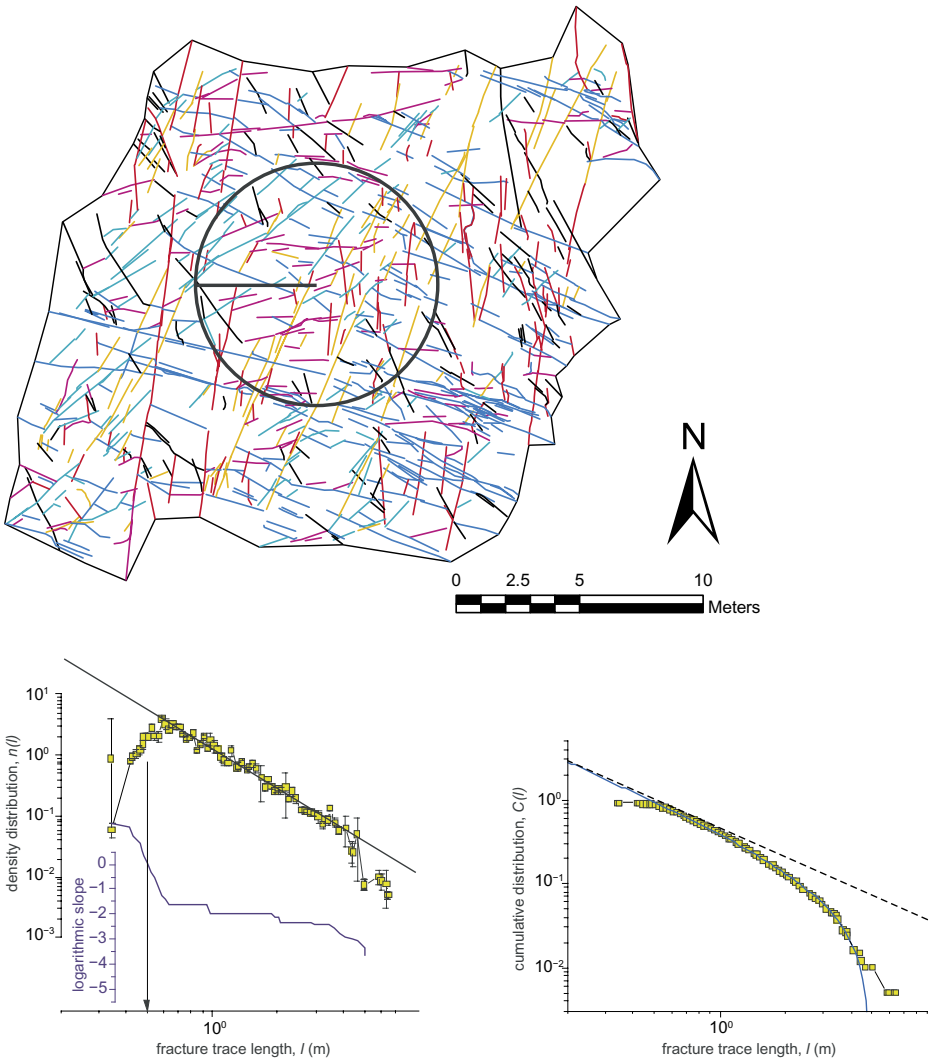

Figure 3-1. *Map of the outcrop ASM000025 (top), calculated fracture distribution per unit area and associated logarithmic slope (bottom left), and cumulative distribution C(l) (bottom right)[3]. Details shown in the map and figures are described in the text.*

[2] Note that it is not the classical probability density function (pdf) since we are interested in evaluating a density function, which gives the number of fracture per unit area, rather than a probability to encounter a fracture over the entire system.

[3] See Appendix 1 for a larger copy of the diagram.

We thus prefer calculating the fracture length density distribution function *lddf*, which is the number of fractures per unit area (for outcrops) whose length ranges in [l, dl][4]. The method that we used was published in /Davy, 1993/. The main "trick" consists in fixing the binning dl so that the number of fractures N within each bin is statistically correct, and that the bin is small enough to consider that the *lddf* $n_{ddf}(l)$ is well approximated by the ratio N/dl/A, where N is the number of fractures, dl the length bin, and A the sampling system area. By varying the bin, we also calculate the standard deviation of each value in the lddf as an indicator of the local variability. Figure 3-1 (middle) shows a bi-logarithmic plot of the *lddf* vs fracture trace length, as well as the logarithmic slope of the *lddf* defined as:

$$\frac{\mathrm{d}\log(n_{\mathrm{ddf}}(l))}{\mathrm{d}\log(l)} \qquad (2)$$

Let study the particular case of *n(l)* is a power law:

$$n_{\mathrm{ddf}}(l) = \alpha\, l^{-a}$$

Then the logarithmic slope is exactly the power-law exponent a, and it can thus be considered as an appraisal of the validity of the power-law assumption.

In the example given in Figure 3-1, the *lddf* is well fitted by a power law whose exponent is about –2.15 ± 0.05, a model which is well validated by the evolution of the logarithmic slope with l (Figure 3-1, bottom left, lowest curve). The power-law model is valid between the resolution scale of the study, arbitrarily fixed at 0.5 m (see arrow in Figure 3-1, bottom left), and a large length scale l_{max}, which is about 5 m. l_{max} is represented on the outcrop by the radius of the circle drawn in the middle of the map. The integral of the power-law fit is then represented on the cumulative distribution function cdf, such as:

$$C_{\mathrm{fit}}(l) = \int_{l}^{l_{\max}} n_{\mathrm{ddf}}(l')\,\mathrm{d}l' \sim \frac{\alpha}{a-1}(l^{-a+1} - l_{\max}{}^{-a+1}) \qquad (3)$$

Figure 3-1 (bottom right) shows that the integral of the density fit still holds for the cumulative distribution if l_{max} is equal to 5 m (solid blue line on the right). The figure also shows that this fit is no more a power law (dashed curve) because of the absence of fracture trace larger than l_{max}. In theory the *cdf* could be used to determine the parameters α, a and l_{max} of the power-law fit, but we do not advise using this method because it assumes that all possible finite-size effects are well modeled by a single parameter l_{max}, which is a very crude assumption even if it works in this example. We thus prefer directly fitting the fracture distribution function to determine the model fit and its parameters.

Note that the determination of the model that will be fitted is a key issue when trying to fit the *lddf*. In this report, we make special emphasis on the power-law fit for reasons that we will explain; but we also check for other distribution model such as the lognormal function and compare for the efficiency of both models to describe the whole dataset including boreholes, outcrops and large-scale lineament maps.

3.2 Density scaling

The complementary characterization is the density term. For the last fifteen years, it has been recognized that fracture density is fractal emphasizing first fracture clustering, and

[4] Actually we calculate the density per unit area in Figure 3-1 to take into account the sampling size. This point is addressed in the next paragraph and generalizes to non-homogeneous systems.

a scale dependency of these spatial correlations /see Bonnet et al. 2001 and references therein/. This has been expressed by /Davy et al. 1990/ who proposed that the total number of fracture of length in [l, l + dl], and in a system of size L can be modeled by the following scaling equation:

$$n(l,L) = \alpha \times l^{-a} \times L^{D}, \quad (4)$$

where $n(l,L)$ and a are resp the fracture distribution function fdf and the length exponent defined in previous section, L the system size, α a density term and D the exponent characterizing the density scaling.

For a homogenous or random repartition of fractures in space, the exponent D (or mass dimension /Bour et al. 2002/) is simply equal to the Euclidean dimension d (d = 1 along a line, = 2 in a plane and = 3 in a volume). When fractures are clustered in space through a fractal organization then the exponent D is less than d (the cluster do not fill the space and the effect is reproduced through scales), and consequently $n(l,L)$ scales as $L^D < L^d$. The apparent fracture density (number of fractures per unit volume, area or length, defined as $n(l,L)/L^d$) is then decreasing while increasing scale. The value of D represents the degree of clustering in the system: the smaller the value of D, the larger the fracture clustering, valid over the whole range of scales were D is defined (Figure 3-2).

As it will be developed in a next section, knowing the value of fractal exponent D is necessary for the reconstruction and normalization of the fracture distribution function from datasets coming from different samples sizes (areas in 2d).

The density scaling thus defined describes the evolution of the number of elements (fractures) found in a system of given size. Therefore the fractal dimension is measured from the set of fracture defined as individual elements, independently of their own sizes. We then chose to characterize the fracture positions trough their barycenter positions. Note that however “all points of fracture plane are possible a priori candidates: we take the fracture barycenter as the most neutral position compared to fracture tips” /Bour et al. 2002/. For 1d datasets, fractures positions are non ambiguous, simply defined as the fracture intercepts.

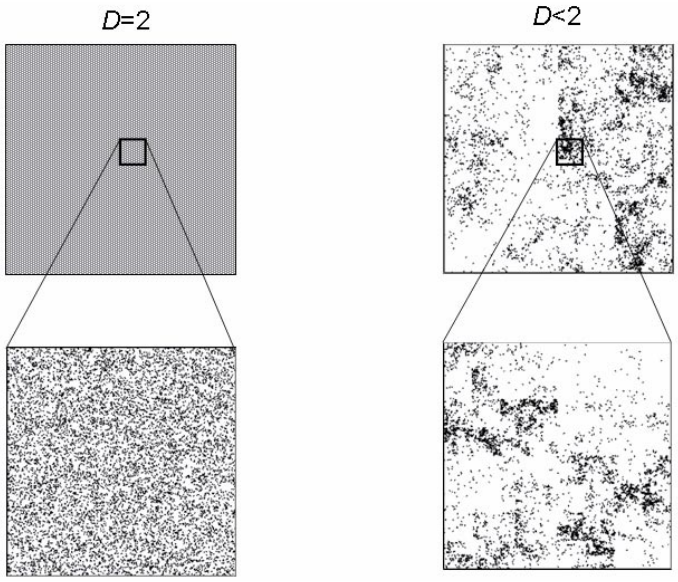

Figure 3-2. *Illustration of fractal clustering over a discrete set of points, comparison of a uniform on the left and a fractal case on the right.*

Several methods permit to measure the fractal dimension of an object (box-counting, mass method, correlation integral, multifractal analysis). Since they refer to different geometrical properties of the object measured, they do not necessarily provide the same value of fractal dimension. Details on the different methods used and different fractal dimensions obtained for fracture systems can be found in /Bonnet et al. 2001/. For the fractal dimension of a natural fracture set, it has been demonstrated that the best method to characterize the system is performed through the measure of the pair correlation integral. For a dataset made of discrete points, the pair correlation function $C_2(r)$ is defined as

$$C_2(r) = 2N_p(r)/[N(N-1)] \tag{5}$$

where $N_p(r)$ is the number of pairs of points whose distance is less than r and N the total number of points in the system. The product $N(N–1)$ is a simple normalization factor, such that, when the variable r equals the distance R between the two furthers apart points of the dataset, then $C_2(r)$ simply reaches 1. The subset "2" is related to correlation of order 2, that is upon pairs of points. The generalized integral of correlation $C_n(r)$ is based on distance statistics on n-plets sets of points /Hentschel and Procaccia, 1983/. It follows then that D_2, called the correlation- or mass dimension, simply called the fractal dimension in the following, is equal to:

$$D_2 = \lim_{r \to 0} \frac{\log C_2(r)}{\log r}$$

Note that in the case of point datasets, mass dimension and correlation dimension are equivalent. However the correlation integral method avoids finite size effects due to finiteness of the datasets and is therefore recommended /Bonnet et al, 2002; Bour et al, 2002/.

In the following we will use simply the term "fractal dimension" for designating the correlation/mass dimension.

In practice, the method efficiency is sensitive to the number of points in the dataset, and to the shape and size of the sampling area. To take account of possible boundary effects due to the area shape, we propose the following procedure:

- The fracture dataset is represented by the barycenter positions in a defined sampled zone.
- From the original dataset we build a new dataset by randomly re-distributing the points over the delimited sampling area.
- The integral of correlations are calculated for both the real and random datasets, leading to $C(r)_{natural}$, noted $C(r)$, and $C(r)_{random}$, noted $C(r)_{ra}$.
- The ratio $C(r)_{random}/C(r)$ is supposed to vary as r^{d-D}, cleared from finite size effects.
- Fractal dimensions are eventually measured directly from the ratios $C(r)_{ra}/C(r)$.

An example of the results is given in Figure 3-3. In the case of a randomized set of points (blue curve in Figure 3-3), $C(r)$ has the expected power-law slope of $D = 1$, up to the distance where finite size effects become dominant. Then the slope slowly decreases and tends to zero when the distance r reaches the system size. This finite-size effect, which exists for both randomized and real sets, is about to be corrected by the applied procedure (left graph in Figure 3-3).

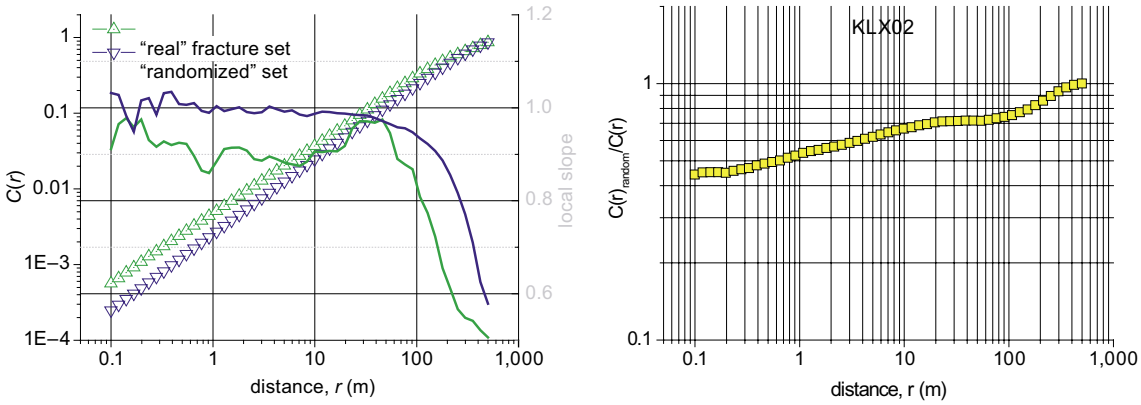

Figure 3-3. *Left: C(r) calculated for dataset KLX02, for all the fracture intercepts (green) and all the fracture intercepts randomized (blue). The right axis and the solid curves give the local "logarithmic slope" of C(r) that is directly comparable to a power-law exponent. Right: Evolution of the ratio $C(r)/C_{random}(r)$ as a function of scale. In this case, the finite-size effect are about to be corrected.*

3.3 Orientation distributions, and fracture sets

The orientation distribution is explicitly taken into account in the statistical model via the term $O_{pdf}(\theta, \varphi)$, which will be given in the next sections. However this parameter directly addresses two important issues for building the eventual DFN model: (i) the subdivision into different fracture datasets, (ii) the correlation between fracture orientations and other parameters such as length distribution or density scaling.

As a preliminary statement, we stress that the 1st-order statistical model is not inconsistent with a subdivision in fracture datasets: each dataset can be described by an equation similar to (1), the general DFN being the sum of these individual components. There are several arguments for subdividing the fracture into several datasets. If the dataset are statistically different, it can be difficult to find a unique mathematical solution that encompasses these differences. For instance, if the datasets have a different scaling, the general DFN should exhibit different scaling regimes, each of them dominated by a particular dataset. The knowledge of the transitional scales is thus an important parameter of the DFN model. Moreover, if the datasets are mechanically independent, it should be useful to analyze the flow properties for each dataset.

- First of all, the subdivision into fracture datasets cannot be made on the orientation information only. Tectonic or geologic arguments should be used to really achieve a sound and useful subdivision. In the example below based on fault growth experiments made in the tectonic laboratory in Rennes, we show that faults with different orientations are growing concomitantly, and that even arguments based on fault termination cannot be unambiguously used to determine a relative chronology. During our short visit of the different outcrops, we cannot conclude that each orientation set is independent of the others – the reverse is likely to occur.
- The physics of fracture growth is nothing but the superposition of subparallel fracture families at different stages of the tectonic history. On the contrary, the main fault statistic features, such as power-law scaling, are supposed to result from the complex interactions between faults of different orientations. At least this is what fault-growth experiments emphasize (see Figure 3-4, /Davy et al. 1990, 1995; Schueller, 2004/).

- Since the orientation remains a basic parameter of the 1st-order DFN model, one takes a full advantage of using different fracture sets only if the subdivision involves other parameters than orientation. To our knowledge, the main determinism on subdividing fractures into different sets remains orientation.
- The main argument in subdividing fractures in different sets is that the scaling factors in length and density (the terms $n_{ddf}(l)$ and $g(\Sigma)$ in equation (1)) are different. In the other hand, deriving such scaling laws require a large number of data, which make impossible any sound statistical analysis in sparse fracture sets. In the next figures, we subdivide fractures of outcrops ASM000025 and ASM000205 in 3 groups by using an orientation criterion (described in Appendix 3); then we calculate the length density distribution $n_{ddf'}(l)$ for each subset. For both outcrops, it is difficult to extract a scaling tendency for the subset that contains the smallest number of fractures. This well illustrates the difficulty of dealing with sparse fracture subsets. For the two other subsets, the length distribution has a scaling trend comparable with the whole fracture set. Even if this result has to be validated with larger fracture sets, this seems to show that the subdivision into independent fracture sets is not really necessary and even more may lead to irrelevant statistical analysis. We recall that this does not mean that we neglect the orientation distribution; but we restrict the analysis to the determination of the orientation probability distribution $O(\theta, \varphi)$ in equation (1).

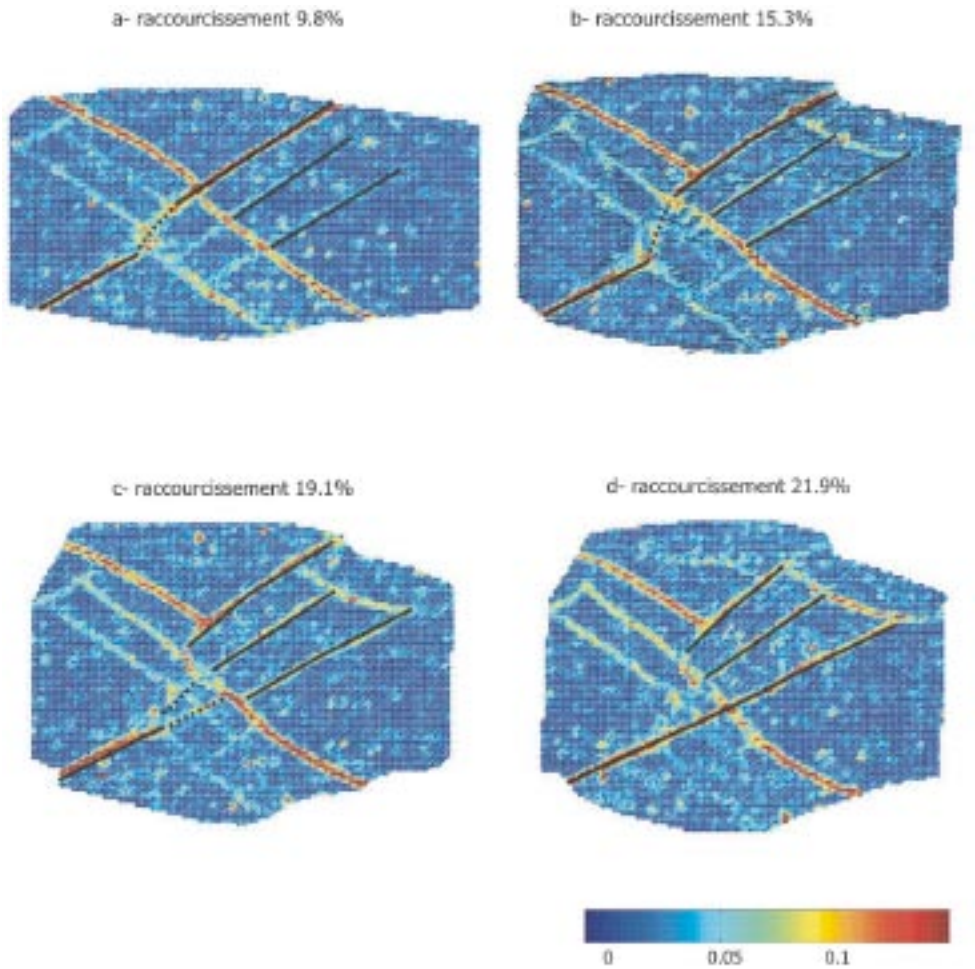

Figure 3-4. *Top-view of 4 stages of a sandbox experiment, showing the active deformation and related faults in a sand layer. The applied deformation is an E-W compression with N-S free boundary. The color scale gives the deformation intensity. The fault extending from NW to NE remains active all along the deformation, while it is clearly offset by the SW-NE fractures. Experiments have been made by Sylvie Schueller for her PhD /Schueller, 2004/.*

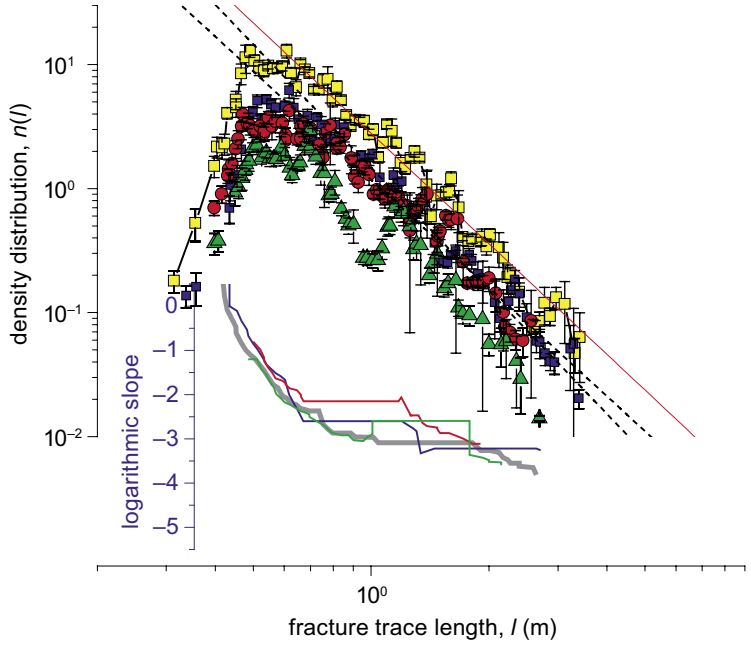

Figure 3-5. *Fracture length density distribution for the original fracture set of the outcrop ASM205 (yellow squares) and for three subsets (blue squares, red circles and green triangles). The power-law scaling exponent a is –2.9 and –3.2 for the two first subsets (to be compared to –3.0 for the original fracture set), and cannot be determined for the latter.*

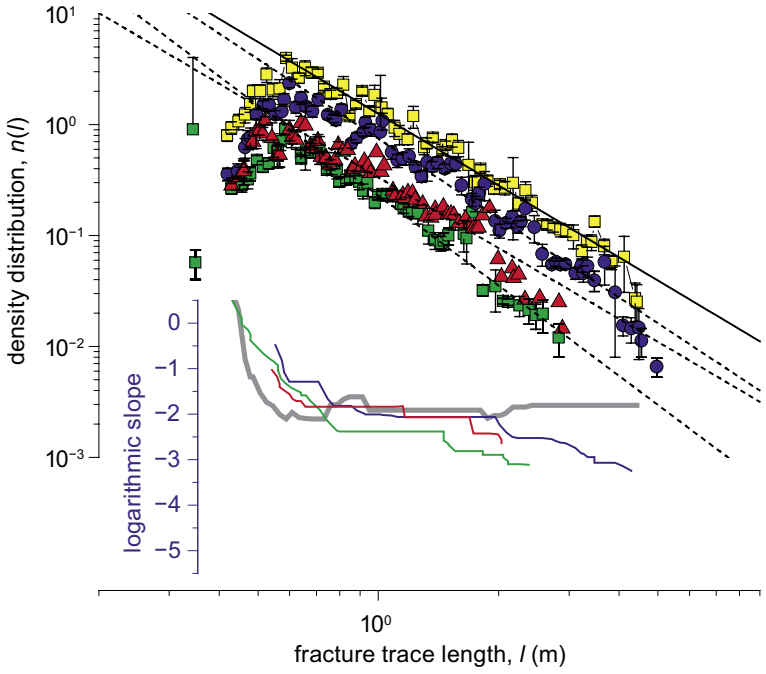

Figure 3-6. *Same as in the previous figure for outcrop ASM025. The power-law length exponent is –2.2 for the whole fracture set. The fits for the three subsets lead to power-law length exponents of –2.35, –2.1, and –2.7 respectively. The latter exponent is significantly smaller than the other ones, and tends to be as large as exponents calculated for outcrop ASM205 for instance (see the discussion about the differences encountered in the different outcrops). However this latter subset is also the one which contain the less number of fractures and we can cast doubt on the statistical relevance of this exponent.*

4 1st-order distribution on individual datasets

The performed analyses are exposed in details below. Complementary figures and summarizing tables are furnished in Appendix 1 for two-dimensional datasets, Appendix 6 for one-dimensional datasets, and for both, full stereonet representations in Appendix 2. The Appendix 1 also contains tables summarizing measured and interpreted parameters for the 2*d* length analysis.

4.1 Length distribution on large-scale lineament maps

Figure 4-1 shows the *lddf* calculated for the topographic lineaments. Qualitatively the *lddf* is well fitted by a power law whose best-fitting exponent is about –3. The logarithmic slope of the *lddf* displays quite large (but not statistically abnormal) fluctuations of the "local" exponent; the graph also gives the validity domain of the power-law fit which is between 400 and 3,500 m.

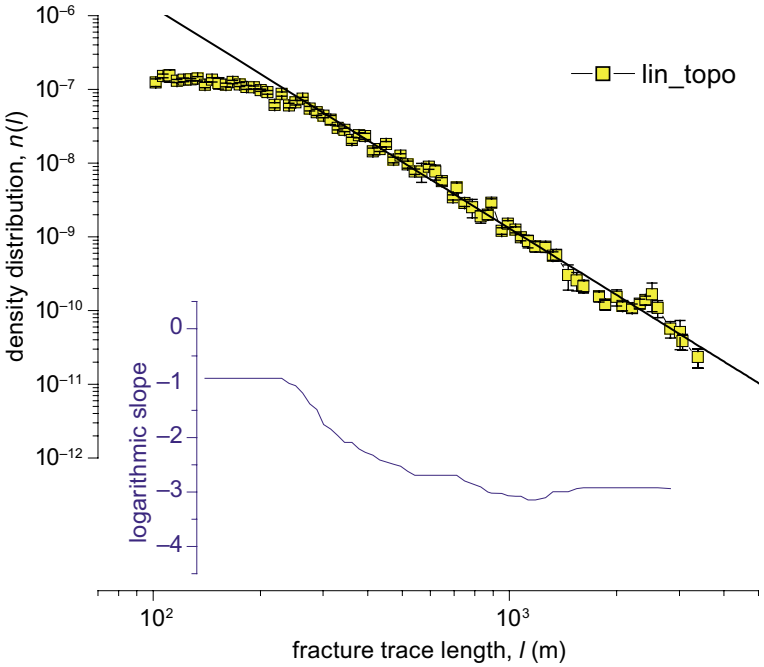

Figure 4-1. *The fracture distribution function calculated for the topographic lineaments (lin_topo). In blue, the logarithmic slope shares the same X-axis than the lddf.*

The Figure 4-3 shows another possible model for the length distribution: the exponential decrease. Such a model is generally related to a Poissonian process where randomly distributed points are joined to form an element. This was observed on the channel stream length distribution calculated for large river networks /Crave and Davy, 1997/. *Lin_2027* and *Lin_2028* are built from the same lineament database, by applying different linkage or segmentation rules when transforming the lineament network into fractures. The fact that *Lin_2027* and *Lin_2028* yield two different exponential functions may indicate that the Poissionian distribution directly derives from the linkage process. It would mean that these fitting functions can hardly be extrapolated to other maps.

If *Lin_2027* exhibits a pure exponential decrease, *Lin_2028* seems to follow a power-law trend for fracture lengths between 1,200 and 5,000 m (see Figure 4-2), with the same exponent of –3 than derived from the topographic map (*Lin_Topo*) and outcrops *ASM000205* and *ASM000206* (see next section). Compared to *Lin_Topo*, the power-law density function of *Lin_2028* is twice larger. Since *Lin_2028* has been reworked to take care of a more realistic transformation from lineament to fracture, we may expect this power-law trend to represent the distribution of some realistic fracture patterns. In terms of fracture density, it is rather difficult to compare *Lin_Topo* with *Lin_2027* without a thorough analysis of the objects that are eventually mapped.

A more thorough discussion on the connection between small-scale fracture outcrops and large-scale lineaments will be found in a next section.

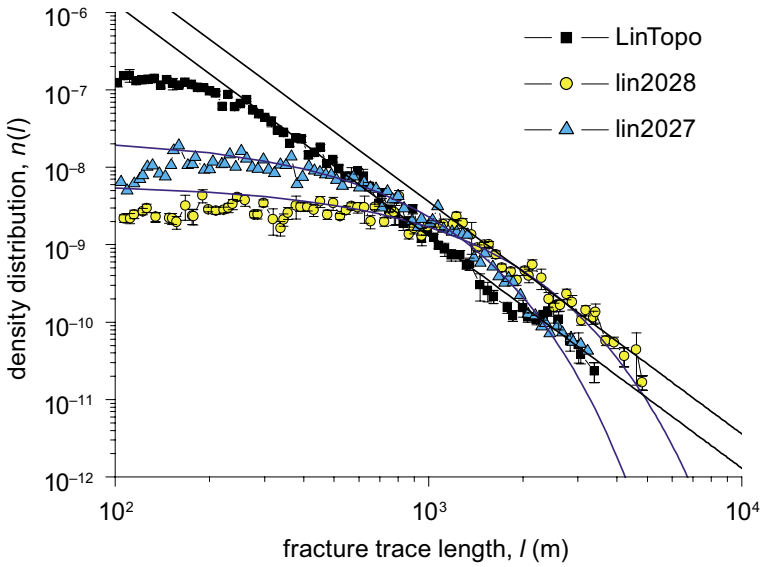

Figure 4-2. *The lddf's calculated for the three lineament maps. Lin_topo in black squares, lin_2028 in yellow squares, lin_2027 in cyan triangles, The black solid lines are power-law fits for the topographic lineament map, and for the Lin2028 map (lineament map corrected for segmentation effects). Blue lines correspond to lognormal fits.*

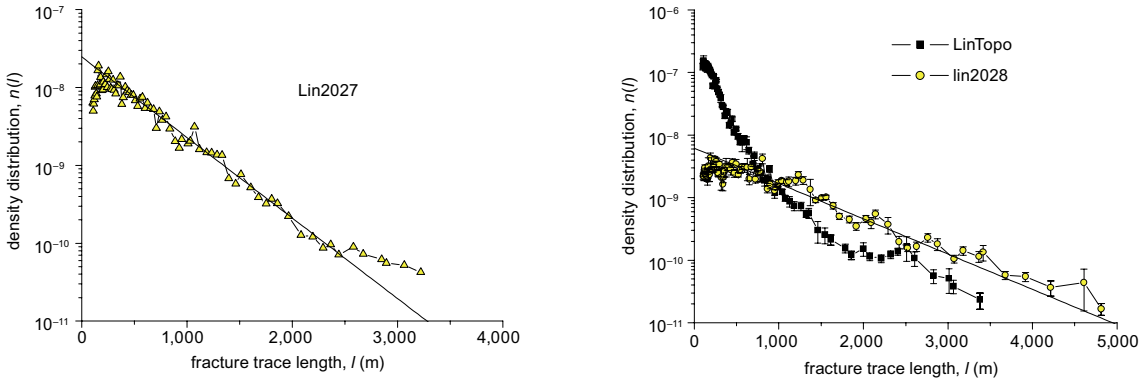

Figure 4-3. *Semi-log graphs for the lddf of the lineament maps. On the left, the lddf of the Lin2027 map shows a remarkable exponential decrease with a typical length scale of about 420 m. On the right, the Lin2028 map is also well fitted by an exponential function, but with a larger characteristic length of about 770 m. This is consistent with the fact that Lin2028 is derived from Lin2027 by correcting segmentation effects. Note that the lddf of the topographic lineament map (right graph) cannot be fitted by an exponential function.*

4.2 Length distribution on outcrops

The *lddf*'s calculated for the four outcrops (see Figure 3-1, 4-4 left, 4-5) shows remarkable power-law trends. For example, Figure 4-4 (graph on the right) shows that for outcrop *ASM000025*, the logarithmic slope in is about constant at –2.15 ± 0.1 from the resolution scale decided by the mapping operator (i.e. 50 cm) to ~ 5 m, which corresponds to ~ 1/4th of the typical size of the outcrop. A lognormal function also yields a good fitting (Figure 4-4 right) when the mode (i.e. most probable length) is much smaller than the resolution scale. Under these conditions, the difference between the lognormal fit and the power-law fit is less than 20% over the admissible range of fracture lengths.

The sampling quality is also a potential issue for validating the *lddf*. In particular we do observe that the fractures that belong to granitic or pegmatic veins have not the same spatial organization than the rest. In particular they are highly clustered and form long but segmented fractured zones (in yellow on Figure 4-5). However their contribution to the *lddf*'s is quite small: the *lddf* is decreased by less than 20% when removing the vein fracture set (Figure 4-5 bottom graph), and the decrease does not change the general shape of the distribution function. Note that this ratio of ~ 10–20% is consistent with the area occupied by veins. Note also that the number of fractures belonging to these veins is not large enough to calculate a sound *lddf*.

To conclude, despite some ambiguity in the fracture mapping we are quite confident about the relevance of the calculated distribution function.

The fitted *lddf*'s for the four outcrops are provided in the Appendix 1. In terms of density and scaling trends, there are clearly two groups of outcrops: in the one hand, *ASM000025* and *ASM000026*, and in the other hand *ASM000205* and *ASM000206*. This analysis confirm the observation made on outcrops, that lithology and/or grain size seems to control the fracture distribution, at least at the scales that are covered by the fracture mapping.

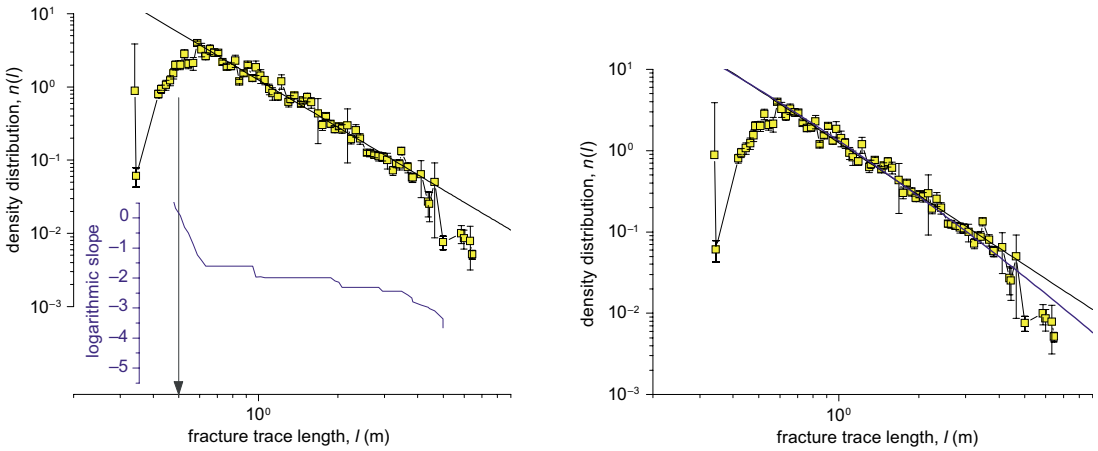

Figure 4-4. *Fracture length density distribution function calculated for the outcrop ASM000025. Left) The upper curve (square and black solid line) gives the data and a power-law fit. The lower curve in blue gives the logarithmic slope and refers to the blue axis. The validity of the power-law fit can be directly appreciated by the more or less constant logarithmic slope between the resolution scale and 1/4th of the system length. Right) Same as the left graph with two curve fitting: power law (black curve) and lognormal function (blue curve).*

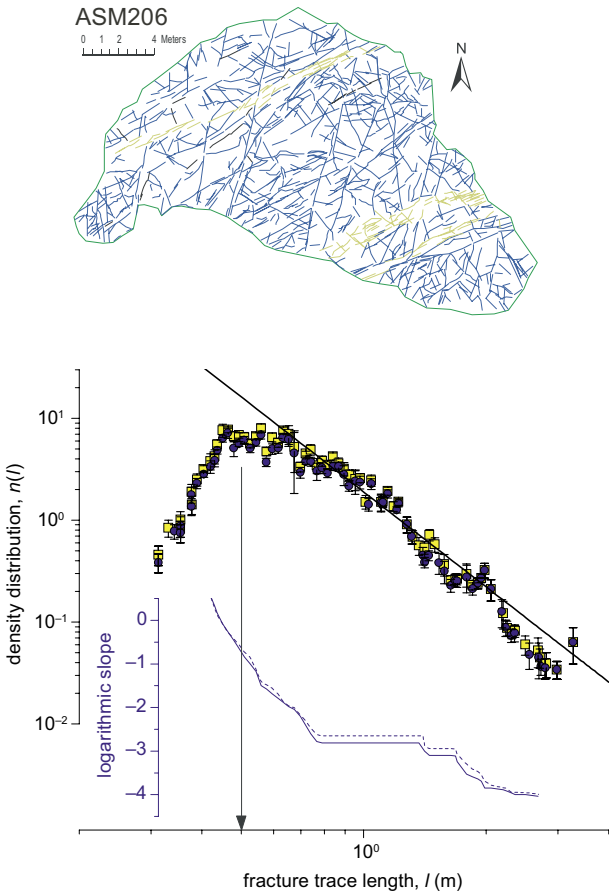

Figure 4-5. *Length density distribution function (bottom graph) calculated for the outcrop ASM000206 (top map). The yellow squares represent the lddf of the whole data set, while the blue ones have been calculated when removing the yellow fractures of the outcrop map that belong to granitic or pegmatic veins. The logaritmic slope of the complete (incomplete, resp) dataset is the solid (dotted, resp) line of the lowest graph.*

4.3 Length distribution on scan-lines drawn on outcrops

4.3.1 Measurements

Two scan-lines were drawn on each of the four outcrops in two different directions (positions are provided in Appendix 1). The four graphs represented in Figure 4-6 show the scan-line distribution for each outcrop. Clearly both directions are not identical but this rather renders the variability of the *lddf* due to the small number of fractures counted for each scanline (which is comprised between 27 and 48) than a significantly different trend. Actually a well-constrained *lddf* that can be fitted over a significantly large range of scales would require several hundred of elements, and better several thousands. This is clearly not the case for the scanline dataset, which causes a fairly large uncertainty on the derived *lddf* parameters.

Here we present power-law fits for each group of data (one per outcrop). It does not mean that the power law is the best fitting function – a lognormal function would have given similar fit quality –; the fit merely shows trend of the density scaling since it is not possible to discuss the underlying distribution model with the scale range and actual precision of the scanline *lddf*.

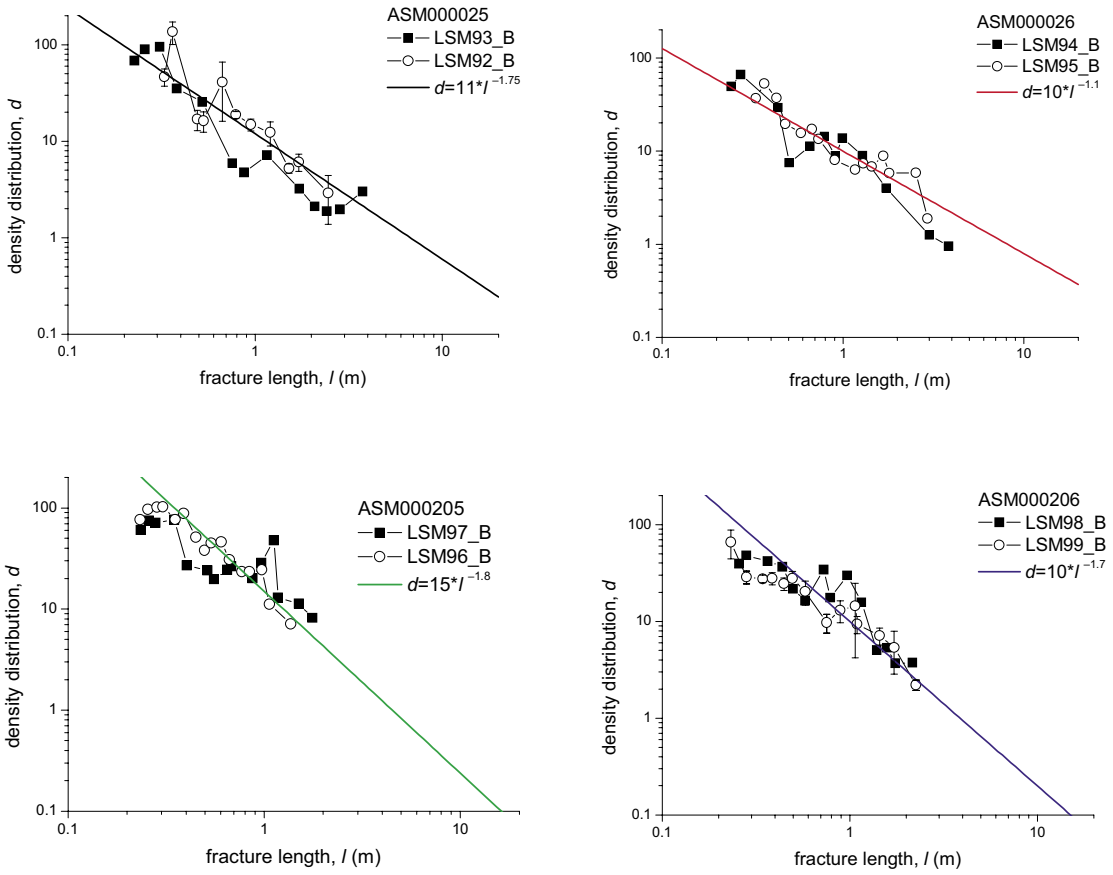

Figure 4-6. *Fracture distribution function d – number of fractures of length in [l, l + dl] per unit scan-line length – of the 8 scan-lines drawn on the four outcrops.*

4.3.2 Interpretation

The power-law fits (Figure 4-7) show apparently the same trends than observed for the 2D *lddf*'s, with two groups of outcrops: in the one hand *ASM000025* and *ASM000026*, in the other hand *ASM000205* and *ASM000206*. However the number of fractures mapped along the scanlines is quite small to provide a sound fitting. The large scattering of basic distributions (Figure 4-6) makes the scanline analysis not as useful as the 2D *lddf*.

Since two scanlines at different orientations has been mapped for each outcrop, we could have expected to draw information about scaling anisotropy. But this rather highlights the intrinsic scattering of the derived distribution function.

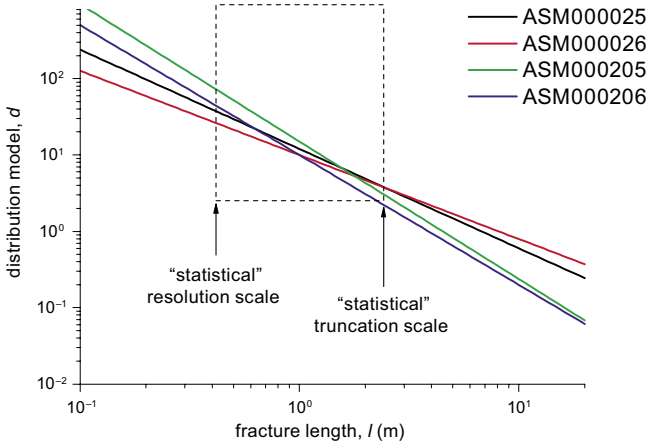

Figure 4-7. *Power-law fits performed for the four outcrops (the fit takes account of both scanlines drawn for each outcrop).*

4.4 Scaling of the fracture distribution function

4.4.1 Preliminary statement

Characterization of the distribution scaling is performed through measurement of fractal dimension by the pair correlation integral function method. This permits to estimate the apparent fractal dimension D_{1d} for one dimensional (boreholes) data and D_{2d} for two dimensional (outcrops and lineament maps) data.

As the fracture length distribution model rely on all fracture traces, the distribution scaling is obviously also measured from the same basic dataset. Therefore all fractures (fracture positions) are taken into account in the analysis, for the two dimensional analysis but also for the one dimensional analysis.

Open and sealed fracture datasets, as registered along boreholes, display obviously distinct hydraulic properties. The density scaling analysis is therefore also performed for these subgroups. In a preliminary tentative to characterize the variations of density scaling with depth, subgroups are also defined according to the depth of the fracture intercepts. Note that this is possible because the 1d datasets are quite robust (mainly several thousands of points by dataset).

To facilitate the understanding of $C(r)$ representations, the following "layout" is systematically used in curves representations: the function $C(r)$ – left y axis in the log-log diagram – is represented as a "symbol plus line" curve and coupled with the representation of its logarithmic slope (in gray) – right y axis in the same diagram (see also Figure 3-3). Inaddition light gray grid lines on the diagram are linked to the logarithmic slope axis. on the diagram.

4.4.2 1*d* fractal dimension, D_{1d}

Regarding fracture trace length distribution, all fracture traces are equivalently considered, without consideration of open or sealed status. Therefore the comparison between 2d data and 1d data can be done later if 1d data contains both open (plus the partly open that are assimilated to open) and sealed fractures, that is "all" the fracture intercepts. Note that the "all" fracture intercepts contain only the identified fractures intercepts (crushed zones and "sealed network" are not taken into account). Besides, since open and sealed fractures obviously display very different hydraulic properties, we apply the fractal analysis also on these sub-networks.

To sum up, the following cases were considered:

- all fracture intercepts,
- open and partly opened fractures,
- sealed fractures,
- all fracture intercepts over a finite range of depth (within the ranges [0; –100], [0; –500] and [–500; –1,000], when boreholes are long enough).

All primary results (diagrams of $C(r)$ and ratios $C(r)/C_{random}(r)$) are provided in Appendix 6 for all, all randomized, sealed and open fracture-intercept datasets. Analyses over a finite range of scales are not provided, but they did not show any specific tendency.

Mean fracture densities over the boreholes are comprised between 4 and 12 fractures per meter. Therefore, for a homogeneous dataset, the mean distances between two nearest neighbors are most comprised between 0.3 and 0.1 meters. Thus, below that scale very few pairs of points can be found and the scale corresponds to the practical resolution scale for the $C(r)$ analysis.

For KSH01A, we calculate a dimension almost equal to one when considering all fracture intercepts. This is characteristics of a uniform spatial repartition (Figure 4-8 left), at least over the range of scale considered. When comparing the sealed- and open- datasets it brings out that the open- dataset seems to be slightly correlated with a well defined exponent equal to 0.9, whereas the sealed- dataset seems to be homogeneous, as long as the all- dataset.

Observations of results obtained for the KAV01 dataset show a different tendency (Figure 4-9). When taking all fracture intercepts, the fractal dimension is now well defined and equal to 0.95. In addition, no clear distinction can be performed between the corresponding open- and sealed- dataset.

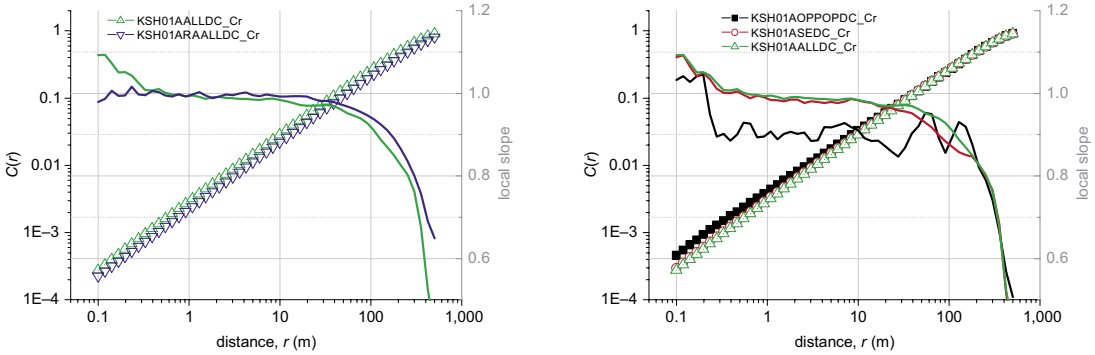

Figure 4-8. *Borehole KSH01A, left) C(r) for all- and all_randomized- datasets, right) C(r) for all-, open- and sealed- datasets.*

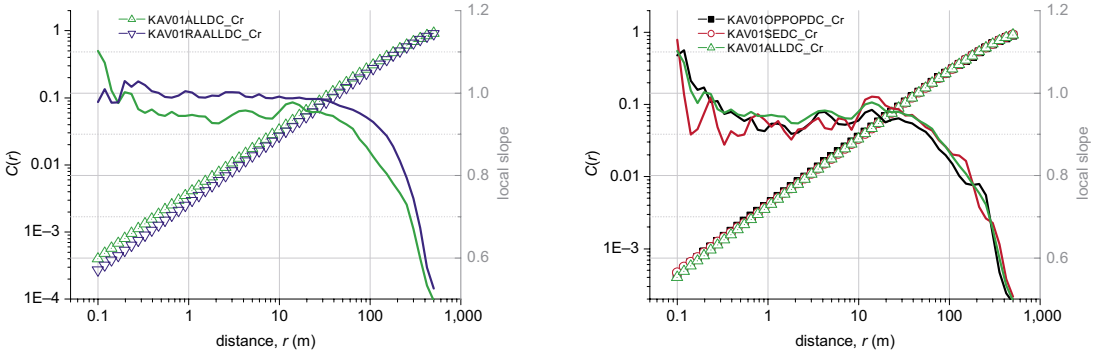

Figure 4-9. *Borehole KAV01, left) C(r) for all- and all_randomized- datasets, right) C(r) for all-, open- and sealed- datasets.*

Table 4-1. Summary of fractal dimensions measured along the 1*d* datasets.

Borehole	$D_{1d, all}$
HSH01	0.96
HSH02	0.97
HSH03	0.95
KAV01	0.95
KLX02	0.91
KSH01A	0.99
KSH01B	0.99
KSH02	0.98
KSH03A	0.97
KSH03B	0.97

To conclude for the borehole datasets, the fractal dimensions are really close to 1, more precisely between 0.9 and 1, when taking all fracture intercepts (see table above). This would mean that the fracture clustering, or spatial correlation, is quite weak and cannot be really identified in all cases and, moreover, the fractal dimensions measured remains between 0.9 and 1. Except for boreholes HSH02, KAV01 and KLX02, open- datasets seem to be slightly more spatially correlated than sealed- datasets. Whatever the dataset considered (all-, open-, sealed-), no fractal dimension below 0.9 is measured.

4.4.3 2d outcrops and lineament maps

Analyses of $C(r)$ on the outcrops and lineament maps are entailed with strong finite size effects: map outlines are irregular and the range of scales investigated is limited. Moreover, except for the lin_topo map, each dataset contains only about a thousand points.

The treatment of outcrop *ASM000025* is illustrated in Figure 4-10. We observe that finite size effects appear from a distance close to 5 meters. The resolution scale is found to be around 0.5 m, a value similar to the one of trace length. Therefore the available range of scales for measuring a fractal correlation on fracture positions is restricted at best to 0.5–5 m. Over that range the local logarithmic slope of $C(r)$ lies in the range 1.8 to 2.

The analysis is repeated for the 4 outcrops and 3 regional lineament maps (Figure 4-11).

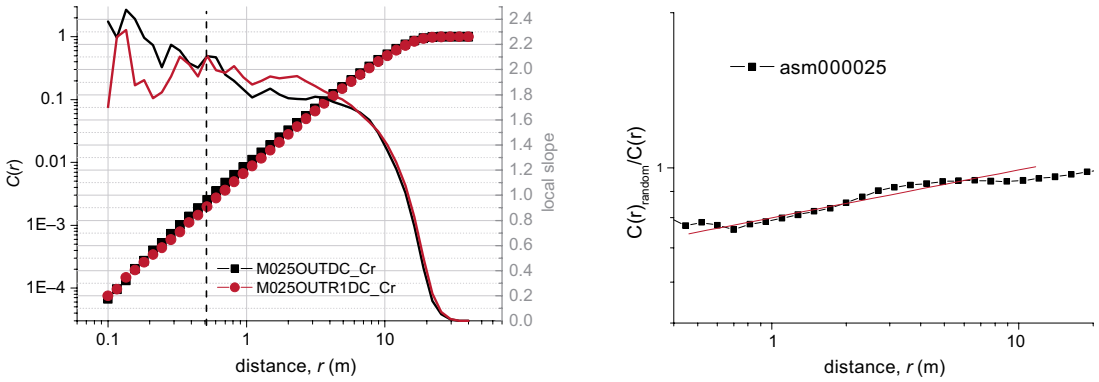

Figure 4-10. *Outcrop ASM000025, left) Integral of correlation C(r) for natural dataset (black) and randomized dataset (red), right) ratio of C(r)/ $C_{random}(r)$.*

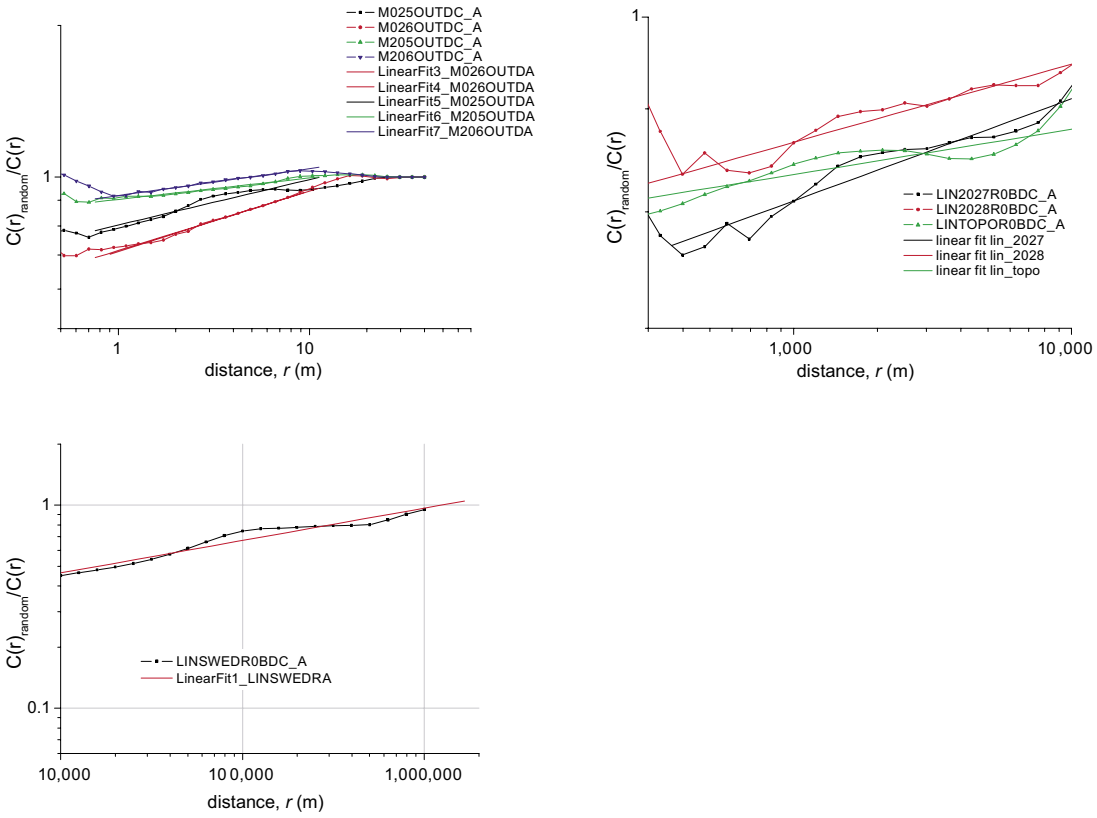

Figure 4-11. *Ratios C(r)/ C_{random}(r), top left) for the 4 outcrop asm-maps. Top right) for lineaments maps lin_topo, lin_2027 and lin_2028, bottom) for lin_sweden.*

For each dataset, the fractal dimension is measured from the power-law fit of the ratio $C(r)/C_{\text{random}}(r)$ over a range of distances close to one order of magnitude. The minimum distance is equal to the resolution scale of the system (for instance 0.5 m for the outcrops, and a few hundreds meters for the lineament maps). The maximum distance is the system size divided by a factor comprise between 2 and 4 (depending on the boundary shape). Several fits were performed, that give an uncertainty on the exponent of about ± 0.05. The exponents measured on the two-dimensional datasets are given in the table below.

Table 4-2. Summary of fractal dimensions measured along the 2*d* datasets.

Reference name	D_{2D}
ASM000025	1.91
ASM000026	1.88
ASM000205	1.96
ASM000206	1.95
lin_2028	1.96
lin_2027	1.95
lin_topo	1.98
lin_sweden	1.84

Except for the lin_sweden map, the fractal dimensions are close to 2 (at least between 1.9 and 2), which indicate weak spatial correlation.

Both the one-dimensional and two-dimensional analysis of the density scaling confirm that the fractal dimensions are close to trivial values (1 in 1*d*, and 2 in 2*d*), meaning that the fracture dataset is consistent with a poissonian distribution. Some variations are nonetheless observed, but they seem to indicate rather an intrinsic variability than a systematic trend.

4.5 Orientation distributions

Representations of orientation distributions – lower hemisphere projections on stereonets – are provided in Appendix 2. An interpretation in term of fracture sets, for outcrops *ASM000025* and *ASM000025* is provided in Appendix 3.

We comment hereafter the orientation distribution without performing the classical division in fracture sets (term $O_{pdf}(\theta,\varphi)$ of the first order distribution model).

4.5.1 2*d* maps orientations

Contoured Schmidt stereonets of the four outcrop are displayed in Figure 4-12 below (discrete steoreonets are available in Appendix 2). An interpretation of these orientation distributions in term of fracture sets is given in Appendix 3 for outcrops *ASM000025* and *ASM000205*. The figure shows several zones of higher fracture intensity. All are located around dip directions close to 80 to 90 degrees. This indicates that fractures sampled are mainly sub-vertical.

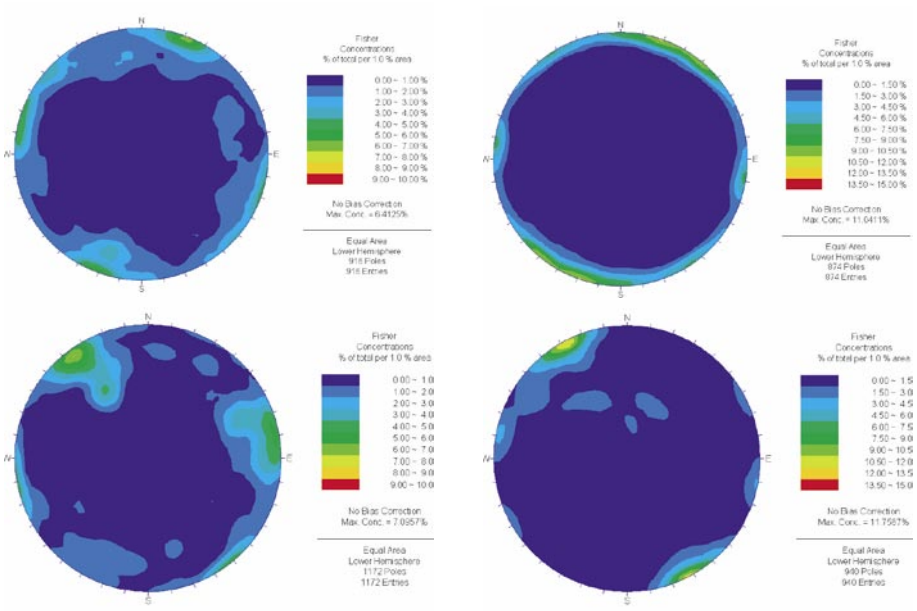

Figure 4-12. *Schmidt density representations of orientation distributions of fracture poles, top left: ASM000025, top right: ASM000026, bottom left: ASM000205 and bottom right: ASM000206.*

The corresponding strike distribution (not affected by orientation bias since outcrops are assumed to be horizontal) could be analyzed by quantifying to which extent the apparent peaks in the strike distribution differ from the uniform background strike intensity. In other words, the orientation distribution is divided in a background intensity of fractures with uniformly distributed orientations plus peaks of specific orientations. The orientation distribution of background fracturing can be simply modeled by a uniform distribution of orientations and the next peaks intensity can be estimated to assess whether or not, according to their size, they should be taken into account in the first order modeling.

For that purpose, peaks of intensity should be separated from the mean background intensity. By developing such analysis one could assess whether the peaks, cleared from the background, should be distinguished or not from the rest.

Regarding the orientation distribution, the background fracturing constitutes the part of the fractures that can be modeled through a uniform orientation distribution.

For instance, the background strike intensity for *ASM000025* and *ASM000026* is estimated to be close to half of the total strike intensity, whereas is reaches almost 2/3 of the total fracture intensity for outcrops *ASM000205* and *ASM000206* (see figure below). The peak located around strike 60 for *asm*206 representq therefore one third of the fractures in the dataset. Peaks isolated in *ASM000025* and *asm000026* represent around one third to 1/6 of the fractures.

Strike distributions of lineament maps are displayed on rosette diagrams in Figure 4-14.

Similar observations on the lineaments maps lin_2028 and lin_2027 show a background intensity eaching at least 80% of the total (Figure 4-14).

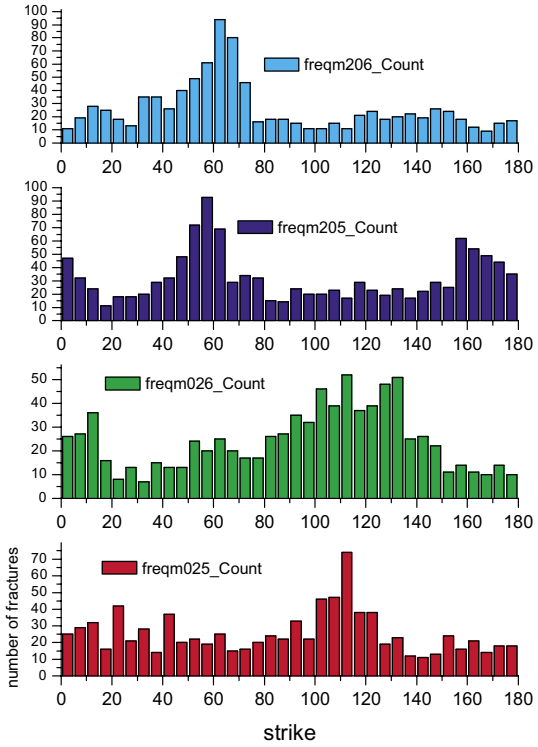

Figure 4-13. *Strike distributions for the four outcrops, from top to bottom: ASM000025, ASM000026, ASM000205 and ASM000206.*

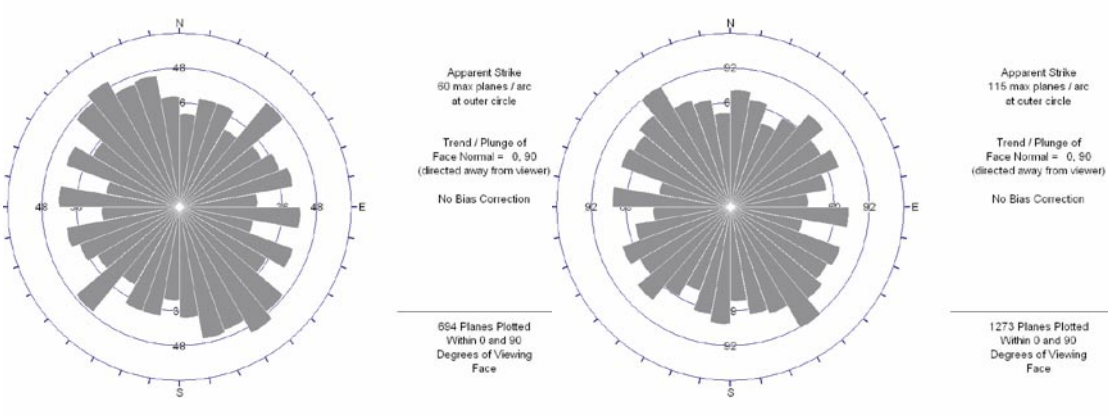

Figure 4-14. *Strike distribution from the lineaments data sets lin_2028 (left) and lin_2027(right).*

In summary, the fracture background intensity for the lineaments and outcrops data reaches between a half and around 80% of the different datasets. Besides, the presence of additional peaks highlights a similarity between *ASM000025* and *asm000026* on the one side, and *ASM000205* and *ASM000206* on the other.

4.5.2 Boreholes orientation distributions

Orientation distributions are represented for the 10 different boreholes having strike/dip fields (all boreholes except KLX01). Observations are based on discrete and contoured Schmidt diagrams of fracture poles (see Appendix 2), as illustrated on Figure 4-15 for borehole KAV01. Here orientations distributions are observed as statistical distributions, no attempt is made at that stage to correlate the observations with the borehole spatial location, depth or encountered lithology.

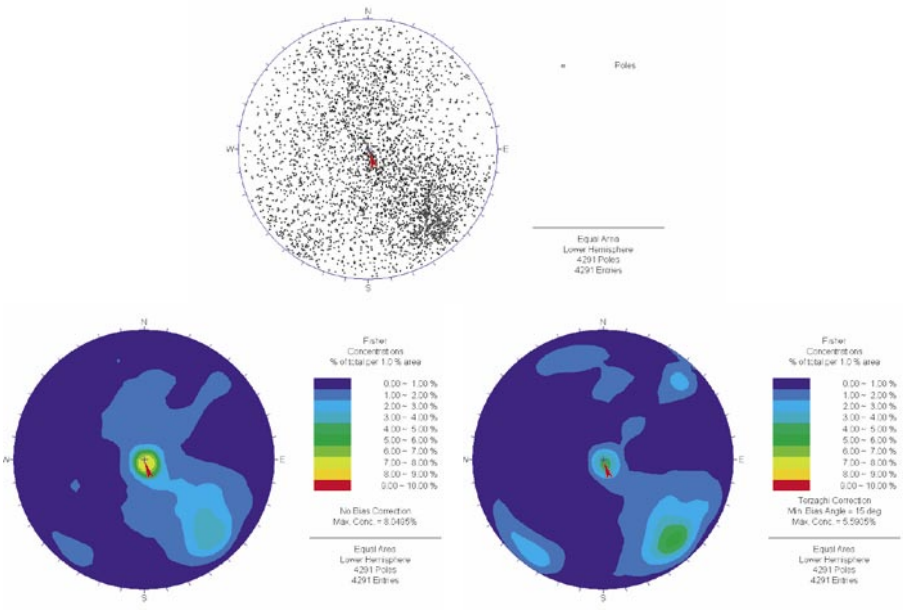

Figure 4-15. *Stereonet diagrams for 1d fracture dataset KAV01; (top) discrete plot; (bottom), not corrected (left) and corrected by Terzaghi correction (right).*

The general trend present for all the borehole datasets is a dominant proportion of sub-horizontal fractures, with a fracture dip close to 0 (as illustrated in Figure 4-15 for borehole KAV01). The tendency is stronger for the largest datasets (longest boreholes). Even after applying the Terzaghi correction, the peak corresponding to sub-horizontal fracture set remains dominant in most cases. Regarding the non-horizontal fractures, general and well identified tendencies are more difficult to highlight. Peaks are not systematically present and their mean position (along the dip axis) is variable. In some cases, we observe peaks of orientations in a direction compatible with strike-NE (for instance borehole HSH02, see Appendix 2). Apart from these observations, the orientations distributions appear to be very variable from one borehole to another. Further investigations would be necessary to understand the reason of such variability.

At this stage, and for generation purposes, corrected “bootstrapped” files corresponding to the different orientations distributions are provided (description in Appendix 5).

An additional comparison between 1d and 2d datasets is performed in Section 5 (the 3d scaling model).

5 The 3D scaling model

5.1 Some model issues

The objective is to find the 3D fracture network model which is statistically consistent with the parameters measured on all available datasets (boreholes, outcrops, and large-scale maps). Such a model is supposed to fit the entire range of scales that are measured, and to predict the scales where no information is available (Figure 1-1). Before developing the scaling model, we would like to point out some of its limits:

- We cannot claim that a single DFN model can describe fractures at all scales and in all places. Lithology (see previous paragraphs) or distance to tectonic events significantly modifies the parameters of the fracture distribution function. However making the exercise to define a mean DFN model is not useless since it may help to precise the nature and extent of this variability in DFN parameters.
- The scaling of the DFN model is limited at large and small scales due to obvious physical constraints. The upper limit is well constrained by the mapping of large-scale structures. In contrast, there are no, or a few, indicators of the small-scale limit of the DFN model with available data. Considering the importance of small fractures on flow dispersivity, this issue deserves address by further work.

From a general point of view, a DFN model describes the number of fractures that can be found in a space *S*, with a set of properties such as length, strike, dip, shape factors… There are several issues that are worth noting:

- Since we are concerned with the fracture distribution model, the density term is the number of fractures belonging to a given volume. This definition is meaningful only if a fracture is represented by one typical point that we have chosen to be its barycenter.
- The embedding space *S* has both a characteristic length scale (its typical size), and a dimension (2D for outcrops and maps, something between 1D and 3D for boreholes). The number of fractures encountered in S thus depends on the probability for a fracture of having an intersection with *S*, which is a complex function that depends on fracture density, length and orientation, and that we will develop below.
- The fracture density can be scale dependent, if for instance fractures are clustered in a fractal way. The fracture distribution function thus depends on *S*.
- The classical parameters measured on field outcrops such as P_{21} (the total fracture trace length over an area) also depends on the scale of resolution of the mapping – especially because small fractures are much more numerous than large ones. Thus these classical parameters cannot be considered as invariants of the *fdf* model. We therefore develop relationships by using the very parameters of the *fdf* model.
- The fracture parameters can depend on each other. For instance the fracture density or length distribution can depend on orientation, or small fractures can be more clustered than larger ones /Bour and Davy, 1999/. Some of these correlations can be simply expressed in the 1st-order DFN model; others cannot and require additional mathematics. Note that these 2nd-order correlations still require more information than the 1st-order model to be properly validated, especially when aiming at extracting scaling parameters. With the available dataset, it is not always possible to extract a statistically sound data subset on which a 2nd-order correlation would be calculated.

In the next paragraphs, we compare outcrop maps and large-scale lineament maps. The issue thus amounts to look for a 2D DFN model, which can provide a good fit of the different areal distribution functions whatever the map scale. In the latter paragraph, we aim at comparing 1D boreholes and fracture maps. This requires building the basic 3D DFN model, compatible with borehole fracture intersection frequency, and outcrop and lineament-map *fdf*s.

5.2 Scaling of fracture density from outcrops to large-scale lineament maps

If we take a typical value of the areal fracture distribution function for each outcrop or map, we can try to draw the best-fitting model that joins all these points. In theory and because of a possible fractal clustering, the areal fracture distribution function depends on both the chosen fracture length and the typical size of outcrop or map L such as:

$n(l, L) = n_{ddf}(l)* A * L^{D-2}$,

where A is the map area (with $g(\Sigma) = A*L^{D-2}$, see equation (1)). The fractal dimension has been calculated for the different maps (see previous section) with values close to 2 which mean that the fractal correction is very small.

Another way to evaluate the fractal term is to compare the fracture density of each maps when extrapolated to a fracture length of 1 m (Figure 5-1). When comparing maps of different areas, we can try to evaluate the fractal correction which should lead to a decrease of the areal density term. Figure 5-1 does not show any significant decrease compared to the observed variability. The best we can do if we really want to find a fractal decrease is to consider that outcrops *ASM000205* and *ASM000206* are linked to the topographic lineament map (dashed line in Figure 5-1). This would give a fractal dimension of about 0.08, which anyway remains small.

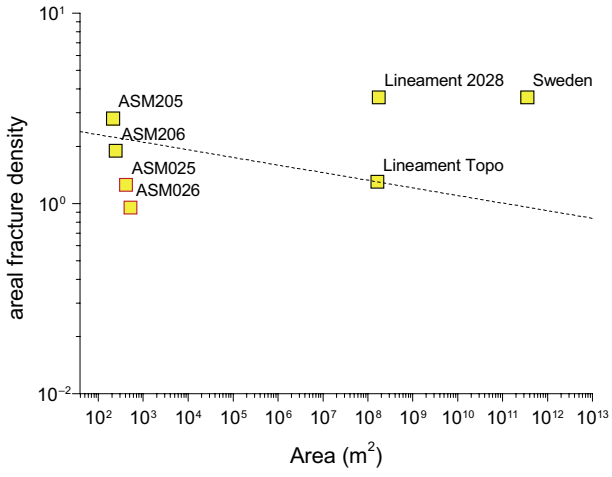

Figure 5-1. *Areal fracture density extrapolated for a fracture length of 1 m as a function of the area of outcrop or lineament map.*

5.3 Scaling of the fracture length distribution from maps and outcrops

The idea when comparing different maps is to find a 2d model that fits both outcrop and large-scale maps, and thus fills the scale gap between about 10 and 100 m. We first discuss the mathematical function that provides the best fit through scale (power-law, lognormal and exponential). We then compare the different maps.

5.3.1 Comparing the different distribution model: power law vs lognormal

In contrast to power laws, the lognormal function presents a maximum for a finite length (the mode value), and a large tail for large values. These mathematical properties make the lognormal value suitable to fit curves such as the fdfs shown in the preceding figures since it can fit the typical bell shape of fracture length distributions. But this would be physically irrelevant since the fdf decrease is associated to the resolution issue, i.e. the inability to map all small fractures. Moreover such a lognormal fit is mathematically unable to predict datasets sampled at a different scale or resolution (Figure 5-2, black curve).

If now the lognormal fit is achieved in the admissible range of fracture lengths (i.e. above the resolution scale and below the largest length recorded), we obtain an excellent agreement with measured fdf (blue curve in Figure 5-2) with a mode which now becomes much smaller than the resolution scale. However this ("large scale") best-fitting function for the large-scale lineament map (blue curve in Figure 5-2 or dashed red curve in Figure 5-3) is totally irrelevant for fitting the outcrop fdfs (as shown Figure 5-3).

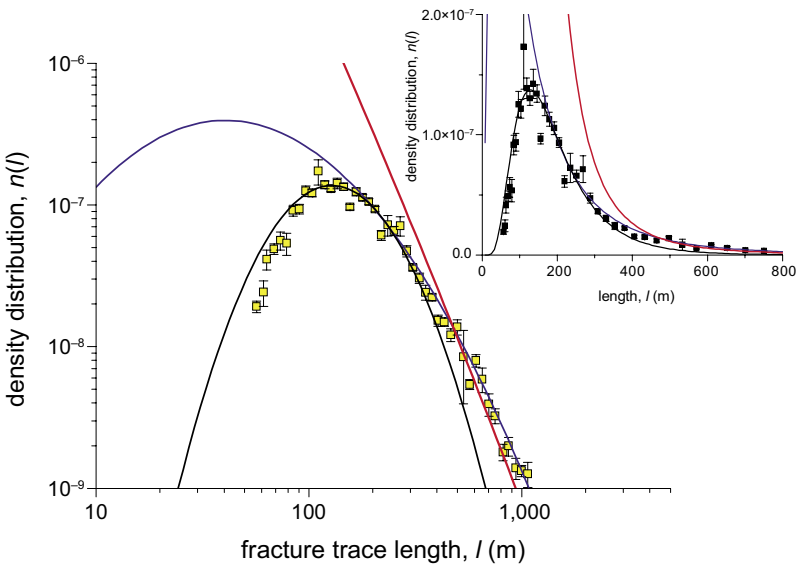

Figure 5-2. *Three different lognormal fits illustrated for the fdf of topographic lineaments. The black curve is derived from the entire dataset including points below the resolution scale. The blue curve fits length between the resolution scale and the largest recorded length. The red one is the best-fitting curve for both outcrop maps and large-scale lineament maps.*

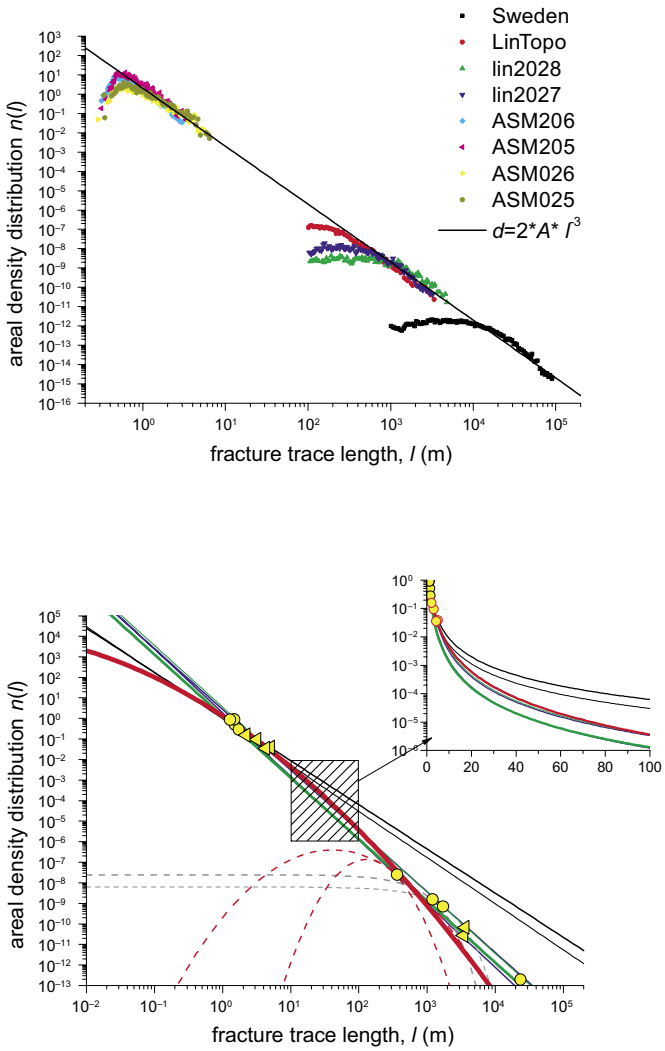

Figure 5-3. *The graphs represent individual best-fitting curves for outcrops, and large-scale lineament maps. On the top, the actual fdf are plotted with the best power-law fit. On the bottom, we plot all fits that have been found in previous sections. A power-law fit has been applied to ASM000025 and ASM000026 outcrops (black lines), ASM000205 and ASM000206 outcrops (blue lines), large-scale topographic lineaments and Lin_2028 (green lines). The best-fitting lognormal function is represented with* $\sigma^2 = 4$ *(bold red line). Both exponential functions that fit the large-scale maps Lin_2027 and Lin_2028 are plotted with a dashed grey line. The yellow circles represent one typical density value for each map and outcrops; the yellow triangles represent the largest length consistent with the power-law fit for each map and outcrops. The graph in the upper right corner is an enlargement of the dashed central part that shows the different fitting functions, and the resulting differences in terms of density predictions.*

At last we have calculated the lognormal function that fits all fdfs from outcrops to large-scale lineament maps (red line in Figure 5-2, and heavy red line in Figure 5-3). This large-scale fit is not very efficient to describe each fdf over the admissible range of fracture lengths (see red line in Figure 5-2).

We thus conclude that the lognormal fit is not a good candidate for defining a DFN model through scale, although it can provide excellent fit for individual fdf curve if needed.

5.3.2 Comparing fracture networks on outcrops and large-scale lineaments maps

Figure 5-3, where all individual fits are plotted together, emphasizes several points:

- The best-fitting functions of *ASM000205*, *ASM000206*, and large-scale topographic lineaments are consistent. The lithology encountered in both outcrops is diorite or monzodiorite, which represents the basic pole of the geological rocks of the Simpevarp peninsula, with fine to intermediate grain sizes.
- The exponential functions obtained for *Lin2027* and *Lin2028* are unable to predict observed outcrop densities. This is consistent with a close relationship between the exponential function and the manner the fractures are individualized from the lineament map.
- The lognormal functions, when fitted to topographic-lineament fdf, cannot predict outcrop densities. Same for the reverse (see also previous section). If all fdfs are put together, the lognormal fit (bold solid line in Figure 5-3) has a very large σ^2 value of 4; moreover it does not fit very well individual fdfs (see also previous section).
- Density functions derived from both outcrops *ASM000025* and *ASM000026* overpredict the lineament densities by about two orders of magnitude if extrapolated at same scales. The lithology of *ASM000025* and *ASM000026* is more or less towards the granitic pole, with quite large grain sizes.

Note that, in contrast with the exponential and lognormal fits that seem to be physically unrealistic and related to the manner fractures are mapped, we are confident in the power-law fit calculated for *ASM000025* and *ASM000026*. Beyond the statistical relevance, which is excellent, similar power-law exponents have been found for large-scale fault patterns /Davy, 1993; Bour and Davy, 1999; Bonnet et al. 2001/. The difference is also qualitatively visible on fracture patterns (Figure 5-4), on lithology and on grain size.

Figure 5-4. *Qualitative difference in fracture networks between the outcrop ASM000025 (left), and ASM000205 (right). The density of small fractures is much larger in the latter than in the former.*

The power-law fit found for the granite outcrops (*ASM000025* and *ASM00002*) cannot however be extrapolated to large-scale maps since it would predict a huge number of very large fractures that clearly do not exist. It would mean that there exists a limit to this fracture organization. The transition from the small-scale organization (observed on Figure 5-4 left) to large-scale lineament organization (that is self-similar to the one observed in Figure 5-4 right) could correspond either to a qualitative change in fracturing processes, or to a change in the nature of the mapped fracture zone since a large-scale fracture is not any more a single fractured plane but is a bundle of sub-parallel fractures. Note that we have no argument to favor one hypothesis against another.

Evaluating the transition between small-scale fracture organization and the large-scale one can become an important issue when trying to assess the consequences of the 3D DFN model. From the different fits drawn in Figure 5-3, we may assume that the transition is somewhere around 10 m, which is rather an order of magnitude than a well-assessed transition scale. This could be confirmed by a detailed study of fracture patterns at scales significantly larger than outcrops. Note that this uncertainty makes the prediction at scales between 10–1,000 m a bit uncertain.

5.4 Consistency between borehole fracture intensity and the distribution function calculated from outcrop networks

5.4.1 Preliminary issues

To assess the consistency between outcrop areal distribution functions and borehole fracture intersection frequency, we propose to derive both measures from the same basic 3D DFN model.

Following the conclusions of the previous section, we restrict our analysis to the power-law model although it can be easily extended to any distribution function. We use the following mathematical formalism[5]:

$$n_d(l,\theta,\varphi) = \alpha_d(\theta,\varphi)\, l^{-a_d} \qquad (6)$$

where d is the dimension of the embedding system (2D for outcrops, 3D for volume), and n_d the fracture distribution function per unit system size. /Piggott, 1997/ has calculated the relationships between the distribution parameters in 2D and 3D for randomly-oriented disks with a power-law length distribution:

$a_{3d} = a_{2d} + 1$,

$$\alpha_{3D} = \alpha_{2D}\sqrt{\pi}\,\frac{\Gamma\left(\frac{2+a_{2D}}{2}\right)}{\Gamma\left(\frac{1+a_{2D}}{2}\right)} \qquad (7)$$

We now calculate *the number of fractures that intersect a core*. We consider that the core is a cylinder of radius r and of height h. The condition for a fracture of length l and dip φ to intersect the core is to have its center within a cylinder of radius $\frac{l\cos\varphi}{2} - r$ (see Figure 5-5).

[5] With the correspondence to notations of equation 1: $\alpha_d(\theta,\varphi) = O_{pdf}(\theta,\varphi).\alpha$.

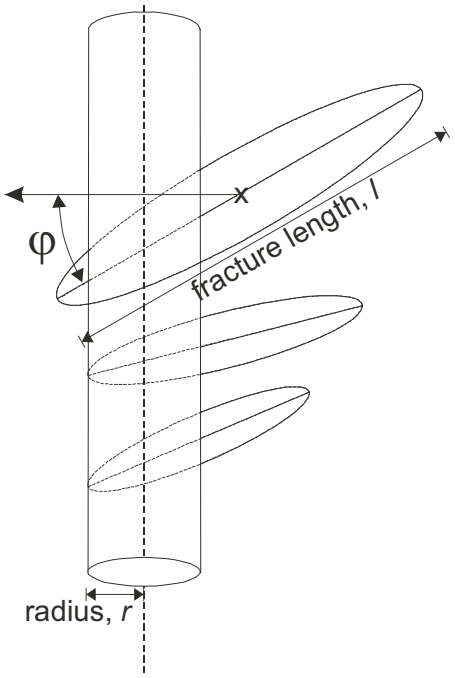

Figure 5-5. *Schema showing the geometry of a fracture intersecting the borehole. The fracture centre is at max at a distance of l cos φ/2 –r.*

For the general case of fractal density, the number of fractures that belongs to such a cylinder is:

$$\mathrm{d}N = h^{D_{3D}-2}\pi\left(\frac{l\cos\varphi}{2} - r\right)^2 n_{3D}(\theta,\varphi,l)\,\mathrm{d}l\,\frac{\mathrm{d}\theta}{\pi}\,\frac{2\mathrm{d}\varphi}{\pi}$$

All these fractures intersect the borehole if their length is larger than $\frac{2r}{\cos\varphi}$. The total number of fractures that crosscut the borehole is then:

$$N_I = h^{D_{3D}-2}\int_0^{\pi/2}\frac{2\mathrm{d}\varphi}{\pi}\int_0^{\pi}\alpha_{3D}(\theta,\varphi)\,\frac{\mathrm{d}\theta}{\pi}\int_{\frac{2r}{\cos\varphi}}^{\infty}\pi\left(\frac{l\cos\varphi}{2} - r\right)^2 l^{-a_{3D}}\,\mathrm{d}l \qquad (8)$$

The calculation can be done for any distribution of fracture length, dip and strike. For the simplest case of a non-fractal distribution of randomly oriented fractures, equation (8) can be analytically integrated, and gives

$$N_I = h\;\alpha_{3D}(2r)^{3-a_{3D}}\,\frac{1}{(a_{3D}-3)(a_{3D}-2)(a_{3D}-1)}\int_0^{\frac{\pi}{2}}\cos\varphi^{\,a_{3D}-1}\mathrm{d}\varphi \qquad (9)$$

which comes to $p_{10} = \frac{N_I}{h} = \frac{1}{18}\alpha_{3D}\,r^{-1}$ if $a_{3D} = 4$. Note that the number of intersections will vary inversely with borehole radius, which is a consequence of the selection criterion that a fracture must be large enough to break the entire core. We could have make a similar calculation for fractures that cut a given percentage of the core; it would come to increase p_{10} for the reasons mentioned just above.

Note also that the only scale of the fracture-intercept density is the borehole radius, which means that the scaling information is representative of the borehole diameter, and not of the borehole length, as it is mentioned in Figure 1-1.

5.4.2 Mean features of the borehole fracture intensity

The fracture intensities recorded in boreholes are extensively described in the Appendix 4. Here we would like to summarize some key features of the relationship between fracture intensity and lithology. These features are illustrated by the Figure 5-6, which gives the number of fracture intercepts per meter (thin lines and left axis) or the cumulative number (bold line and right axis) compared to lithology.

First of all, the fracture intensity appears to be highly variable from place to place, which is not inconsistent with what we know about the intrinsic heterogeneity of the fracturing process. But the cumulative curve shows that this variability is limited, and that it makes sense to derive average parameters. The example shown in Figure 5-6 is typical of what we can see in most of the boreholes. Indeed we do observe both a change of the fracture intensity, and of lithology. Above 300 m, the fracture intensity is larger than 15 fractures/ meter and the lithology is mostly given as quartz monzonite or monzodiorite. Below 300 m, fracture intensity is much smaller with values between 2 and 5 fractures/meter; the lithology is given as granite. The interdependency between fracture intensity and lithology can also be highlighted by small-scale features such as the diorite sill, located at depth about 870 m that yields a local increase of the fracture intensity up to 15 fractures/meter.

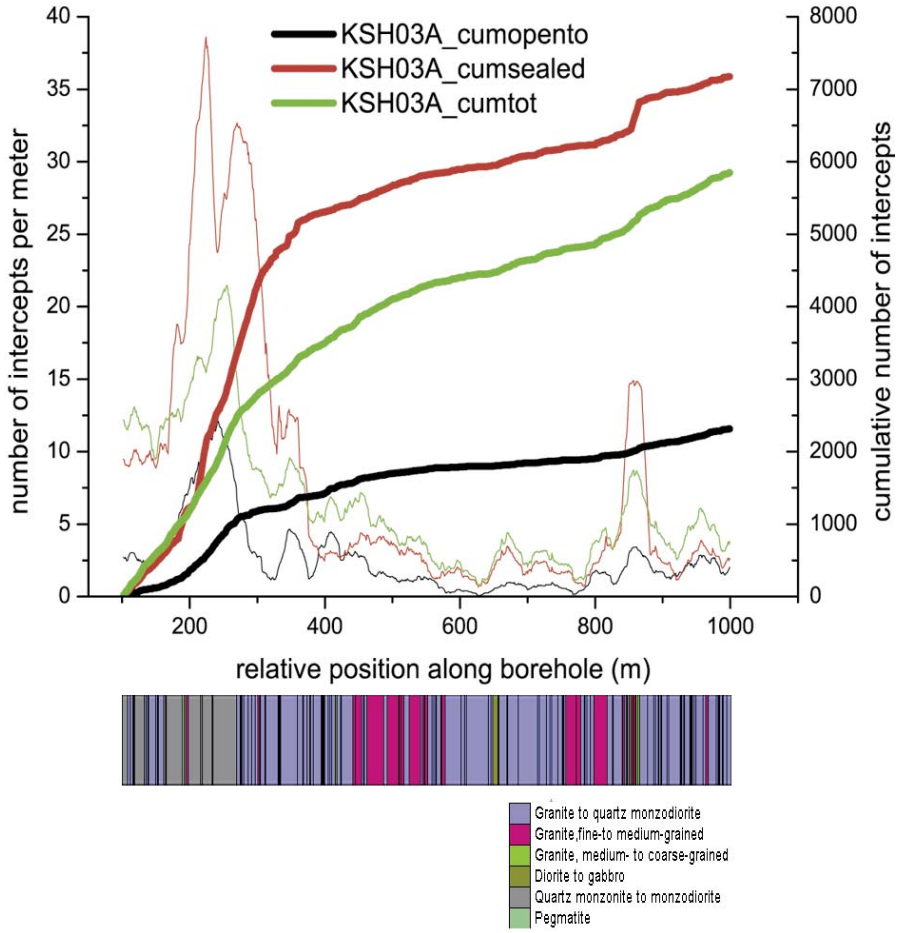

Figure 5-6. *Example of the relationship between fracture intensity and lithology. The graph gives the number of fracture intercepts per meter (thin lines, left axis) or the cumulative number (bold lines, right axis) as a function of depth for all fractures (black lines), or the sealed fractures only (red lines), or the open fractures only (black lines).*

5.4.3 About the orientation distributions

The fault plane orientation distribution of 2*d* outcrops displays mainly close-to-vertical fractures with two main peaks in strike (see Section 4.3). In contrast, boreholes sample mostly close-to-horizontal fracture planes (see Section 5.5.2). This result is qualitatively consistent with the rules of intersection and should be corrected by the classical Terzaghi coefficient. However even when applying the Terzaghi correction, a large discrepancy between outcrop-derived and borehole-derived orientation distributions still remains as can be shown in the next figure.

More generally, this observation points to the issue of the consistency between outcrop and borehole fracture sets. Even if both examples shown in Figure 5-7 are the most "critical" ones, and even if one considers the difficulty of sampling sub-horizontal fractures on outcrops and sub-vertical ones from boreholes, it is difficult to explain the inconsistency generally observed between outcrop-derived and borehole-derived orientation distributions (Appendices 1 and 2). If both datasets are really inconsistent as the orientation distribution seems to show, this would raise a few important problems for building a sound DFN model:

- A cause of such inconsistency could be that outcrops are not representative of the fracturing at depth. Since the DFN is mostly calculated from outcrop information, this would cast doubt about the relevance of such a DFN to describe the 3D fracture set.
- Another cause could be that the fracture distribution at the outcrop scale cannot be extrapolated to borehole scales. This could happen if there exists a major change of the very nature of fracturing between borehole scales (< 8 cm) and outcrop scales (50 cm – 3 m). This explanation does not seem to be consistent with direct observation in the field. It can be easily checked by a detailed mapping of some parts of outcrops. If it still comes to be true, this would cast doubt on the validity of the DFN to link scales, which in fact is the very reason why we attempt to calculate it.

Hopefully, we think that the observed discrepancy comes from an inadequate Terzaghi correction for borehole. In fact the Terzaghi correction assumes that boreholes are thin lines, which they are not actually. Equation (9) gives the exact expression of having fractures that fully intersect a cylinder. It can be shown that the angle correction depends on the fracture length distribution. This conveys that the number of intersecting fractures is dominated by the smallest ones (with the kind of length distribution that we get from outcrops), and that the length of the smallest fracture that can crosscut the borehole depends on the fracture dip.

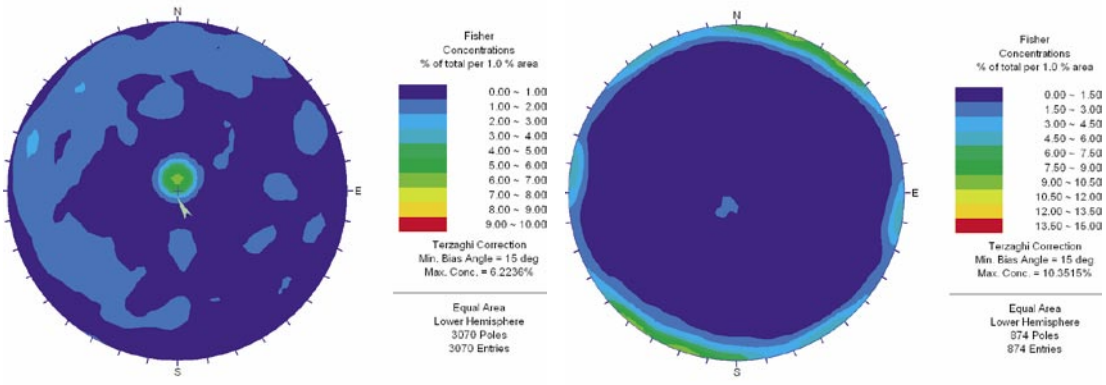

Figure 5-7. *Contoured stereonets corrected from orientation bias for borehole KLX02 (left), and outcrop ASM000026 (right). Both examples represent the most "critical" ones, with strong domination of sub-horizontal fractures on the vertical borehole and sub-vertical fractures on the outcrop (all datasets are represented in Appendix 2).*

For a power-law length distribution, equation (9) shows that the Terzaghi correction is actually $\cos\varphi^{a_{3D}-1}$. If a_{3D} is about 4, as it is found for outcrop ASM000205, the correction is $(\cos\varphi)^3$ rather than the classical $\cos\varphi$, which favors a lot horizontal fracture plane compared to inclined ones. This may explain why boreholes sample mostly horizontal fractures, while this is not observed in the Äspö gallery for instance.

5.4.4 Predictions from analytical solutions

The following table summarizes the prediction that we can make from the analytical derivation described in the previous section. The fracture intercept frequency is the number of fractures that break the borehole. To calculate this frequency from the outcrop parameter, we make the assumption that fractures are disks with a non-fractal density distribution and random orientations (this latter assumption can be easily changed; however the results are not significantly changed if we apply realistic distribution). The 3D density term has then been estimated from Piggott's formula. The number of fractures that entirely break the core are given by equation (9).

Table 5-1. Density parameters either estimated from the analytical solution equation (9) or measured from boreholes. The first line gives the nature of the parameters.

Lithology	α_{2D}	a_{2D}	α_{3D} (estimated)	Fracture intercept frequency (calculated)	Fracture intercept frequency (measured)
Lin2028	3.6	3	8.46	11.75	
Topographic lineament	1.3	3	3.1	4.3	
Outcrop ASM000205	2.8	3	6.6	10	
Outcrop ASM000206	1.9	3.1	4.53	7.3	
Outcrop ASM000025	1.25	2.15	2.6	7.3	
Outcrop ASM000026	0.95	2.25	2	3.6	
Diorite-like borehole					10–12
Granite-like borehole					3–6

With the crude assumptions described in the previous paragraph, we obtain very interesting information about the consistency between outcrop fracture distribution and borehole fracture intercept:

- Parameters derived from the outcrop *ASM000206* (close to the CLAB), which represents the diorite pole of encountered lithology, predict a very large fracture intercept frequency for boreholes.
- The other end member is the outcrop *ASM000026*, which differs significantly from the other for the fdf of scan-lines (Figure 4-7). Its fdf parameters predict low fracture intercept frequency.
- The two others outcrops predict intermediate fracture intensity values.
- The fractures of the topographic lineament map would predict low borehole fracture intensity, whereas the lineament map *lin208* is consistent with large borehole fracture intensity.

Note that the borehole fracture frequency is very sensitive to the detection threshold that has been used for counting fractures. For a power-law exponent a_{2D} of 3, the fracture intercept frequency increases by a factor 3 if we count fractures that cut only half of the core radius, while this factor is only 1.3 if $a_{2D} = 2.2$.

5.4.5 Predictions from numerical simulations

Analytical predictions presented in previous sections are based on uniform orientation distributions. In that case, density relations between 2*d* and 3*d* (resp 1*d* and 3*d*) parameters are given in equation (7) (resp equation (8)). Numerical predictions are performed here to check their consistency and mostly to couple results with specific bootstrapped orientations distributions.

Relations between the models parameters and properties in 1*d*, 2*d* and 3*d* are briefly recalled below, followed by the presentation of results from the numerical simulations.

Model parameters

The 3*d fdf* model is noted:

$$n_{3d}(l,L) = \alpha_{3d} l^{-a_{3d}} L^{D_{3d}}$$

The corresponding apparent 2*d* and 1*d* fracture models (fracture length traces distribution on an outcrop, fracture intersecting a borehole) are also power laws whose length exponents are related through:

$$a_{1d} = a_{2d} - 1 = a_{3d} - 2$$

Relations between α_{1d} and α_{2d} with α_{3d}, in the case of uniform orientation distributions were provided in previous section.

The number of fracture centres by unit of volume, P_{30}, and the cumulative surface of fracture by unit of volume, P_{32}, are simply expressed through the following relations:

$$P_{30} = \frac{\int_{l_{\min}}^{L} \alpha_{3d} \cdot l^{-a_{3d}} \cdot L^3 \cdot dl}{L^3} = \alpha_{3d} \frac{\left[l_{\min}^{-a_{3d}+1} - L^{-a_{3d}+1} \right]}{(a_{3d} - 1)}$$

and

$$P_{32} = C_{shape} \frac{\int_{l_{\min}}^{L} \alpha_{3d} \cdot l^{-a_{3d}+2} \cdot L^3 \cdot dl}{L^3} = C_{shape} \alpha_{3d} \frac{\left[l_{\min}^{-a_{3d}+3} - L^{-a_{3d}+3} \right]}{(a_{3d} - 3)},$$

where the C_{shape} is related to the fracture shape: $C_{shape} = \pi/4$ if the fracture is in 3d a disk of diameter l or $\pi/8$ if the fracture is an ellipse of eccentricity 0.5 and large axis l.

The cumulative fracture trace length by unit of area, P_{21}, is expressed through:

$$P_{21} = \frac{\int_{l_{\min}}^{L} \alpha_{2d} \cdot l^{-a_{2d}+1} \cdot L^3 \cdot dl}{L^3} = \alpha_{2d} \frac{\left[l_{\min}^{-a_{2d}+2} - L^{-a_{2d}+2} \right]}{(a_{2d} - 2)}$$

The 1*d* model arising from the intersection of a 3*d* power law model for the fracture *fdf* is also a power-law model of parameters α_{1d}, a_{1d} and D_{1d}. The number of fracture intercept by unit of length, P_{10}, is equal to:

$$P_{10} = \frac{\int_{l_{\min}}^{L} \alpha_{1d} \cdot l^{-a_{1d}} \cdot L^1 \cdot dl}{L^1} = \alpha_{1d} \frac{\left[l_{\min}^{-a_{1d}+1} - L^{-a_{1d}+1} \right]}{(a_{1d} - 1)}$$

By forming the ratios P_{30}/P_{21} it is possible to relate resp α_{2d} to α_{3d}. For l_{min} equal to 1, it comes that:

$$\frac{\alpha_{3d}}{\alpha_{2d}} = \frac{P_{30}(l_{\min}=1)}{P_{21}(l_{\min}=1)} \cdot \frac{(a_{3d}-1)}{(a_{2d}-2)} \tag{10}$$

Note that for the 2*d*-3*d* simulations, the equation (10) is valid if P_{30} is computed for all the fractures (by definition there $l_{min} = 1$) and P_{21} is computed only for fractures whose trace length on the outcrop is larger or equal to $l_{min} = 1$.

From the numerical simulations we obtain the ratio α_{3d}/α_{2d}. Since α_{2d} is known, we obtain simply an estimate of the α_{3d} corresponding to the 2d datasets.

1d to 3d

The α_{3d} density term is related to the P_{30} factor by:

$$\alpha_{3d} = P_{30}(l_{\min}) \cdot \frac{(a_{3d}-1)}{l_{\min}^{-a_{3d}+1}} = \frac{P_{30}(1)}{(l_{\min})^3} \cdot \frac{(a_{3d}-1)}{l_{\min}^{-a_{3d}+1}} \tag{11}$$

$$\Delta\alpha_{3d} = \frac{\alpha_{3d}}{P_{30}} \cdot \Delta P_{30}$$

$$P_{10}(1) = P_{10}(l_{\min}) \cdot l_{\min}$$

l_{min} is taken as the borehole diameter since only we consider only fractures that are large enough to break the entire core.

Simulations

The simulations take P_{10} or P_{21}, and a_{3d} ($a_{3d} = a_{2d} + 1$) as input parameters[6] and provide the P_{30} (or P_{32}) as output parameters (mean + standard deviation). In practice, a 3*d* synthetic model of discrete fractures is generated, until the frequency P_{10} or P_{21} is reached, resp on a borehole or an outcrop. In all cases, systems are considered as homogenous ($D = d$). Orientations distributions are simply bootstrapped from each dataset or taken as uniform.

The fracture network is generated in a cubic system of linear size L. The lower length cut-off of the fracture distribution is fixed to $l_{min} = 1$.

Output calculated values are averaged over a ten to a hundred of runs.

Datasets *ASM000205*, *ASM000025* and *KAV01* are used as bases for the simulations.

Numerical predictions

The variability of numerical estimations of α_{3d} is between 1 and 2%. ($\Delta\alpha/\alpha = \Delta P_{30}/P_{30} \leq 0.02$). For $a_{3d} = 3.15$, numerical predictions overestimate the α_{3d} from almost a factor of two. In fact, finite size effects lead to an overestimation of α_{3d}: no fractures are generated outside the system of size L; such fractures should intersect the outcrop and contribute to the parameter P_{21}. Therefore, to compensate the missing fractures, the "local" (in the system L) density is necessary larger to reach the P_{21} value.

[6] Relations between P_{32}, P_{21}, P_{10}, P_{30}, α_d and $l_{\min}$ are provided in Appendix 0. The combination of α_d and $l_{\min}$ is sufficient for calculating the P parameters.

Variations due to the orientation distribution lie between 2% for *ASM000205* outcrop and reach 6% for *ASM000025*.

Table 5-2. Results for the *2d-3d* case.

	Input			Analytical prediction /Piggott, 1997/	Simulations (calculated from equation (10))
Dataset original reference	**α_{2d}**	**a_{3d}**	**Orientations**	**α_{3d}**	**α_{3d}**[7]
ASM000025	1.25	3.15	bootstrapped	–	3.78
–	1.25	3.15	uniform	2.6	3.57
ASM000205	2.8	4.0	bootstrapped	–	5.48
	2.8	4.0	uniform	6.6	5.36

Table 5-3. Results for the *1d-3d* simulations.

	Input				simulations	
Dataset original reference	**$P_{10,measured}$**	**a_{3d}**	**l_{min}**	**Orientations**	**α_{3d}**	**$\Delta\alpha_{3d}$**
KAV01	5.79	4.0	0.08	uniform	1.11	0.16
KAV01	5.79	4.0	0.08	bootstrapped	1.05	0.16
KAV01	5.79	3.15	0.08	uniform	2.76	0.42
KAV01	5.79	3.15	0.08	bootstrapped	2.49	0.37

Numerical simulations predict that the density term α_{3d} varies between 1.05 to 2.76, depending on the input a_{3d} and on the orientation distribution. The main variation is due to the variation of a_{3d} between 3.15 and 4. The analytical expression equation (8) gives $\alpha_{3d} = 4.16$ for $P_{10} = 5.79$ and $a_{3d} = 4$. There is therefore a factor close to 3.75 between the theoretical and analytical predictions on α_{3d}. However, the theoretical analysis and numerical model use distinct hypothesis regarding the borehole assumptions. The numerical borehole is approximated by a one-dimensional straight line in the simulations; any fracture that intersects the borehole is recorded as long as it is larger than the borehole diameter. In the analytical solution, the real borehole volume is considered, and only fractures that fully break it are counted as intersecting fractures. As a consequence of the numerical approximation, the numerical α_{3d} density term is an underestimation of the "real" α_{3d} density term. Note that is effect is increased by the presence of a large proportion of small fractures (able to only partly cross-cut the borehole) in comparison to the borehole diameter. This occurs for large value of the exponent a_{3d} and small values of the l_{min} (minimum length of the fracture distribution function).

Secondly, numerical results show an apparent increase in α_{3d} when decreasing the value of a_{3d} from 4 to 3.15. However, as it was already noticed for the 2d-3d case, finite size effects become dominant when a_{3d} decreases to 3.15. In that case, a large proportion of large fractures (having their centres outside the volume of the system generation) are missing, leading to an artificial increase in the α_{3d} density term.

[7] Variability is not indicated in the table of results but in the text since it remains small, comprised between 1 and 2%.

However, both “borehole” and finite size effects remains equivalent when dealing with a uniform or bootstrapped orientation distribution. Therefore the numerical simulations remain a way to quantify the role, on the fracture model density term, of specific orientation distribution. Analysis from borehole KAV01 show that orientation effects lead to a variation of 6 to 10% in the density term estimation. This is of second order regarding the local variations in density from one borehole to another.

Conclusions

Two main effects prevent from using directly the numerical simulations to compare power-law fracture models and relate α_{3d}, α_{2d} and α_{1d} density terms: finite size effects and usual simplifications related to the borehole representation. The first one can be minimized by increasing the size of the volume where fractures are generated in comparison to the volume of interest (outcrop or borehole in the present case). The latter requires building the real borehole, with its volume, in the simulation, i.e. not to neglect the borehole thickness.

As finite size effects are related to the fracture lengths, variations in densities due to the orientation distributions can be simply quantified by the deviation in density recorded when considering different orientation distributions. By doing this, we show that bootstrapped orientation distributions arising from outcrops ASM- and borehole KAV01 entail small variations in densities: between 1 to 10%. These variations remain of second order in front of the local variations from one dataset to the other.

6 General conclusions

In this report, we have calculated the 1st-order fracture distribution for different datasets available through the Simpevarp site. We also attempt to define the maximum-likelihood model that is consistent with statistics at different scales.

The first order model characterized here is a fracture distribution function, noted, *fdf*, which provides the number of fractures of a certain length and orientation, belonging to a given volume of observation. Orientations are calculated as a probability density function noted $O_{pdf}(\theta,\varphi)$. The first order model comprises a priori all the fractures of the system, independently of their possible belonging to distinct fracture sets. The sampling-size term is related to a potential non-trivial scaling of fracture density, and thus to the dimension of the fracture network. Finally, the fracture distribution function, *fdf*, encompasses the fracture size distribution. As in the present work the power-law model has been found to the best scaling model, the additional parameters of the *fdf* is the power-law exponent a of the fracture length distribution.

Along the report, a special attention is paid to describe the methods used in data analyses, in particular regarding the length distribution and the density scaling characterization method. 1*d* and 2*d* datasets were investigated independently, to provide material for building the scaling DFN model. Local statistics is mostly based on both an analysis of the orientation distribution, and on the calculation of the fracture length density distribution function per unit area. The validity of the 3D DFN model, which is related to the consistency of the different local statistics across scale, is checked with analytical predictions and numerical simulations that guarantee the relations between different dataset parameters. Results are now summed up.

The basis of the study relies on the 2*d* datasets analysis and determination of a model for the *fracture length density distribution function* (*lddf*) defined per unit area. We found there that the best fitting model for the *lddf* is the power-law model. Different models have been tested to fit to the lineament data: power law, exponential and lognormal. The comparison between different models shows that, for a fixed range of scales, the power-law and the lognormal model can both lead to satisfactory fits. Note that the power-law fits calculated for outcrops are some of the best we have ever seen.

Five maps show well defined power-law fits: *lin_topo*, *lin_2028*, *ASM000205* and *ASM000206* with an exponent close to 3, and the remaining outcrops with an exponent close to 2.2. At the outcrop scale, the distinction between *ASM000205* and *ASM000206* on one side and *ASM00025* and *ASM00026* on the other, is also confirmed by difference in orientation distributions, and can be rationalized by a difference in lithology.

The fracture density scaling analysis is a complement to the length analysis: in order to normalise the local *fdf* from their respective sample size, the fractal dimension *D* associated to the density scaling, must be defined. For that purpose, the correlation integral method is applied over each dataset. All datasets display a fractal dimension comprised between 1.9 and 2. These results are very similar to the 1d analysis of fractal dimension along boreholes, where all the values were found to be comprised in the range 0.9 and 1 (in 1*d*). A second method, based on direct observation of densities observed on several 2*d* datasets confirms the former result: the datasets present well defined but weak fractal correlations. We choose therefore to neglect any fractal correlation in the rest of the study by considering ($D = d$).

The orientation distributions of 2*d* outcrops are rather difficult to link with those measured on 1*d* boreholes, even after applying the Terzaghi correction. 1*d* boreholes predict a large number of sub-horizontal fracture planes, while 2*d* outcrops emphasize vertical fractures. We discuss this important issue and argue that the classical Terzaghi correction does not take account of the core size, and is thus partly inappropriate for 1*d* boreholes. At this stage of the analysis process, this result suggests of using orientation distributions derived from outcrop maps rather than from borehole to derive the 3D DFN model. We note that further investigations are necessary to better assess the consistency of the 3D fracture orientation distribution.

The density consistency of the 3D DFN model was determined by analyzing the consistency between the 2*d* model of both outcrops and large-scale maps, and the 1*d* fracture-intercept densities along boreholes. A theoretical expression of P_{10} has been derived as a function of the borehole diameter and the parameters of the 2*d fdf*. In addition, numerical simulations were performed in order to quantify the effects due to non uniform orientation distributions. They show that the orientation effects are much smaller than the effects due to the variations of density, or of the length-scaling exponent.

Two different DFNs have been found to describe the whole available datasets:

- The first DFN model is derived from the *fdf* of the outcrops with fine-grained size lithology, and is valid across all scales investigated in this study, from the highly-fractured cores to large-scale maps. Its best-fitting parameters are : $[a_{2d} = 3, D_{2d} = 2, \alpha_{2d} = 2.01]$ or $[a_{3d} = 4, D_{3d} = 3, \alpha_{3d} = 5.5 \pm 1]$.
- The second DFN model is derived from the *fdf* of the outcrops with coarse-grained size lithology, and is found consistent with cores that present the smallest fracturing intensity. The power-law length exponent is a_{2D} is about equal to 2.2. This model is not found to hold at large scale, which implies a transition scale above which a_{2d} and other distribution parameters should change. Evaluating the transition between small-scale fracture organization and the large-scale one can become an important issue when trying to assess the consequences of the 3D DFN model.

We suggest further investigations to refine this model:

- Deepen the orientation analysis in order to determine how 3D fracture orientation distributions may be extrapolated from 1*d* and 2*d* datasets. It implies the analysis of the consistency between the different datasets when considering orientations bias corrections depending on the length distribution model and data uncertainty.
- There are few indicators of the small-scale limit of the DFN model. This limit remains however important to better constraint further more when considering the role of small fractures on flow dispersivity.
- The granite-type fracture organization is different from the mean distribution model. The spatial and scaling extent of this difference could be better defined.
- A detailed analysis of the relationship between fracture intensity and lithology can be pursued from borehole datasets. For this, it would be useful to define a “lithology” parameter at a coarse scale (let say some tenths of meter) by interacting with geologists.
- Other 2nd-order correlation (fracture length vs fracture density, lithology vs orientation, etc) can be checked.

7 DFN parameters

The parameters, expressed with both notations (see Appendix 0 for relations), are summarized here. Note that it's about the mean global model. Local distinctions are not summarized here but can be found along the report.

The mean global model parameters (related at the outcrop scale to diorite or monzodiorite lithology) are the following:

a_{3d} 4

α_{3d} 5.5 ± 1.0

l_{min} ≤ 0.1 (meter)

k_{3d} 3

r_0 ≤ 0.1 (meter)

$P_{32}(l_{app} = 0.1)$ 43 ± 8

$P_{32}(l_{app} = 1)$ 4.3 ± 0.8

$P_{32}(l_{app} = 10)$ 0.43 ± 0.08

Corrected probability density functions of orientations, $O(\theta,\varphi)$, are provided elsewhere under the form of ascii files for the outcrops data and for the boreholes (see Appendix 5 for indications). Note that the different orientation distributions can be simply coupled by combining and normalizing the probability functions.

In complement, the 3d parameters of the local DFN model corresponding to the outcrops ASM000025 and ASM000026 (granite-like) are:

a_{3d} 3.2 ± 0.05

α_{3d} 2.3 ± 0.3

k_{3d} 2.2 ± 0.05

$P_{32}(l_{app} = 0.1)$ 15.2 ± 4.0

$P_{32}(l_{app} = 1)$ 9.9 ± 3.7

$P_{32}(l_{app} = 10)$ 6.6 ± 3.0

8 References

Bonnet E, Bour O, Odling N, Main I, Davy P, Cowie P, Berkowitz B, 2001. Scaling of Fracture Systems in Geological Media, Reviews of Geophysics, 39, 3, 347–383.

Bour O, Davy P, 1999. Clustering and size distributions of fault patterns: theory and measurements, Geophysical Research Letters, 26 (13), 2,001–2,004.

Bour O, Davy P, Darcel C, Odling N, 2002. A statistical scaling model for fracture network geometry, with validation on a multi-scale mapping of a joint network (Hornelen Basin Norway), J. Geophys. Res., 107, 2113, doi: 2001JB000176.

Cowie P A, Scholz C H, 1992. Physical explanation fort he displacement-length relationship of fault using a post-yield fracture mechanics model, J. Struct. Geol., 14, 1,133–1,148.

Cowie P A, 1998. Normal fault growth in three dimensions in continental and oceanic crust, in Faulting and Magmatism at Mid-Ocean Ridges, Geophys. Monogr. Ser., Vol 106, edited by W. R. Bucket., pp 325–348, AGU, Washington, D. C.

Crave A, Davy P, 1997. Scaling relationships and channel networks from two large-magnitude watersheds in French Brittany, Tectonophysics, 269, 91–111.

Darcel C, 2003. TRUE Block Scale Continuation, Assessment of the feasibility of tracer tests with injection in "background fractures" using a model based on power law fracture length distribution. SKB IPR-03-41, Svensk Kärnbränslehantering AB.

Davy P, Sornette A, Sornette D, 1990. Some consequences of a proposed fractal nature of continental faulting, Nature, 348, 56–58.

Davy P, 1993. On the frequency-length distribution of the San Andreas fault system, J. Geophys. Res., 98, 12, 141–12,151.

Davy P, Hansen A, Bonnet E, Zhang S-Z , 1995. Localization and fault growth in brittle-ductile systems. Implications to deformations of the continental lithosphere, J. Geoph. Res., 100, 6,281–6,294.

Hentschel H G E, Proccacia I, 1983. The infinite number of generalised dimensions of fractals and strange attractors. Physica. Vol 8, 435–444.

Laslett G M, 1982. Censoring and edge effects in areal and line transect sampling of rock joint traces. Journal of the International Association for Mathematical Geology. Vol. 14(2): p 125–140.

Munier R, 2004. Statistical analysis of fracture data, adapted for modelling Discrete Fracture Networks-Version 2, SKB R-04-66, Svensk Kärnbränslehantering AB.

Piggott A R, 1997. Fractal relations for the diameter and trace length of discshaped fractures, J. Geophys. Res., 102, 18,121–18,125.

Schueller S, 2004. Localisation de la deformation et fracturation associée. Etude expérimentale et numérique sur des analogues de la lithosphere continentale. PhD thesis, University of Rennes I.

Appendix 0

Symbols, notations, abbreviations

Index of notations

L characteristic length of a system (ex side L of a cube).

l typical size of a fracture
(ex: for a disc shape fracture, disc diameter in 3d, trace length in 2d).

l_{min} real minimum fracture length (diameter) in the power-law model.

(θ,φ) fracture pole orientation in 3d.

a exponent of the power-law length distribution (notation SKB: k = a –1).

D fractal dimension.

α density term that fixes the density at a given scale of observation.

C_{shape} coefficient related to the fracture shape,
equal to $\pi/4$ if fractures are assumed to be discs.

DFN discrete fracture network.

Power-law model nomenclature

Length exponent

SKB recommends using the following notation for representing the probability density function /Munier, 2004/:

$$f(r) = \frac{k\, r_0^k}{r^{k+1}} \qquad \begin{matrix} k > 0 \\ r_0 > 0 \\ r_0 \le r < \infty \end{matrix}$$

where r_0 is the location parameter (smallest value of r), and k the shape parameter.

In the following we use however the density distribution function as:

$$n(l) = \alpha \cdot l^{-a}$$

where α is a density term, $-a$ the exponent of the power-law model and l the characteristic fracture extension. Note that to simplify the terms, results of the power-law exponent are expressed as positive values, a, agreed that the final power-law exponent is negative.

The corresponding probability density function is:

$$p_{df}(l) = \frac{a-1}{l_{min}^{-a+1}} \cdot l^{-a}$$

it comes directly that:

$$n_{ddf}(l) = n(l) = \alpha\, ' \cdot p_{df}(l) = \alpha \cdot l^{-a}$$

The relations between parameters are simply:

$k = a - 1$

$r_o = l_{\min}$

Density scaling

To encompass the scaling through scale, the *ddf* $n(l)$ is generalized to account for the system size L in which the fracture system is observed. The fracture model is then described by the fracture distribution function $n(l,L)$:

$n(l,L) = \alpha \cdot l^{-a} \cdot L^{D}$,

where D is the fractal dimension.

For a uniform fracture density distribution, D is simply equal to the Euclidean dimension d. In that case, the total number of fractures belonging to a system of linear size L, is simply given by the number of fracture per unit of area (in $2d$) multiplied by the area of interest L^{d}.

Relation between α_{3d} and P_{32}

The 3D fracture density is usually expressed as the fracture area per volume unit, P_{32}. P_{32} can be simply related to the power-law density model of fracture parameters through:

$$P_{32}(l_{\min}) = C_{shape} \frac{\int_{l_{\min}}^{L} \alpha_{3d} \cdot l^{-a_{3d}+2} \cdot L^{D} \cdot dl}{L^3} = C_{shape} \alpha_{3d} \cdot L^{D-3} \cdot \frac{\left[l_{\min}^{-a_{3d}+3} - L^{-a_{3d}+3} \right]}{(a_{3d} - 3)}$$

Similarly the number of fractures per unit volume, P_{30}, is given by:

$$P_{30}(l_{\min}) = \frac{\int_{l_{\min}}^{L} \alpha_{3d} \cdot l^{-a_{3d}} \cdot L^{D} \cdot dl}{L^3} = \alpha_{3d} \cdot L^{D-3} \cdot \frac{\left[l_{\min}^{-a_{3d}+1} - L^{-a_{3d}+1} \right]}{(a_{3d} - 1)}$$

For a fracture system dominated by smallest fractures ($a_{3\mathrm{d}} \geq 3$) it comes that:

$$P_{30}(l_{\min}) = \frac{\int_{l_{\min}}^{L} \alpha_{3d} \cdot l^{-a_{3d}} \cdot L^{D} \cdot dl}{L^3} = \alpha_{3d} \cdot L^{D-3} \cdot \frac{\left[l_{\min}^{-a_{3d}+1} - L^{-a_{3d}+1} \right]}{(a_{3d} - 1)}$$

Note that in practice, values of P_{21} are measured on outcrops for fractures down to a minimum extension, l_{app}, which correspond to the resolution limit or to a pre-fixed cut-off length scale. l_{app} is not necessarily equal to $l_{\min}$ the physically small scale limit of the power-law model. Moreover, l_{app} can be evaluated on outcrops but not along boreholes. In addition, in the perspective of DFN simulations, one can choose to generate the fracture network for fractures down to a certain lower extension, independently of the true physical limit. Then we have:

$$P_{32}(l_{\min}) \sim C_{shape} \alpha_{3d} \cdot L^{D-3} \cdot \frac{l_{\min}^{-a_{3d}+3}}{(a_{3d} - 3)}$$

Then, $\alpha_{3\mathrm{d}}$ is an invariant of the fracture density model which remains independent of resolution or truncation effects, it seems to be more convenient to define the fracture density model.

Although it remains of course worthwhile, P_{32} provides a measure of the fracture density that can entail confusion between scale of resolution regarding measurements and cut-off length scale regarding DFN generation, this especially is the case of a power-law model dominated by smallest fractures ($a_{3d} \geq 3$).

Integrating orientations in the first order model

The first order model description here can be simply completed with consideration of fracture orientations, as long as lengths and orientations can be assumed to be independent. In that case, orientations are handled through the density parameter α:

$$n(\theta,\varphi,l,L) = \alpha \cdot O_{pdf}(\theta,\varphi) \cdot l^{-a} \cdot L^{D}$$

where $O_{pdf}(\theta,\varphi)$ represents the probability distribution function of orientations and α remains the global density term.

Appendix 1

2*d* datasets – overview

What is in this appendix?

We provide here an overview of characteristics related to the two dimensional datasets, with in particular a detailed identification sheet for each of the four outcrops, *asm000025*, *asm000026*, *asm000205*, *asm000206*, *lintopo*, *lin2028* and *lin2027*. Respective geographical positions of each outcrop maps are recalled in Figure A1-1. Resulting measured and interpreted parameters for the outcrops are summed up in the following table. In addition, data related to the scanlines sampled over the four outcrops are given as a complement.

Details for each 2d-outcrop are provided, with the same layout applied for each one as follows:

- Top left: fracture trace map, lower cut-off equal to 0.5 m, including scheme of scanline (*lsm*-), except on *asm000206*.
- Top right: photo of the corresponding outcrop.
- Middle left: fracture trace length density distribution.
- Middle right: integral of correlation $C(r)$.
- Bottom left: discrete stereoplot of fracture poles, Schmidt lower hemisphere projection. (*)
- Bottom right: extrapolated density stereoplot corresponding to previous figure (scales are automatically adjusted for each dataset, therefore can not be directly compared in between). (*)

(*) Note that for 2d-lineament maps, a half rose diagram of strikes is provided instead of stereoplots.

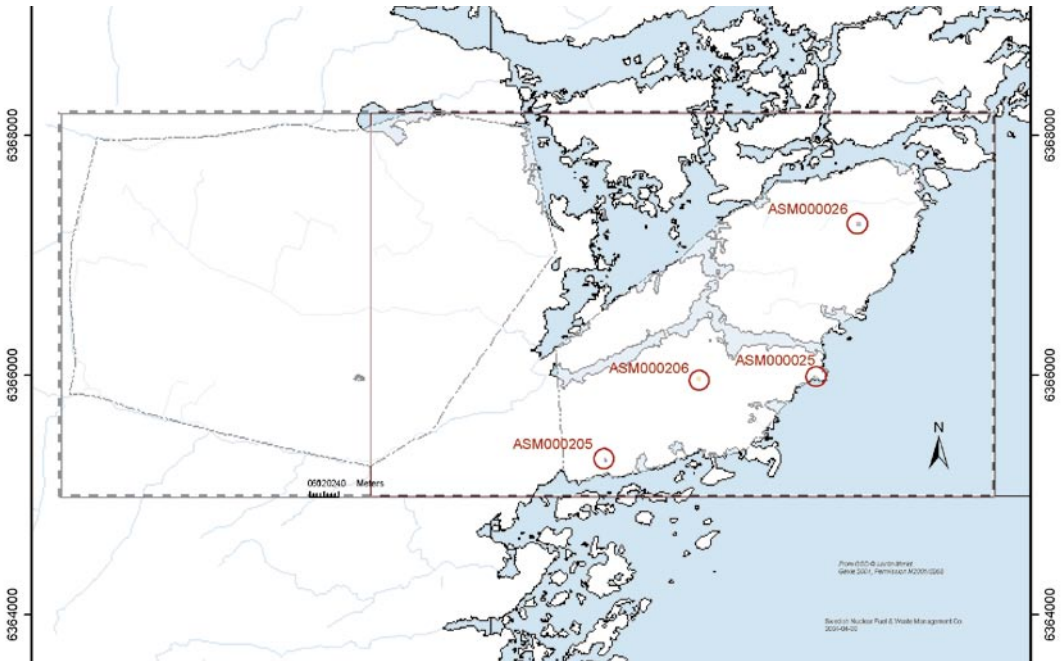

Figure A1-1. *The four outcrops, asm000025, asm000026, asm000205, and asm000206, spatial localization.*

Outcrops characteristics

Reference name	Area (m^2)	P_{20} measured	P_{21} measured	α_{2d} interpreted	a_{2d} interpreted	D_{2d} interpreted	Major rock type
ASM000025		2.19	2.69	1.25	2.15	1.91	501044
(sea view)	418.99						Granite to quartz monzodiorite, generally porphyritic.
							Ävrö granite
ASM000026		1.67	2.13	0.95	2.25	1.88	501044
	523.59						Granite to quartz monzodiorite, generally porphyritic.
							Ävrö granite
ASM000205		5.46	4.97	2.79	2.96	1.96	501030
(close to CLAB)	215.00						Fine-grained dioritoid (Metavolcanite, volcanite)
ASM000206	245.45	3.83	3.19	1.89	3.1	1.95	501036
							Quartz monzonite to monzodiorite, equigranular to weakly porphyritic.
lin_2028					3.0	1.96	
lin_2027					–	1.95	
lin_topo					3.0	1.75	
lin_sweden					3.0	1.84	

And for the scanlines:

Reference name	Outcrop	Number of intercepts	Size (m)	Indicative a_{1d}
LSM000092	ASM000025	40	10	1.75
LSM000093	ASM000025	30	10	
LSM000094	ASM000026	27	10	1.1
LSM000095	ASM000026	30	10	
LSM000096	ASM0002005	48	10	1.8
LSM000097	ASM0000205	46	10	
LSM000098	ASM0000206	34	10	1.7
LSM000099	ASM0000206	30	10	

Outcrop asm000025

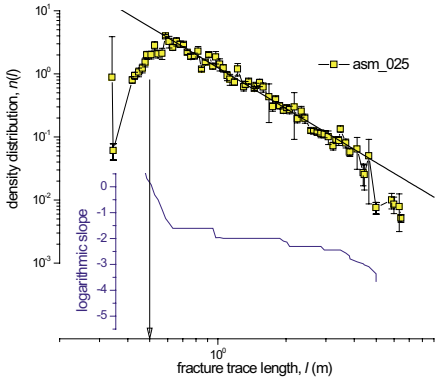

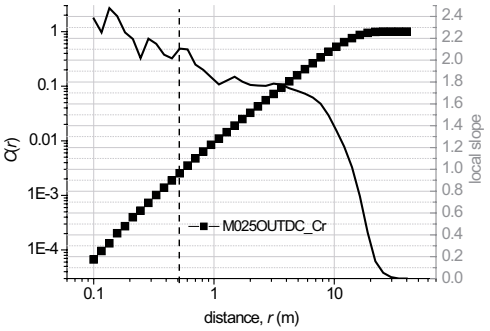

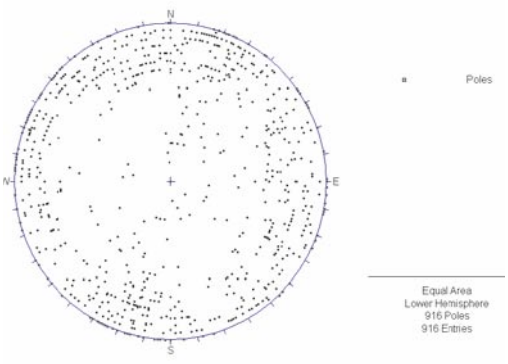

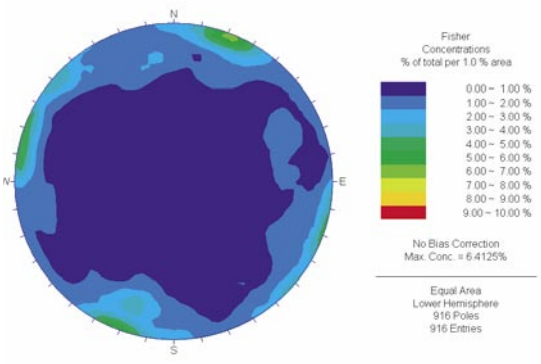

Outcrop asm000026

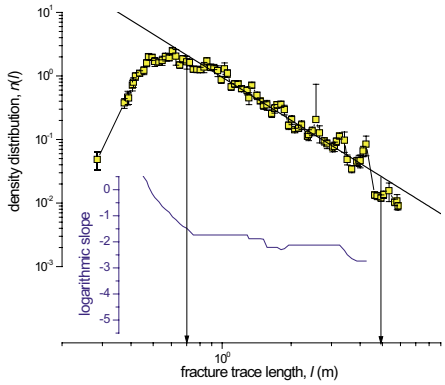

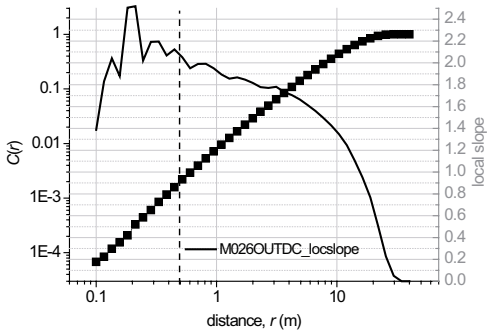

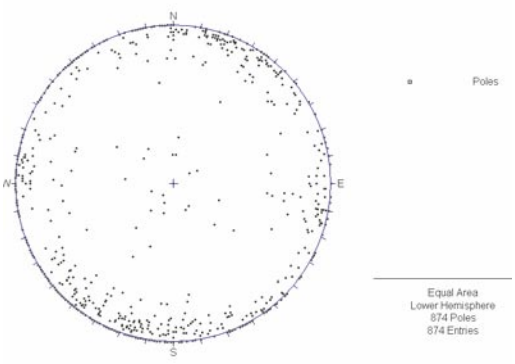

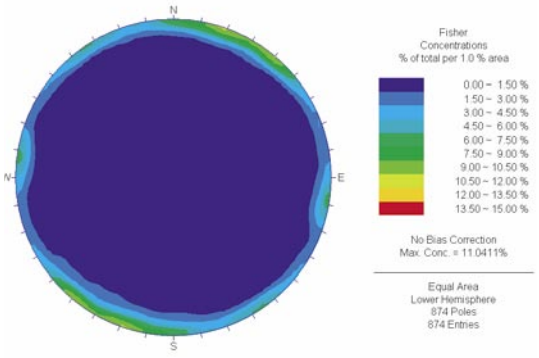

Outcrop asm000205

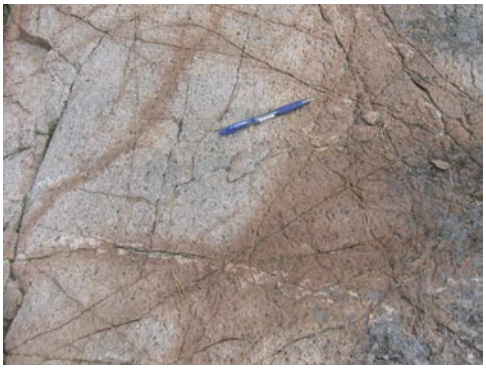

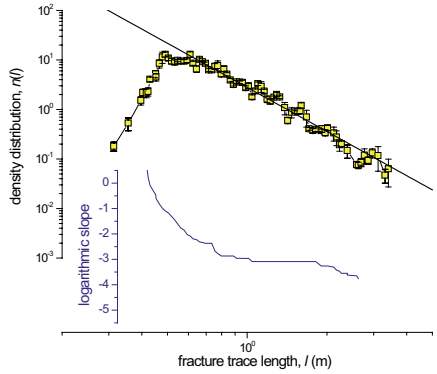

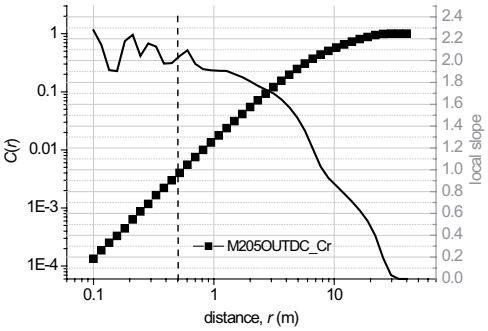

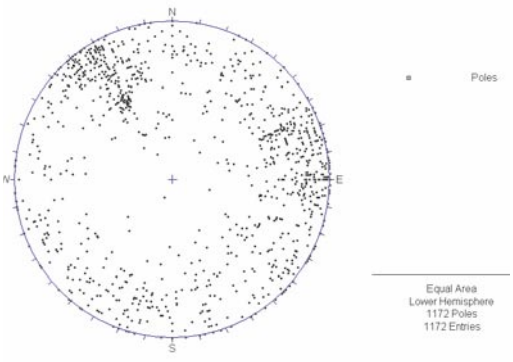

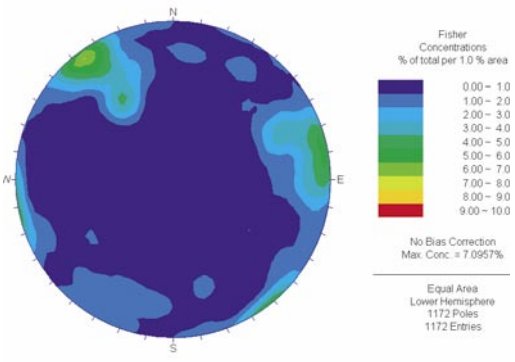

Outcrop asm000206

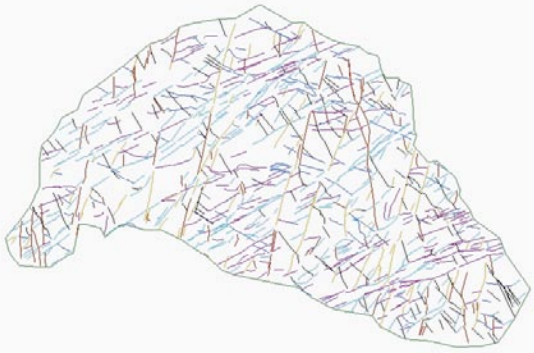

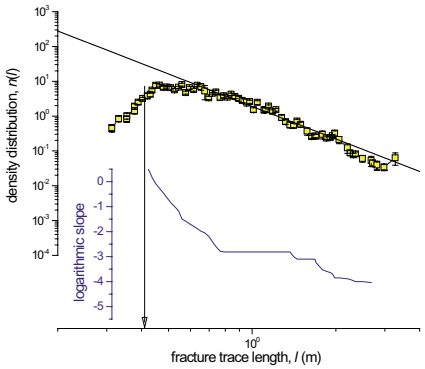

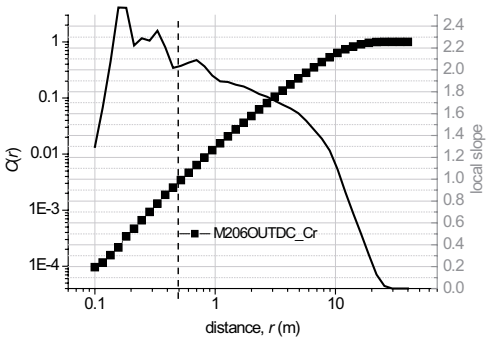

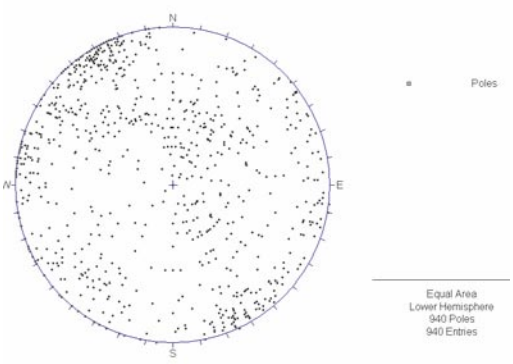

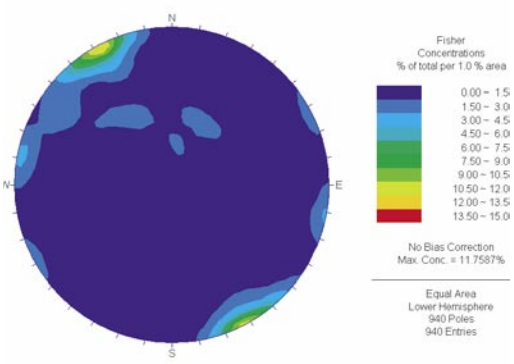

Lin_topo

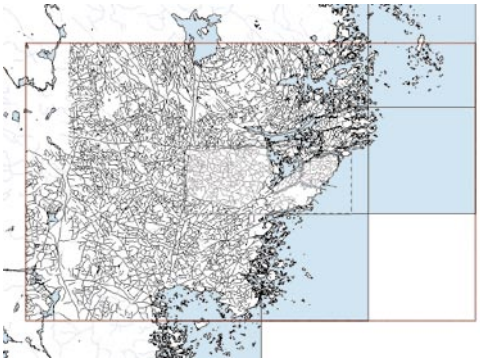

No data

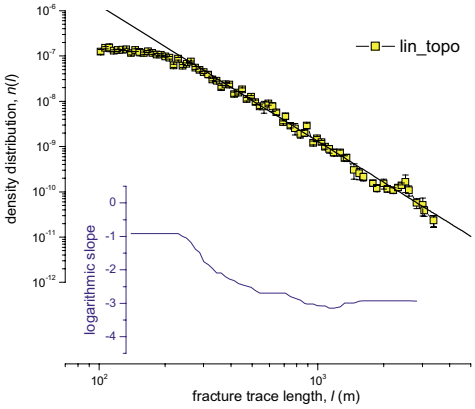

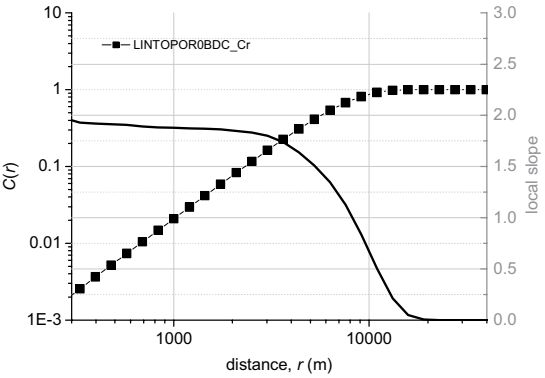

No data

No data

Lin_2028

No data

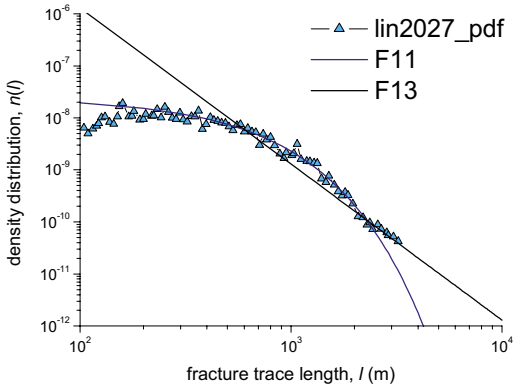

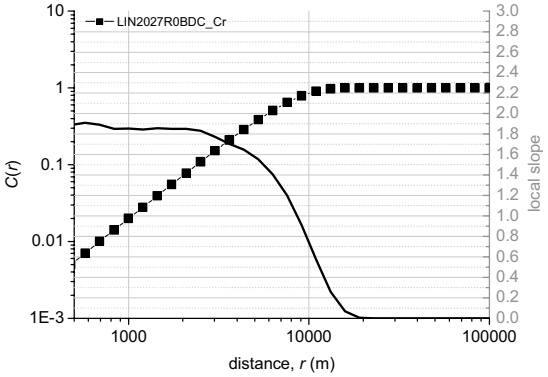

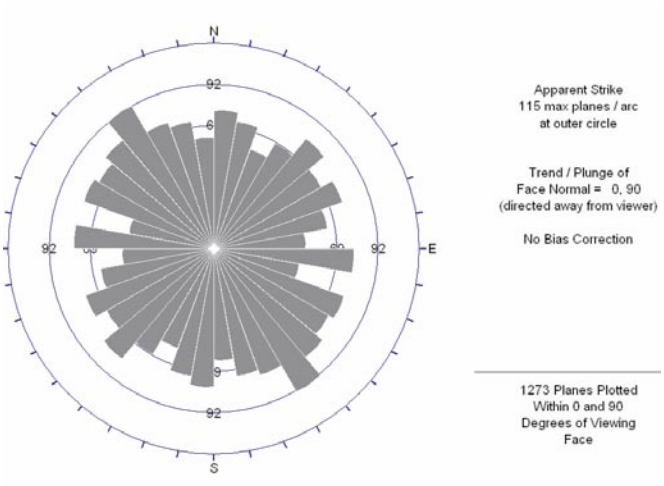

Lin_2027

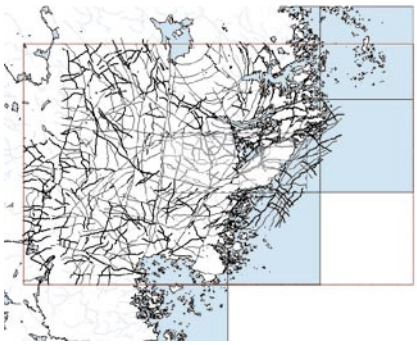

No data

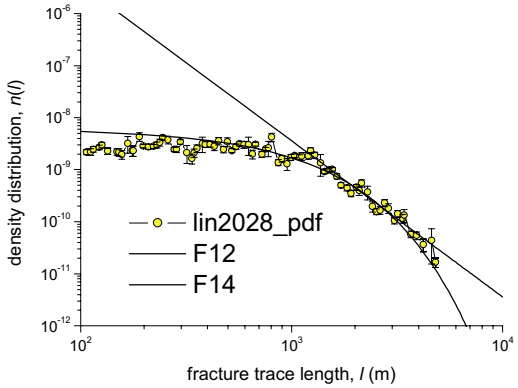

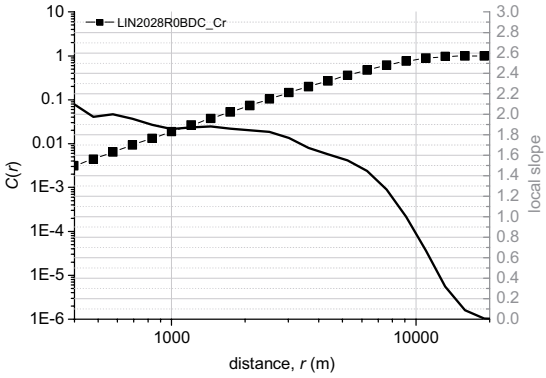

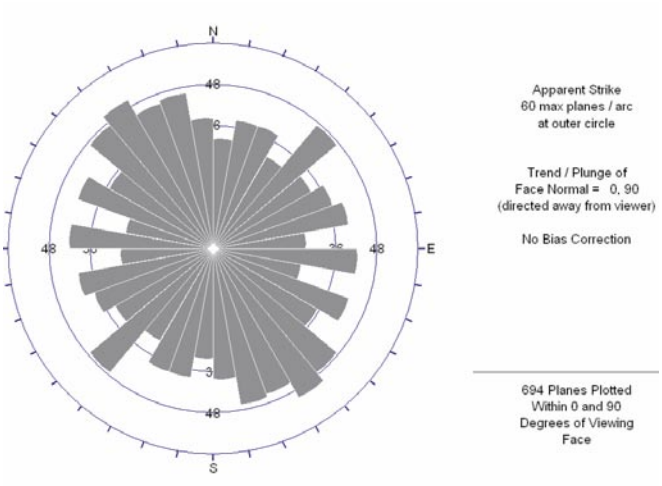

Appendix 2

2*d* datasets, stereoplots

What is in this appendix?

Stereoplots, for all the datasets considered in the report, are displayed in this appendix. This represents a convenient way to have a general idea of fracture orientations with the system studied. All the fractures are simultaneously represented, without distinction between for instance open and sealed ones.

When possible, discrete, contoured and rosette diagrams are provided, as long as corresponding Terzaghi corrected ones. The Schmidt equal area projection in lower hemisphere is selected. Fisher concentrations are chosen to represent contoured stereonets.

For borehole data, the indicative position of borehole orientation is indicated by an arrow.

A basic interpretation in terms of possible fracture sets is provided in A-03 for outcrops asm000025 and asm000205. The way orientation data are used for DFN generation purpose at local scale (linked to a local zone) are provided in A-05.

The software DIPS 5.0 is used to represent the stereoplots.

Layout

We present in next pages Schmidt diagrams of fracture poles with the following layout:

- Top: fracture poles discrete plot.
- Middle left: fracture poles contoured plot.
- Middle right: fracture poles contoured plot after Terzaghi correction.
- Bottom: fracture strikes rosette diagram.

ASM000025

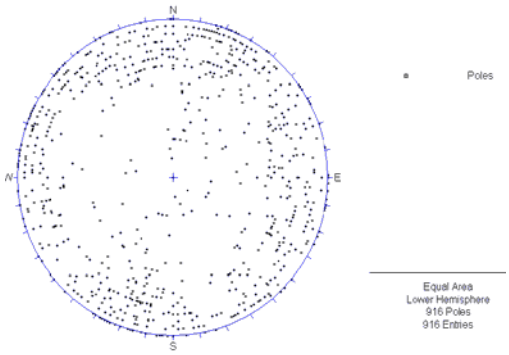
N
W
E
S
Poles
Equal Area
Lower Hemisphere
916 Poles
916 Entries

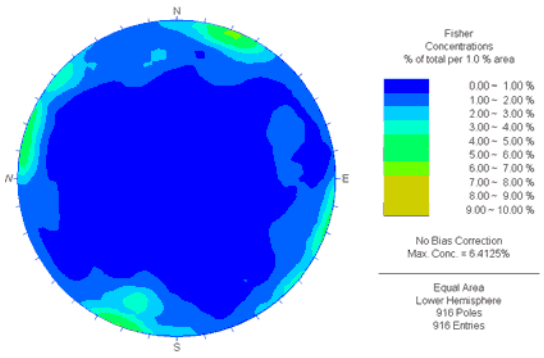
N
W
E
S
Fisher
Concentrations
% of total per 1.0 % area
0.00 ~ 1.00 %
1.00 ~ 2.00 %
2.00 ~ 3.00 %
3.00 ~ 4.00 %
4.00 ~ 5.00 %
5.00 ~ 6.00 %
6.00 ~ 7.00 %
7.00 ~ 8.00 %
8.00 ~ 9.00 %
9.00 ~ 10.00 %
No Bias Correction
Max. Conc. = 6.4125%
Equal Area
Lower Hemisphere
916 Poles
916 Entries

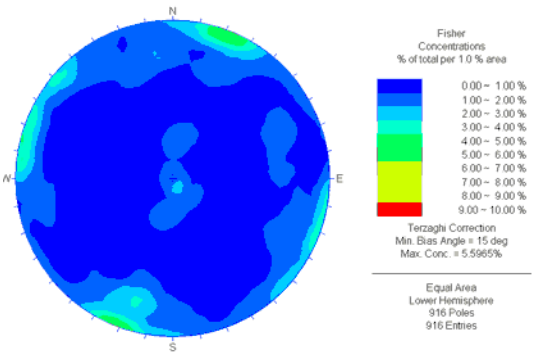
N
W
E
S
Fisher
Concentrations
% of total per 1.0 % area
0.00 ~ 1.00 %
1.00 ~ 2.00 %
2.00 ~ 3.00 %
3.00 ~ 4.00 %
4.00 ~ 5.00 %
5.00 ~ 6.00 %
6.00 ~ 7.00 %
7.00 ~ 8.00 %
8.00 ~ 9.00 %
9.00 ~ 10.00 %
Terzaghi Correction
Min. Bias Angle = 15 deg
Max. Conc. = 5.5965%
Equal Area
Lower Hemisphere
916 Poles
916 Entries

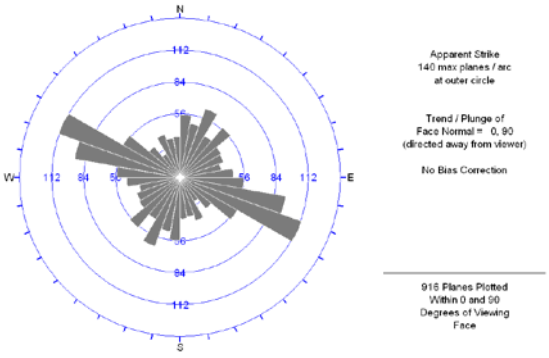
N
W
E
S
112
84
56
Apparent Strike
140 max planes / arc
at outer circle
Trend / Plunge of
Face Normal = 0, 90
(directed away from viewer)
No Bias Correction
916 Planes Plotted
Within 0 and 90
Degrees of Viewing
Face

ASM000026

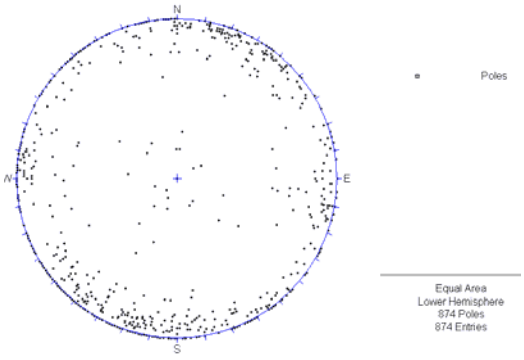
N
W
E
S
Poles
Equal Area
Lower Hemisphere
874 Poles
874 Entries

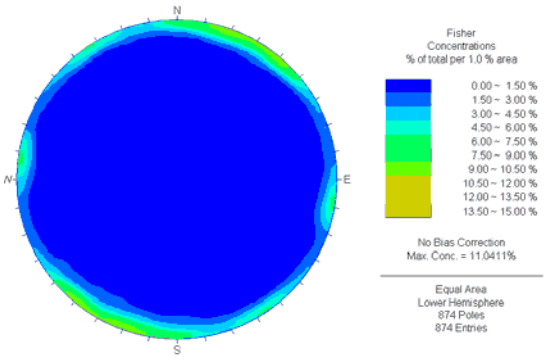
N
W
E
S
Fisher
Concentrations
% of total per 1.0 % area
0.00 ~ 1.50 %
1.50 ~ 3.00 %
3.00 ~ 4.50 %
4.50 ~ 6.00 %
6.00 ~ 7.50 %
7.50 ~ 9.00 %
9.00 ~ 10.50 %
10.50 ~ 12.00 %
12.00 ~ 13.50 %
13.50 ~ 15.00 %
No Bias Correction
Max. Conc. = 11.0411%
Equal Area
Lower Hemisphere
874 Poles
874 Entries

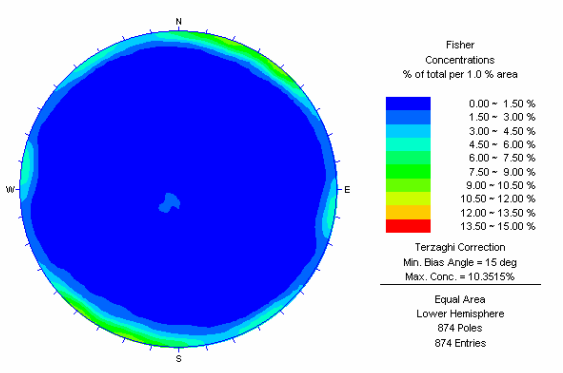
N
W
E
S
Fisher
Concentrations
% of total per 1.0 % area
0.00 ~ 1.50 %
1.50 ~ 3.00 %
3.00 ~ 4.50 %
4.50 ~ 6.00 %
6.00 ~ 7.50 %
7.50 ~ 9.00 %
9.00 ~ 10.50 %
10.50 ~ 12.00 %
12.00 ~ 13.50 %
13.50 ~ 15.00 %
Terzaghi Correction
Min. Bias Angle = 15 deg
Max. Conc. = 10.3515%
Equal Area
Lower Hemisphere
874 Poles
874 Entries

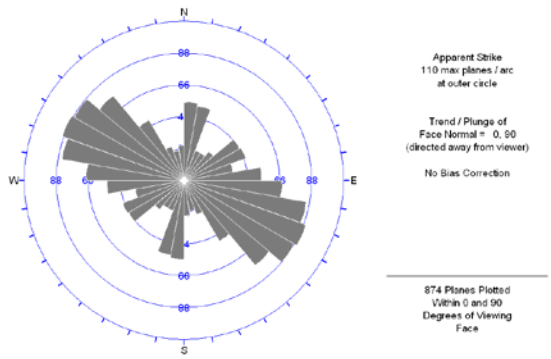
N
W
E
S
Apparent Strike
110 max planes / arc
at outer circle
Trend / Plunge of
Face Normal = 0, 90
(directed away from viewer)
No Bias Correction
874 Planes Plotted
Within 0 and 90
Degrees of Viewing
Face

ASM000205

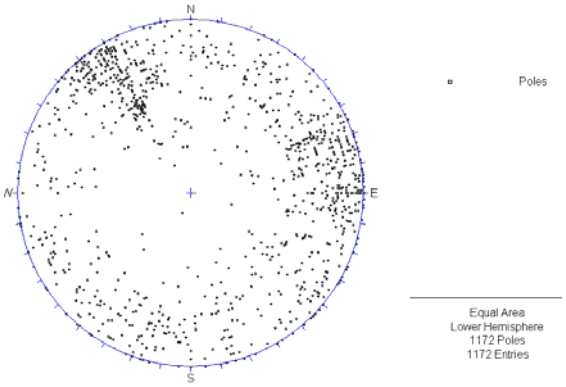
N
W
E
S
Poles
Equal Area
Lower Hemisphere
1172 Poles
1172 Entries

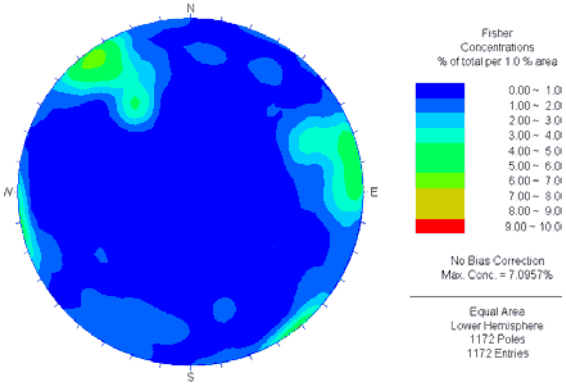
N
W
E
S
Fisher
Concentrations
% of total per 1.0 % area
0.00 ~ 1.0
1.00 ~ 2.0
2.00 ~ 3.0
3.00 ~ 4.0
4.00 ~ 5.0
5.00 ~ 6.0
6.00 ~ 7.0
7.00 ~ 8.0
8.00 ~ 9.0
9.00 ~ 10.0
No Bias Correction
Max. Conc. = 7.0957%
Equal Area
Lower Hemisphere
1172 Poles
1172 Entries

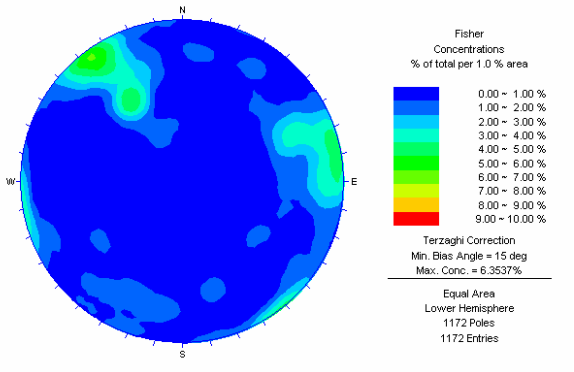
N
W
E
S
Fisher
Concentrations
% of total per 1.0 % area
0.00 ~ 1.00 %
1.00 ~ 2.00 %
2.00 ~ 3.00 %
3.00 ~ 4.00 %
4.00 ~ 5.00 %
5.00 ~ 6.00 %
6.00 ~ 7.00 %
7.00 ~ 8.00 %
8.00 ~ 9.00 %
9.00 ~ 10.00 %
Terzaghi Correction
Min. Bias Angle = 15 deg
Max. Conc. = 6.3537%
Equal Area
Lower Hemisphere
1172 Poles
1172 Entries

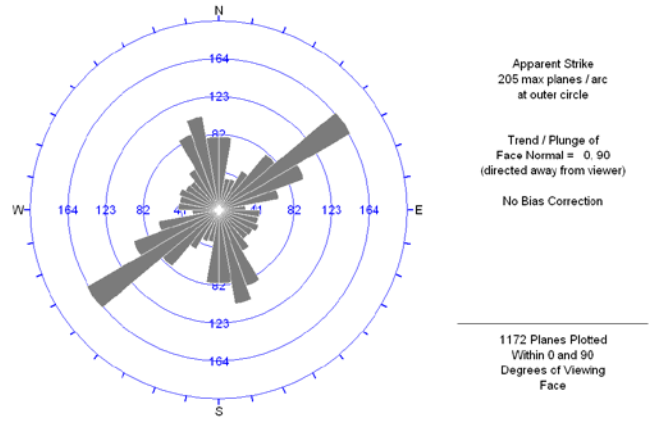
N
W
E
S
164
123
82
41
Apparent Strike
205 max planes / arc
at outer circle
Trend / Plunge of
Face Normal = 0, 90
(directed away from viewer)
No Bias Correction
1172 Planes Plotted
Within 0 and 90
Degrees of Viewing
Face

ASM000206

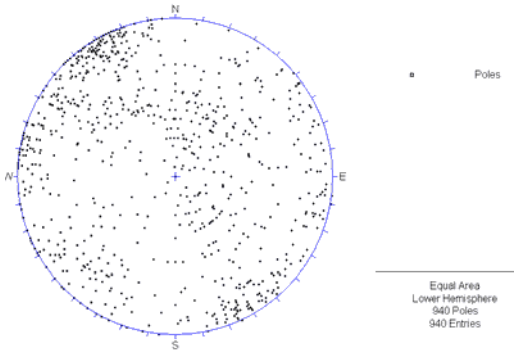
N
W
E
S
Poles
Equal Area
Lower Hemisphere
940 Poles
940 Entries

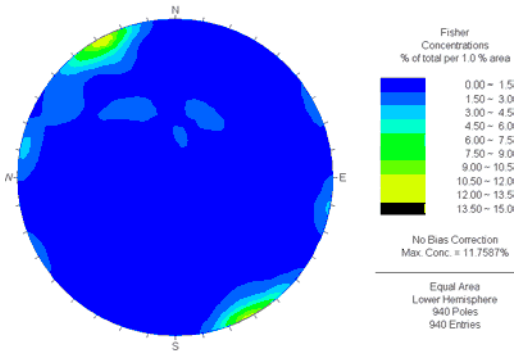
N
W
E
S
Fisher
Concentrations
% of total per 1.0 % area
0.00 ~ 1.5
1.50 ~ 3.0
3.00 ~ 4.5
4.50 ~ 6.0
6.00 ~ 7.5
7.50 ~ 9.0
9.00 ~ 10.5
10.50 ~ 12.0
12.00 ~ 13.5
13.50 ~ 15.0
No Bias Correction
Max. Conc. = 11.7587%
Equal Area
Lower Hemisphere
940 Poles
940 Entries

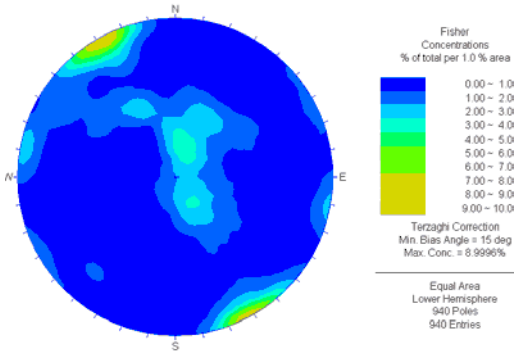
N
W
E
S
Fisher
Concentrations
% of total per 1.0 % area
0.00 ~ 1.0
1.00 ~ 2.0
2.00 ~ 3.0
3.00 ~ 4.0
4.00 ~ 5.0
5.00 ~ 6.0
6.00 ~ 7.0
7.00 ~ 8.0
8.00 ~ 9.0
9.00 ~ 10.0
Terzaghi Correction
Min. Bias Angle = 15 deg
Max. Conc. = 8.9996%
Equal Area
Lower Hemisphere
940 Poles
940 Entries

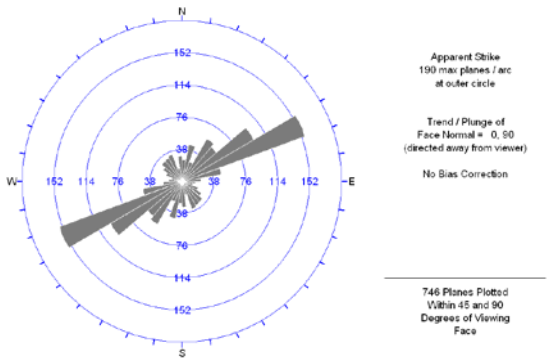
N
W
E
S
152
114
76
38
Apparent Strike
190 max planes / arc
at outer circle
Trend / Plunge of
Face Normal = 0, 90
(directed away from viewer)
No Bias Correction
746 Planes Plotted
Within 45 and 90
Degrees of Viewing
Face

HSH01

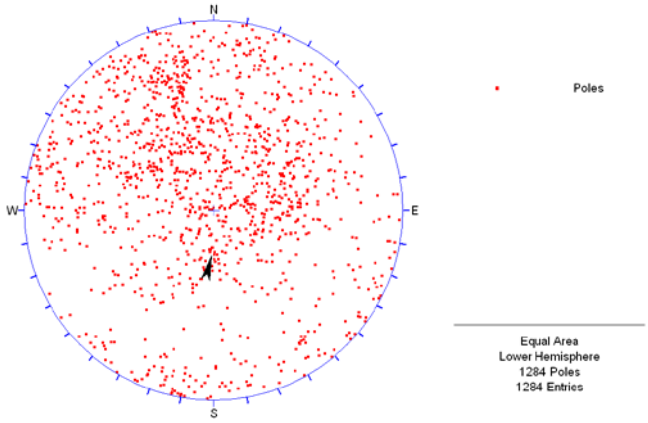
N
W
E
S
Poles
Equal Area
Lower Hemisphere
1284 Poles
1284 Entries

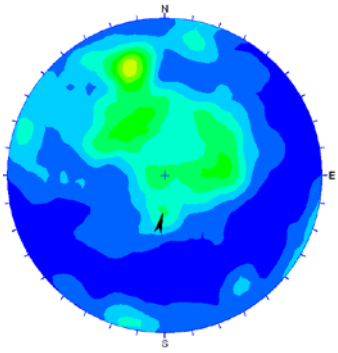
N
E
S

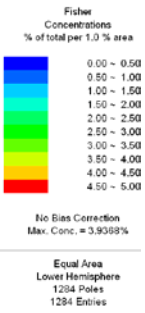
Fisher
Concentrations
% of total per 1.0 % area
0.00 ~ 0.50
0.50 ~ 1.00
1.00 ~ 1.50
1.50 ~ 2.00
2.00 ~ 2.50
2.50 ~ 3.00
3.00 ~ 3.50
3.50 ~ 4.00
4.00 ~ 4.50
4.50 ~ 5.00
No Bias Correction
Max. Conc. = 3.9368%
Equal Area
Lower Hemisphere
1284 Poles
1284 Entries


N
E
S

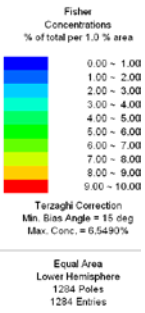
Fisher
Concentrations
% of total per 1.0 % area
0.00 ~ 1.00
1.00 ~ 2.00
2.00 ~ 3.00
3.00 ~ 4.00
4.00 ~ 5.00
5.00 ~ 6.00
6.00 ~ 7.00
7.00 ~ 8.00
8.00 ~ 9.00
9.00 ~ 10.00
Terzaghi Correction
Min. Bias Angle = 15 deg
Max. Conc. = 6.5490%
Equal Area
Lower Hemisphere
1284 Poles
1284 Entries

HSH02

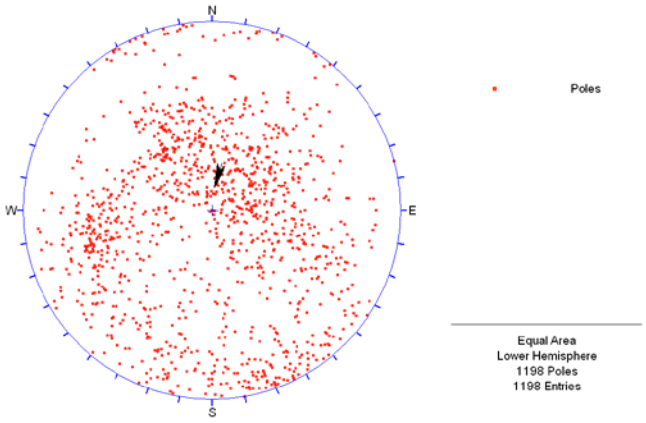
N
W
E
S
Poles
Equal Area
Lower Hemisphere
1198 Poles
1198 Entries

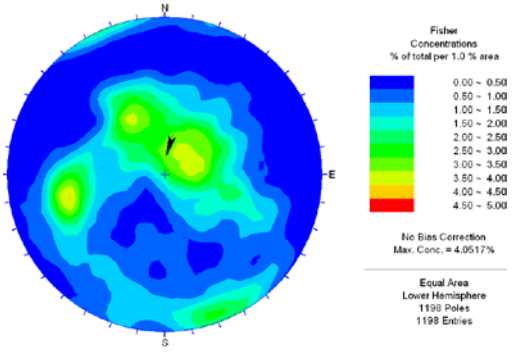
N
E
S
Fisher
Concentrations
% of total per 1.0 % area
0.00 ~ 0.50
0.50 ~ 1.00
1.00 ~ 1.50
1.50 ~ 2.00
2.00 ~ 2.50
2.50 ~ 3.00
3.00 ~ 3.50
3.50 ~ 4.00
4.00 ~ 4.50
4.50 ~ 5.00
No Bias Correction
Max. Conc. = 4.0517%
Equal Area
Lower Hemisphere
1198 Poles
1198 Entries

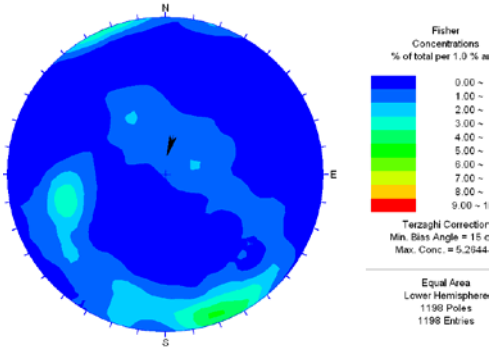
N
E
S
Fisher
Concentrations
% of total per 1.0 % a
0.00 ~
1.00 ~
2.00 ~
3.00 ~
4.00 ~
5.00 ~
6.00 ~
7.00 ~
8.00 ~
9.00 ~ 1
Terzaghi Correction
Min. Bias Angle = 15 c
Max. Conc. = 5.2944
Equal Area
Lower Hemisphere
1198 Poles
1198 Entries

HSH03

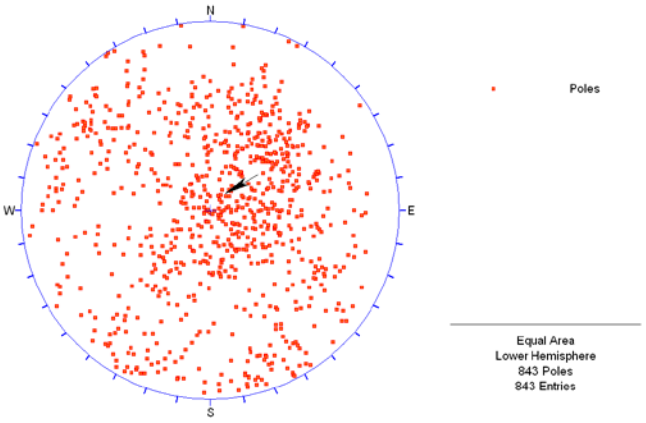
N
W
E
S
Poles
Equal Area
Lower Hemisphere
843 Poles
843 Entries

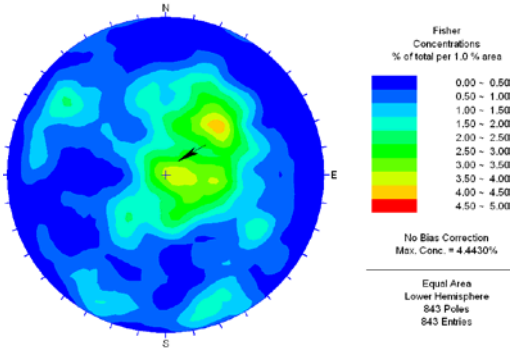
N
E
S
Fisher
Concentrations
% of total per 1.0 % area
0.00 ~ 0.50
0.50 ~ 1.00
1.00 ~ 1.50
1.50 ~ 2.00
2.00 ~ 2.50
2.50 ~ 3.00
3.00 ~ 3.50
3.50 ~ 4.00
4.00 ~ 4.50
4.50 ~ 5.00
No Bias Correction
Max. Conc. = 4.4430%
Equal Area
Lower Hemisphere
843 Poles
843 Entries

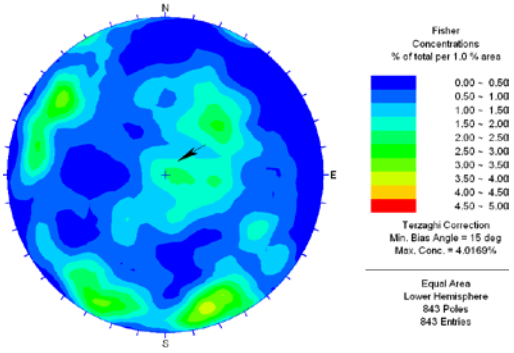
N
E
S
Fisher
Concentrations
% of total per 1.0 % area
0.00 ~ 0.50
0.50 ~ 1.00
1.00 ~ 1.50
1.50 ~ 2.00
2.00 ~ 2.50
2.50 ~ 3.00
3.00 ~ 3.50
3.50 ~ 4.00
4.00 ~ 4.50
4.50 ~ 5.00
Terzaghi Correction
Min. Bias Angle = 15 deg
Max. Conc. = 4.0169%
Equal Area
Lower Hemisphere
843 Poles
843 Entries

KAV01

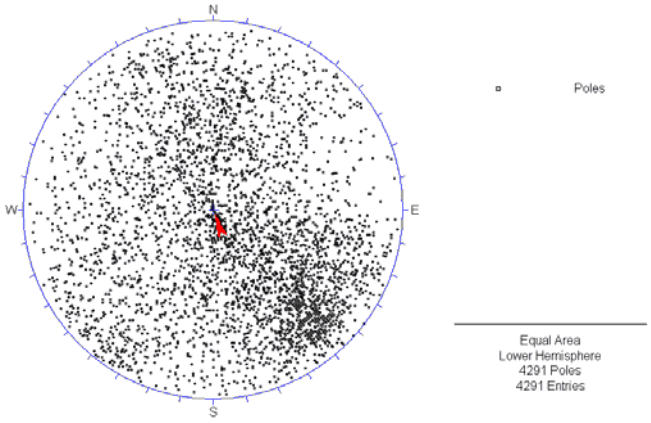
N
W
E
S
Poles
Equal Area
Lower Hemisphere
4291 Poles
4291 Entries

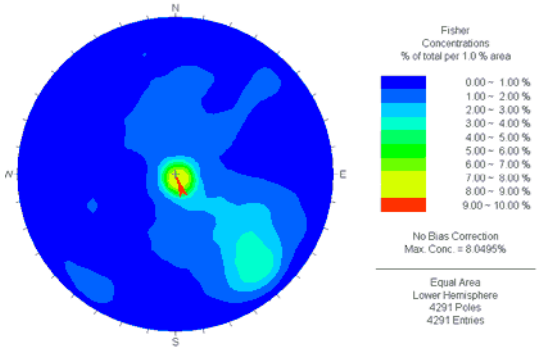
N
W
E
S
Fisher
Concentrations
% of total per 1.0 % area
0.00 ~ 1.00 %
1.00 ~ 2.00 %
2.00 ~ 3.00 %
3.00 ~ 4.00 %
4.00 ~ 5.00 %
5.00 ~ 6.00 %
6.00 ~ 7.00 %
7.00 ~ 8.00 %
8.00 ~ 9.00 %
9.00 ~ 10.00 %
No Bias Correction
Max. Conc. = 8.0495%
Equal Area
Lower Hemisphere
4291 Poles
4291 Entries

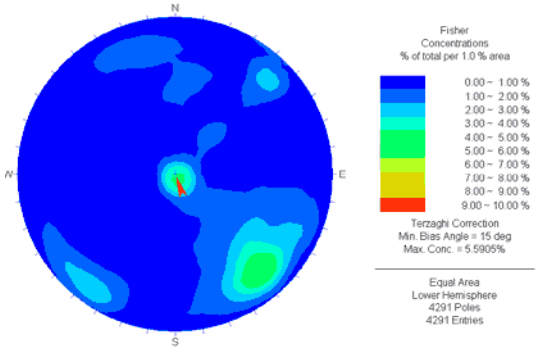
N
W
E
S
Fisher
Concentrations
% of total per 1.0 % area
0.00 ~ 1.00 %
1.00 ~ 2.00 %
2.00 ~ 3.00 %
3.00 ~ 4.00 %
4.00 ~ 5.00 %
5.00 ~ 6.00 %
6.00 ~ 7.00 %
7.00 ~ 8.00 %
8.00 ~ 9.00 %
9.00 ~ 10.00 %
Terzaghi Correction
Min. Bias Angle = 15 deg
Max. Conc. = 5.5905%
Equal Area
Lower Hemisphere
4291 Poles
4291 Entries

KLX02

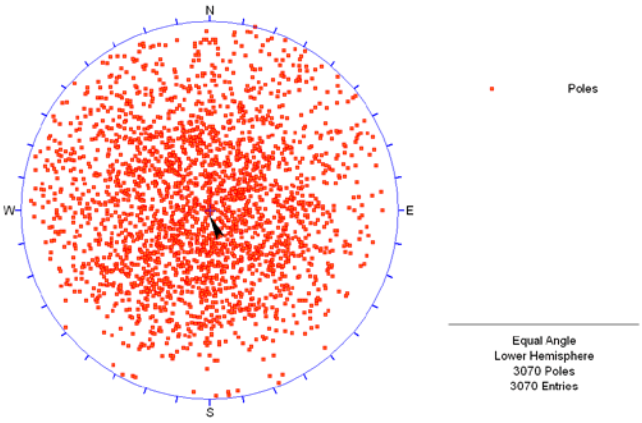
N
W
E
S
Poles
Equal Angle
Lower Hemisphere
3070 Poles
3070 Entries

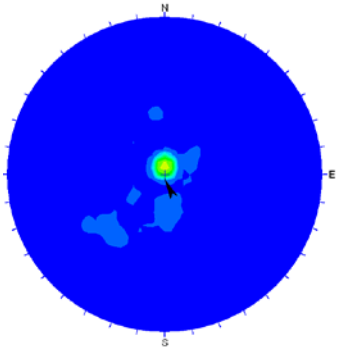
N
E
S

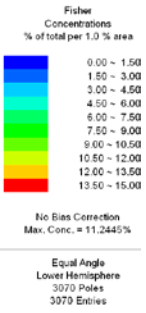
Fisher
Concentrations
% of total per 1.0 % area
0.00 ~ 1.50
1.50 ~ 3.00
3.00 ~ 4.50
4.50 ~ 6.00
6.00 ~ 7.50
7.50 ~ 9.00
9.00 ~ 10.50
10.50 ~ 12.00
12.00 ~ 13.50
13.50 ~ 15.00
No Bias Correction
Max. Conc. = 11.2445%
Equal Angle
Lower Hemisphere
3070 Poles
3070 Entries

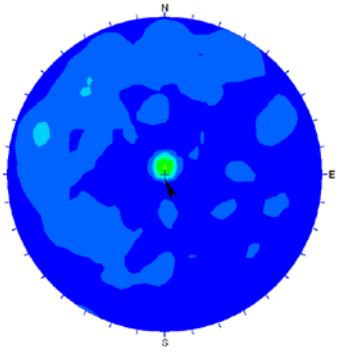
N
E
S

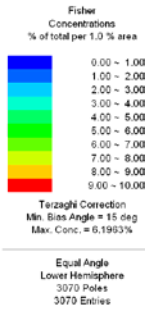
Fisher
Concentrations
% of total per 1.0 % area
0.00 ~ 1.00
1.00 ~ 2.00
2.00 ~ 3.00
3.00 ~ 4.00
4.00 ~ 5.00
5.00 ~ 6.00
6.00 ~ 7.00
7.00 ~ 8.00
8.00 ~ 9.00
9.00 ~ 10.00
Terzaghi Correction
Min. Bias Angle = 15 deg
Max. Conc. = 6.1963%
Equal Angle
Lower Hemisphere
3070 Poles
3070 Entries

KSH01A

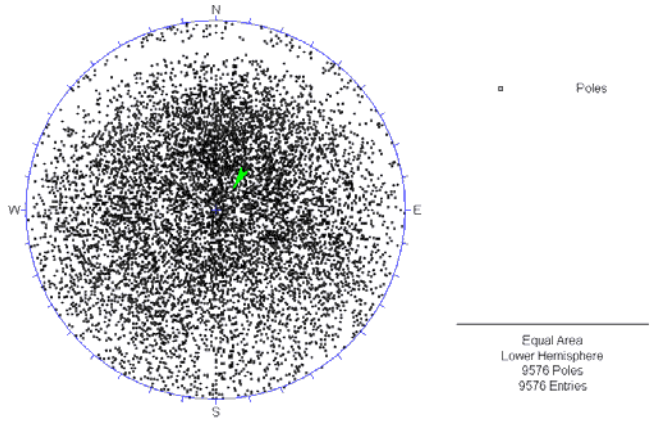
N
W
E
S
Poles
Equal Area
Lower Hemisphere
9576 Poles
9576 Entries

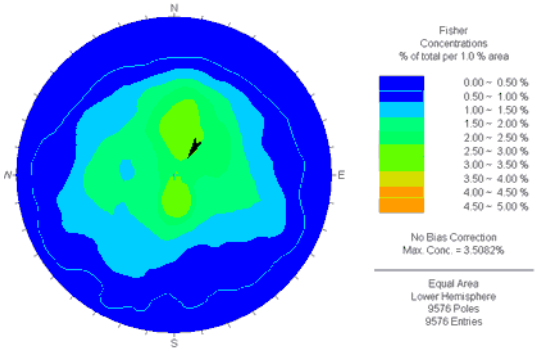
N
W
E
S
Fisher
Concentrations
% of total per 1.0 % area
0.00 ~ 0.50 %
0.50 ~ 1.00 %
1.00 ~ 1.50 %
1.50 ~ 2.00 %
2.00 ~ 2.50 %
2.50 ~ 3.00 %
3.00 ~ 3.50 %
3.50 ~ 4.00 %
4.00 ~ 4.50 %
4.50 ~ 5.00 %
No Bias Correction
Max. Conc. = 3.5082%
Equal Area
Lower Hemisphere
9576 Poles
9576 Entries

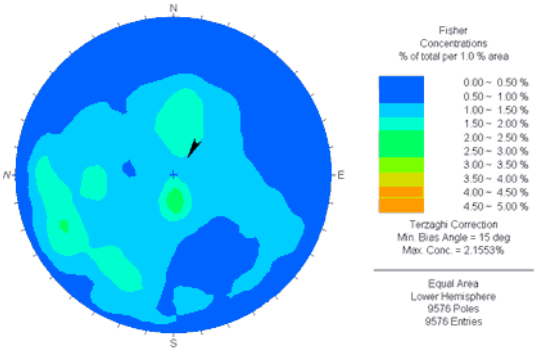
N
W
E
S
Fisher
Concentrations
% of total per 1.0 % area
0.00 ~ 0.50 %
0.50 ~ 1.00 %
1.00 ~ 1.50 %
1.50 ~ 2.00 %
2.00 ~ 2.50 %
2.50 ~ 3.00 %
3.00 ~ 3.50 %
3.50 ~ 4.00 %
4.00 ~ 4.50 %
4.50 ~ 5.00 %
Terzaghi Correction
Min. Bias Angle = 15 deg
Max. Conc. = 2.1553%
Equal Area
Lower Hemisphere
9576 Poles
9576 Entries

KSH01B

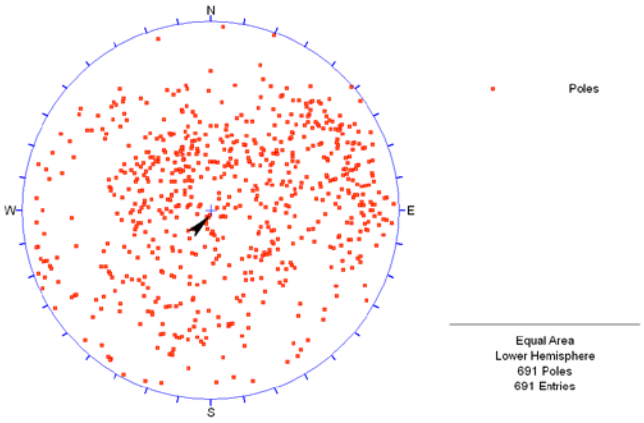
N
W
E
S
Poles
Equal Area
Lower Hemisphere
691 Poles
691 Entries

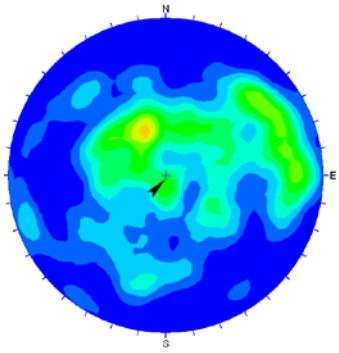
N
E
S

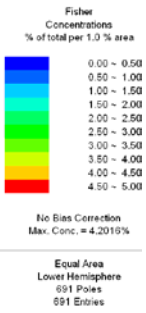
Fisher
Concentrations
% of total per 1.0 % area
0.00 ~ 0.50
0.50 ~ 1.00
1.00 ~ 1.50
1.50 ~ 2.00
2.00 ~ 2.50
2.50 ~ 3.00
3.00 ~ 3.50
3.50 ~ 4.00
4.00 ~ 4.50
4.50 ~ 5.00
No Bias Correction
Max. Conc. = 4.2016%
Equal Area
Lower Hemisphere
691 Poles
691 Entries

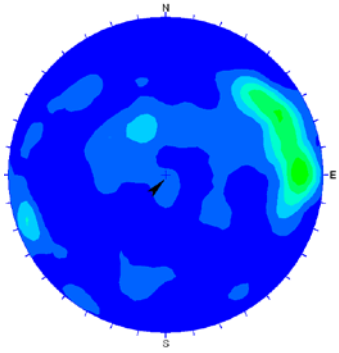
N
E
S

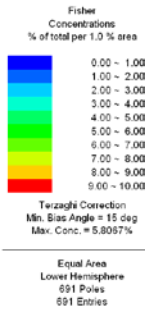
Fisher
Concentrations
% of total per 1.0 % area
0.00 ~ 1.00
1.00 ~ 2.00
2.00 ~ 3.00
3.00 ~ 4.00
4.00 ~ 5.00
5.00 ~ 6.00
6.00 ~ 7.00
7.00 ~ 8.00
8.00 ~ 9.00
9.00 ~ 10.00
Terzaghi Correction
Min. Bias Angle = 15 deg
Max. Conc. = 5.8067%
Equal Area
Lower Hemisphere
691 Poles
691 Entries

KSH02

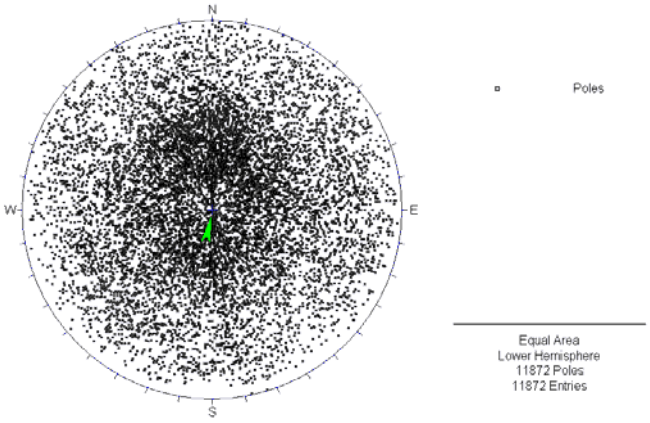
N
W
E
S
Poles
Equal Area
Lower Hemisphere
11872 Poles
11872 Entries

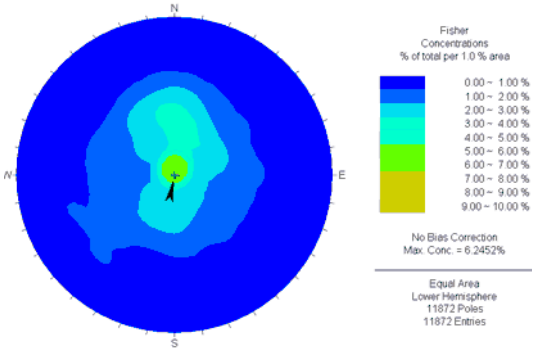
N
W
E
S
Fisher
Concentrations
% of total per 1.0 % area
0.00 ~ 1.00 %
1.00 ~ 2.00 %
2.00 ~ 3.00 %
3.00 ~ 4.00 %
4.00 ~ 5.00 %
5.00 ~ 6.00 %
6.00 ~ 7.00 %
7.00 ~ 8.00 %
8.00 ~ 9.00 %
9.00 ~ 10.00 %
No Bias Correction
Max. Conc. = 6.2452%
Equal Area
Lower Hemisphere
11872 Poles
11872 Entries

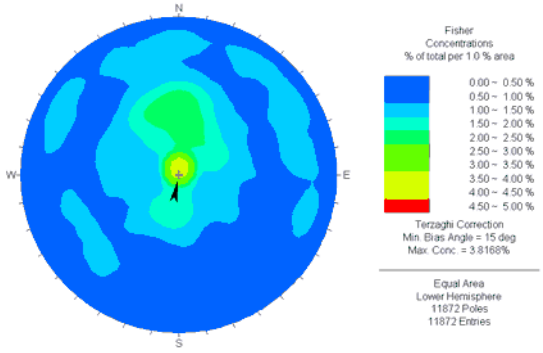
N
W
E
S
Fisher
Concentrations
% of total per 1.0 % area
0.00 ~ 0.50 %
0.50 ~ 1.00 %
1.00 ~ 1.50 %
1.50 ~ 2.00 %
2.00 ~ 2.50 %
2.50 ~ 3.00 %
3.00 ~ 3.50 %
3.50 ~ 4.00 %
4.00 ~ 4.50 %
4.50 ~ 5.00 %
Terzaghi Correction
Min. Bias Angle = 15 deg
Max. Conc. = 3.8168%
Equal Area
Lower Hemisphere
11872 Poles
11872 Entries

KSH03A

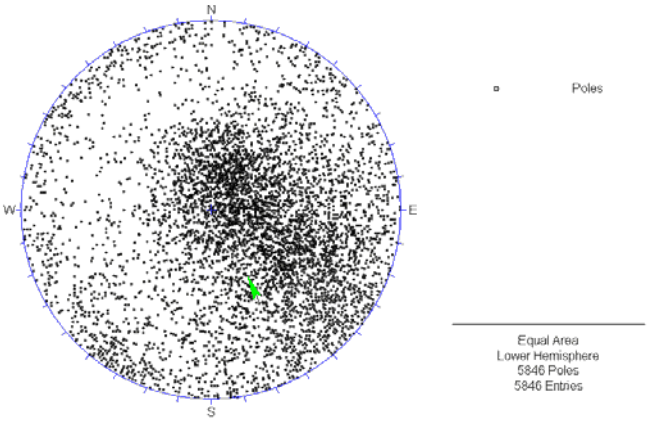
N
W
E
S
Poles
Equal Area
Lower Hemisphere
5846 Poles
5846 Entries

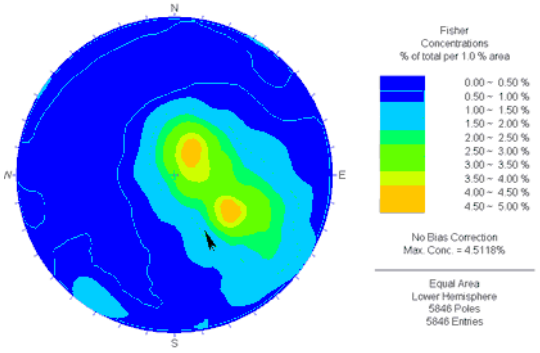
N
W
E
S
Fisher
Concentrations
% of total per 1.0 % area
0.00 ~ 0.50 %
0.50 ~ 1.00 %
1.00 ~ 1.50 %
1.50 ~ 2.00 %
2.00 ~ 2.50 %
2.50 ~ 3.00 %
3.00 ~ 3.50 %
3.50 ~ 4.00 %
4.00 ~ 4.50 %
4.50 ~ 5.00 %
No Bias Correction
Max. Conc. = 4.5118%
Equal Area
Lower Hemisphere
5846 Poles
5846 Entries

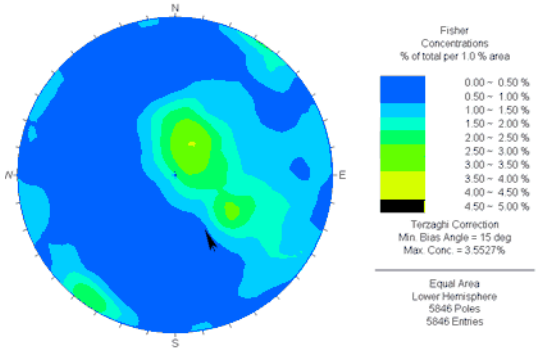
N
W
E
S
Fisher
Concentrations
% of total per 1.0 % area
0.00 ~ 0.50 %
0.50 ~ 1.00 %
1.00 ~ 1.50 %
1.50 ~ 2.00 %
2.00 ~ 2.50 %
2.50 ~ 3.00 %
3.00 ~ 3.50 %
3.50 ~ 4.00 %
4.00 ~ 4.50 %
4.50 ~ 5.00 %
Terzaghi Correction
Min. Bias Angle = 15 deg
Max. Conc. = 3.5527%
Equal Area
Lower Hemisphere
5846 Poles
5846 Entries

KSH03B

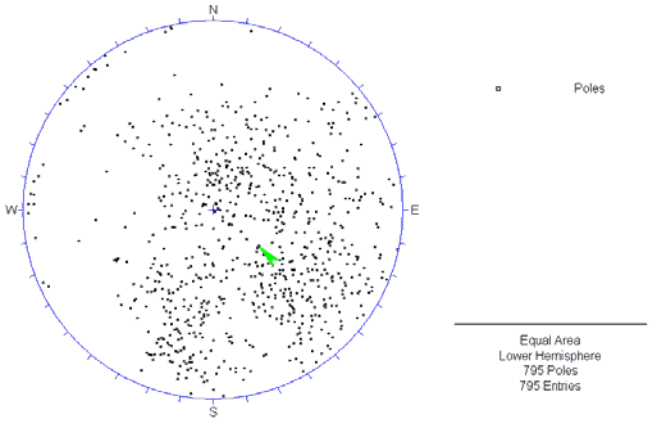
N
W
E
S
Poles
Equal Area
Lower Hemisphere
795 Poles
795 Entries

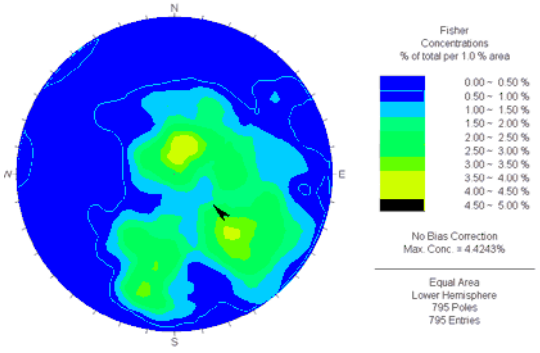
N
W
E
S
Fisher
Concentrations
% of total per 1.0 % area
0.00 ~ 0.50 %
0.50 ~ 1.00 %
1.00 ~ 1.50 %
1.50 ~ 2.00 %
2.00 ~ 2.50 %
2.50 ~ 3.00 %
3.00 ~ 3.50 %
3.50 ~ 4.00 %
4.00 ~ 4.50 %
4.50 ~ 5.00 %
No Bias Correction
Max. Conc. = 4.4243%
Equal Area
Lower Hemisphere
795 Poles
795 Entries

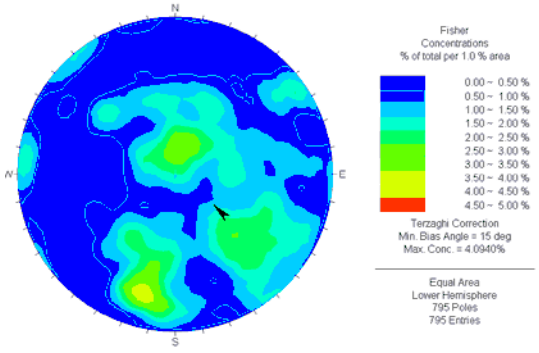
N
W
E
S
Fisher
Concentrations
% of total per 1.0 % area
0.00 ~ 0.50 %
0.50 ~ 1.00 %
1.00 ~ 1.50 %
1.50 ~ 2.00 %
2.00 ~ 2.50 %
2.50 ~ 3.00 %
3.00 ~ 3.50 %
3.50 ~ 4.00 %
4.00 ~ 4.50 %
4.50 ~ 5.00 %
Terzaghi Correction
Min. Bias Angle = 15 deg
Max. Conc. = 4.0940%
Equal Area
Lower Hemisphere
795 Poles
795 Entries

Appendix 3

Fracture set based analysis on *asm*000025 and *asm*000205

What is in this appendix?

A first order fracture set analysis is provided for outcrop *asm*000025 and *asm*000205. It is dedicated to assess the first order geometrical DFN model. It includes the fracture set distinction and the subsequent length distribution analysis. The fracture set distinction is mainly based on strike distinction. The fracture set analysis could be refined; this would however entail many modelling questions (see main text). Therefore we chose this simple method to distinct between fracture sets.

Note that at this stage, we prefer the boostrapping method for generation purposes (see Appendix 5).

Fracture sets

The distinction in fracture sets is firstly based on the contoured stereonet qualitative observation. The orientation distribution is dominated by sub-horizontal fractures. Three zones of higher intensity appear for the sub-horizontal fractures (see illustration just below, right).

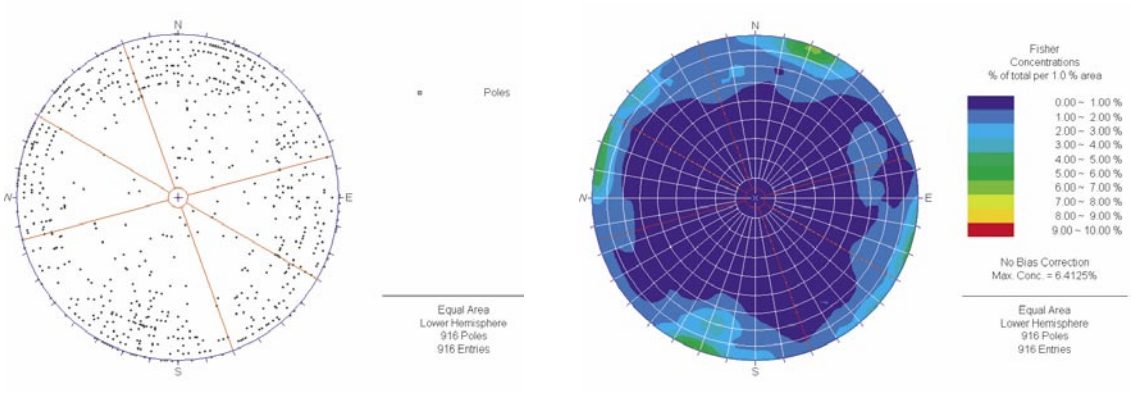

Figure A3-1. *Outcrop asm000025, stereonets with fracture sets symbolized as red lines.*

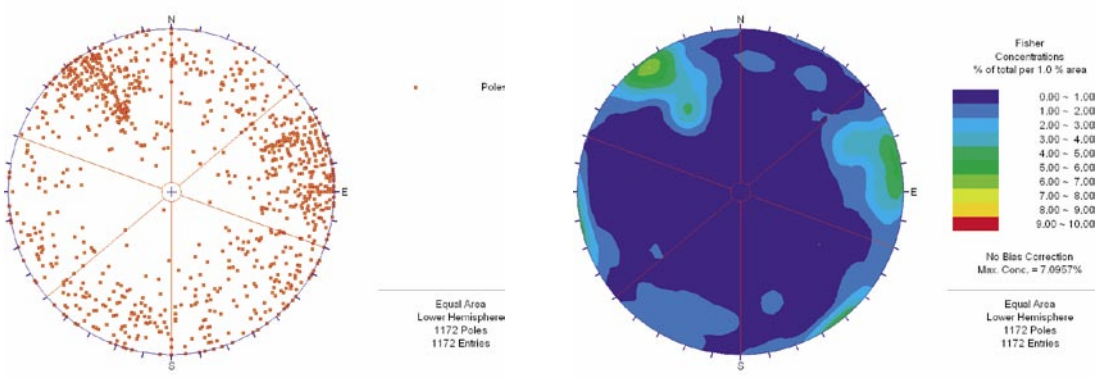

Figure A3-2. *Outcrop asm0000205, stereonets with fracture sets symbolized as red lines.*

Then the fracture dataset is subdivided in three distinct sets, based on the fracture strikes.

The three datasets summarized in the tables below:

For the asm000025

ID	Number	$\%_{total}$	Strike limit	Mean dip – dip direction	K (fisher dispersion)
1w	167	0.18	120 → 160	86/319	9
2w	517	0.57	340 → 75	87/203	4.8
3w	228	0.25	75 → 120	85/280	8.7

For the asm000205

ID	Number	$\%_{total}$	Strike limit	Mean dip – dip direction	K (fisher dispersion)
1w	523	0.45	110 → 180	79/146	8.2
2w	431	0.37	50 → 110	8/259	10.4
3w	218	0.18	110 → 180	89/206	6.6

Length distributions of the different fracture sets

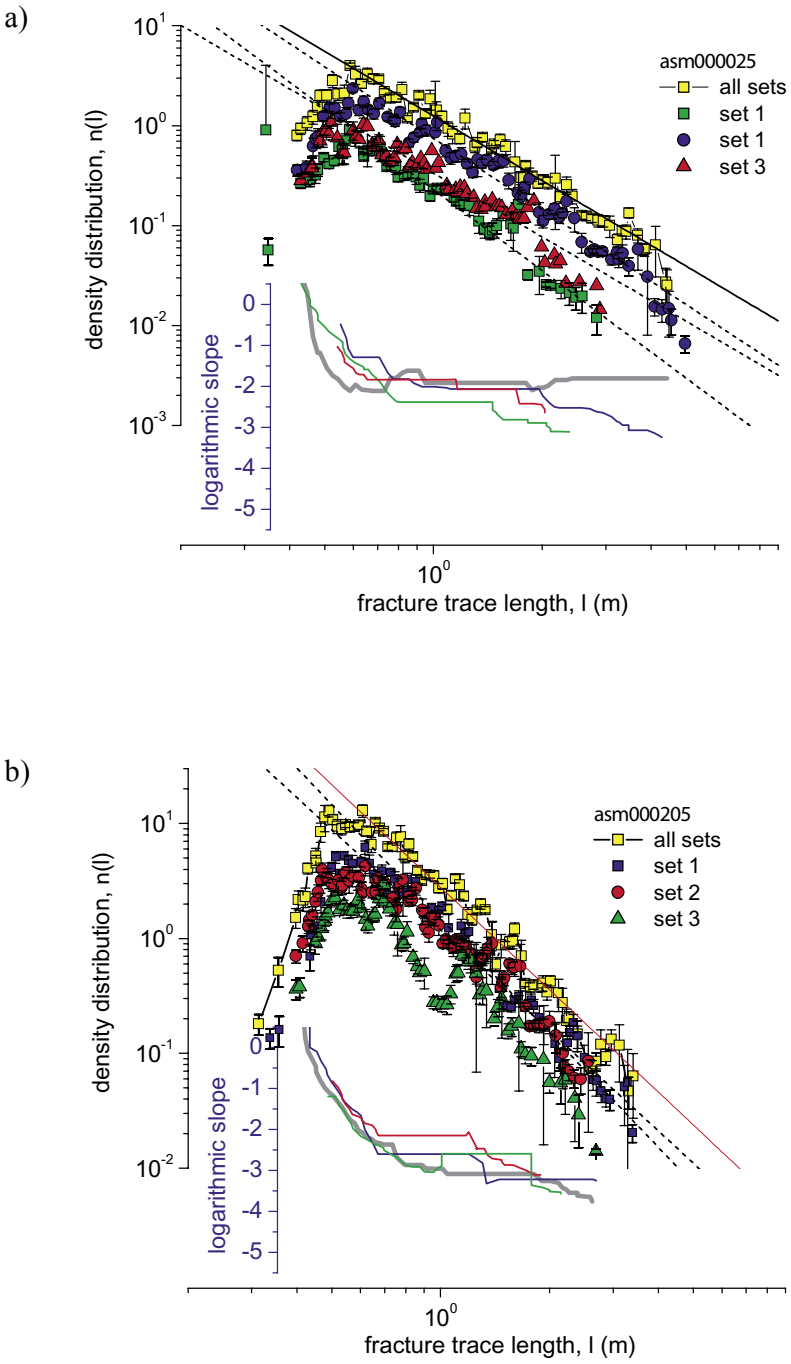

Figure A3-3. *Density distribution for fracture sets defined from a) outcrop asm000025 and b) outcrop asm000205. See main text for detailed explanations.*

Appendix 4

1*d* datasets, frequencies and rock type

What is in this appendix?

In this appendix, we recall what information is stored along boreholes, in particular the fracture intercepts status ("open" and "sealed" related) and rock lithology. Information is displayed under a both global shape (the mean P_{10} values, table next page) and through local variations (frequency diagrams coupled to rock lithology representations) for boreholes KAV01, KLX02, KSH01A, KSH02 and KSH03A.

Note that not all information related to fracture intercepts have been used in the present report; the analysis is restricted to open/sealed characters and to rock lithology (qualitative comparison). *Alteration, mineralization, etc, could not be considered.*

[Source files: rock.xls, freq_1m.xls]

P_{10}, open, sealed

Along boreholes, various "states" of fractures are identified and represented under the following labels:

OPEN_FRAC

OPEN_PARTLY

OPEN_CRUSH

SEALED_FRAC

SEALED_NETWORK

OPEN_FRAC, OPEN_PARTLY and SEALED_FRAC correspond to fracture intercepts clearly identified along the boreholes (with complement of informations like strike, dip etc).

OPEN_CRUSH and SEALED_NETWORK correspond to zones where fracture intercepts can not be identified as unique element. The corresponding local frequency is there estimated.

In the computation of the total number of open or sealed fracture intercepts, crush zones and sealed_network zones can be or not integrated since they do not exactly constitute single identified elements. Therefore we have:

OPEN_TOTAL ("opentot" in Figures below) = OPEN_FRAC + OPEN_PARTLY + OPEN_CRUSH

SEALED_TOTAL ("sealedtot" in Figures below) = SEALED_FRAC + SEALED_ NETWORK

And finally the total amount of identified fractures, open and sealed is expressed through:

FRAC_TOTAL ("tot" in Figures below) = OPEN_FRAC + OPEN_PARTLY + SEALED_ FRAC

For each boreholes, the mean values of P_{10}, corresponding to the different groups defined above, are summarized in Table A4-1, they are also represented in Figure A4-1.

Table A4-1. P_{10} values, in m^{-1}, calculated over full boreholes length, distinctions between open, sealed etc, see text.

	Size (m)	Open frac	Open partly	Open crush	Open total	Sealed frac	Sealed network	Sealed total	Sealed broken	Frac total
HSH01	184	2.83	0.42	0.38	3.63	3.14	0	3.14	0.01	6.39
HSH02	134	4.08	0.17	0	4.25	1.74	0	1.74	0.04	5.99
HSH03	183	1.75	0.26	0.34	2.35	2.16	0	2.16	0.01	4.17
KAV01	740	3.34	0.00	0.45	3.79	2.45	0	2.45	0.28	5.79
KLX01	694	–	–	–	–	–	–	–	–	–
KLX02	802	2.61	0.13	0.34	3.08	1.07	0	1.07	0.27	3.81
KSH01A	896	2.39	0.03	0.07	2.49	8.21	0	8.21	0.94	10.63
KSH01B	93	1.47	0.01	0	1.48	5.72	0	5.72	0.75	7.20
KSH02	979	3.86	0.00	0.72	4.58	8.23	0	8.23	1.51	12.09
KSH03A	880	2.40	0.01	0.16	2.57	4.09	3.89	7.98	0.87	6.50
KSH03B	99	1.30	0.02	0	1.32	6.55	0.05	6.60	2.11	7.87

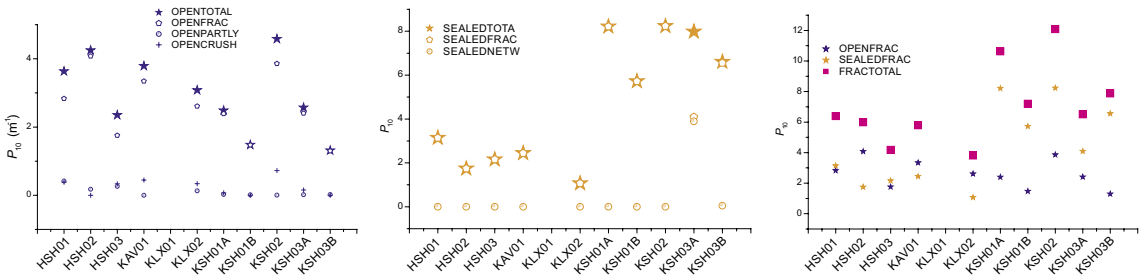

Figure A4-1. *Mean P10 for boreholes. On left for open fractures and crush zones, middle for sealed fracture and network and right direct comparison between sealed, open and open+sealed fractures intercepts frequencies.*

Local variations along boreholes

We present here local variations of P_{10} and rock lithologies, for boreholes KAV01, KLX02, KSH01A, KSH02, KSH03A. The frequencies diagrams are build as follows:

curves labelled “cumopento”, “cumsealed” and “cumtot”, thick lines, respectively black, red and green, are joined to the right y axis. They correspond to cumulative of the values defined above :

OPEN_TOTAL = OPEN_FRAC + OPEN_PARTLY + OPEN_CRUSH

SEALED_TOTAL = SEALED_FRAC + SEALED_NETWORK

FRAC_TOTAL = OPEN_FRAC + OPEN_PARTLY + SEALED_FRAC

Joined to the left axis, are the local variations of the number of elements per meter (thin lines), corresponding to the cumulatives described just above (same color code). Curves are not direct variations of the number of fractures counting per meter, but smoothed curves build by adjacent averaging over 30 points.

A representation of rock type variations along the boreholes is place next to each frequency diagram.

KAV01

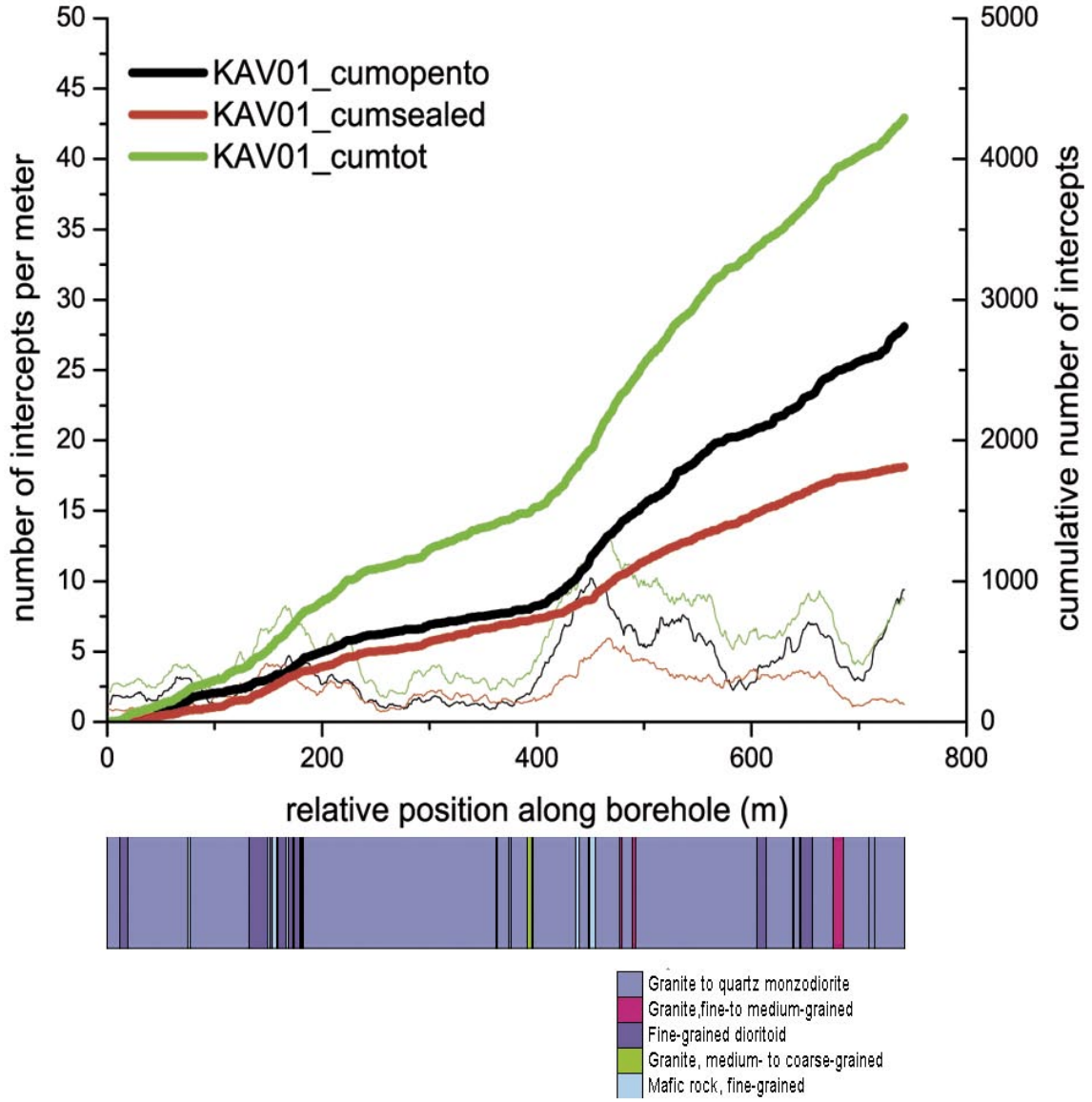
KAV01_cumopento
KAV01_cumsealed
KAV01_cumtot
number of intercepts per meter
cumulative number of intercepts
relative position along borehole (m)
0
200
400
600
800
0
5
10
15
20
25
30
35
40
45
50
0
1000
2000
3000
4000
5000
Granite to quartz monzodiorite
Granite,fine-to medium-grained
Fine-grained dioritoid
Granite, medium- to coarse-grained
Mafic rock, fine-grained

KLX02

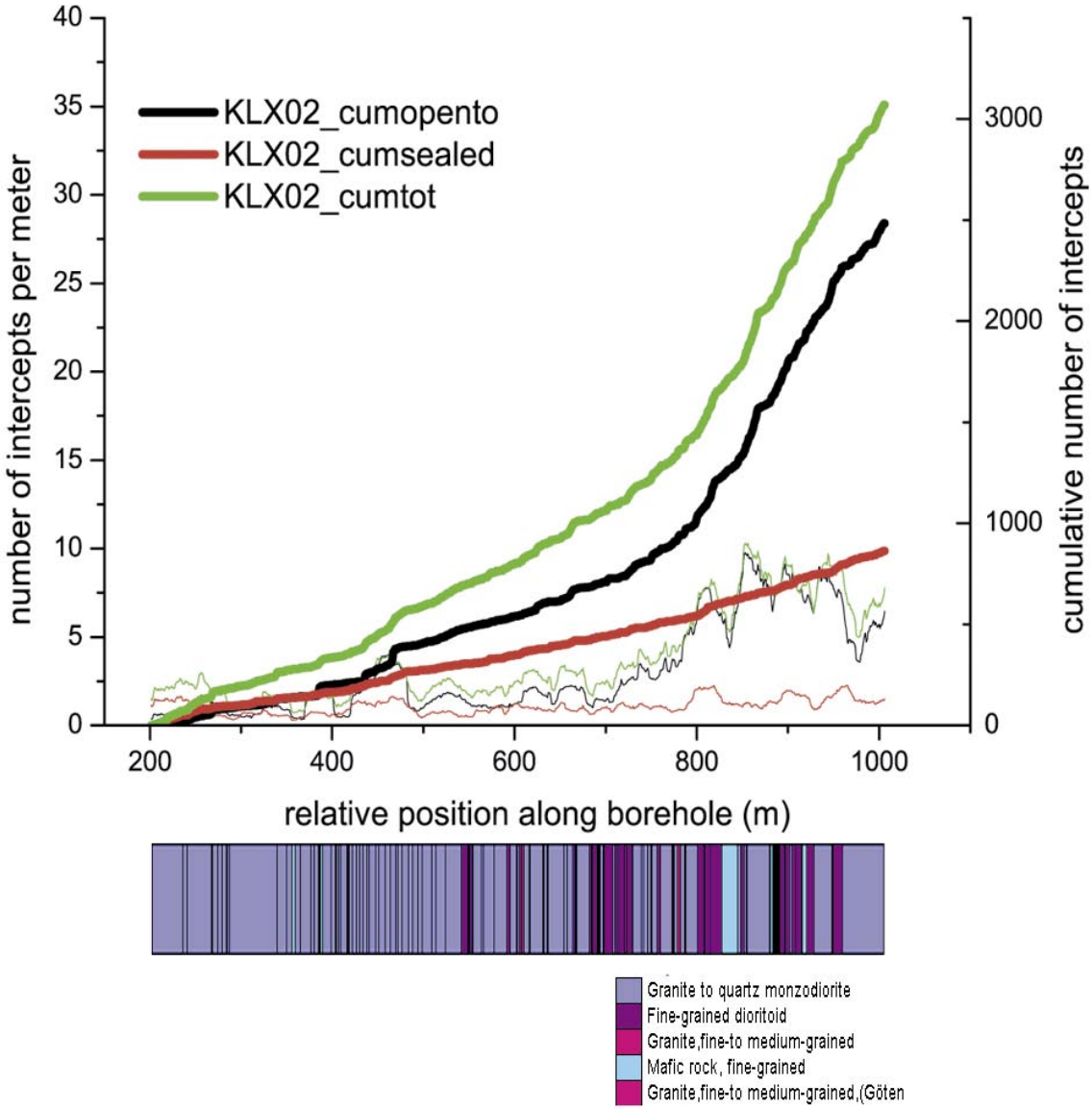
KLX02_cumopento
KLX02_cumsealed
KLX02_cumtot
number of intercepts per meter
cumulative number of intercepts
relative position along borehole (m)
0
5
10
15
20
25
30
35
40
0
1000
2000
3000
200
400
600
800
1000
Granite to quartz monzodiorite
Fine-grained dioritoid
Granite,fine-to medium-grained
Mafic rock, fine-grained
Granite,fine-to medium-grained,(Göten

KSH01A

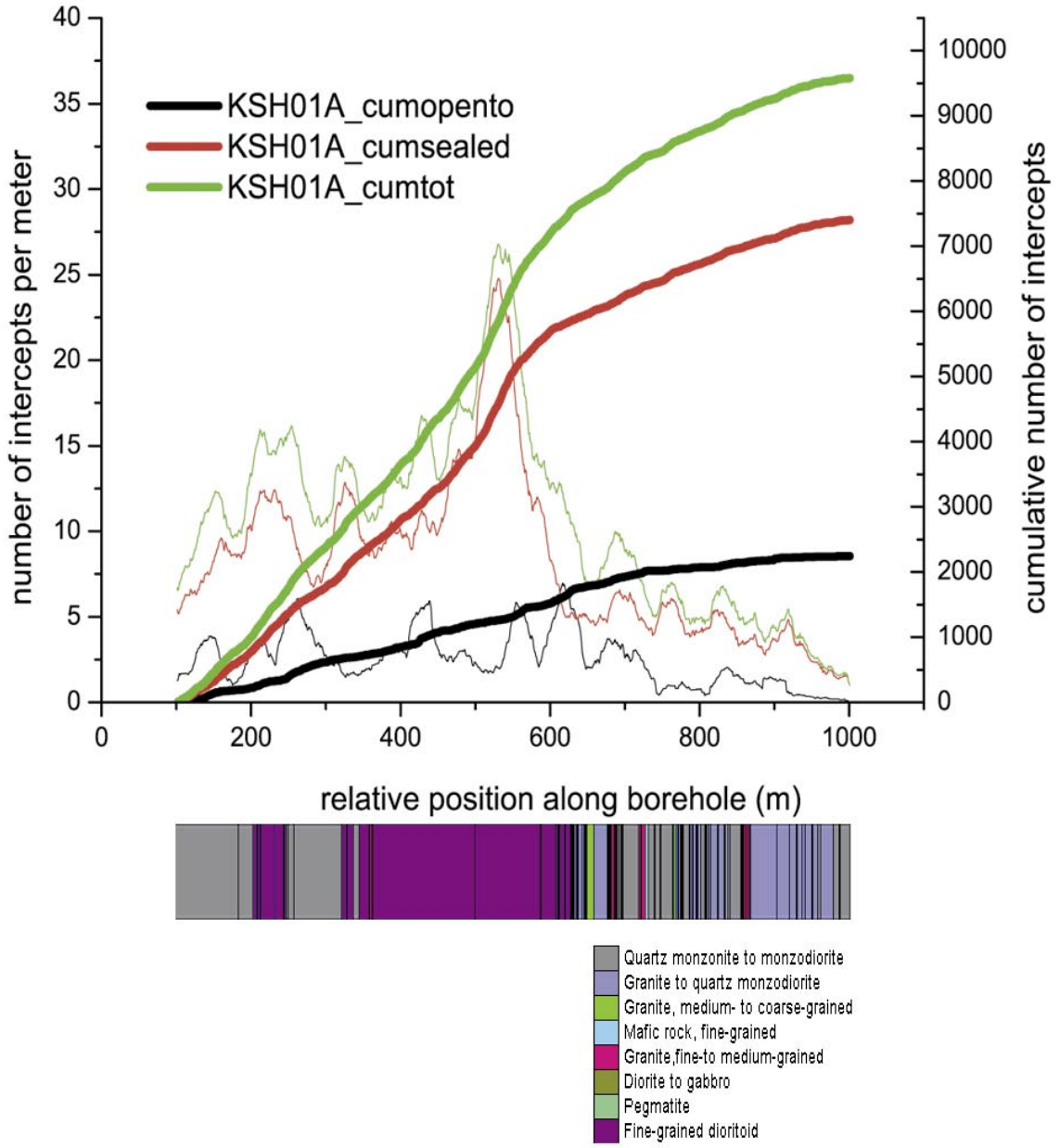
KSH01A_cumopento
KSH01A_cumsealed
KSH01A_cumtot
number of intercepts per meter
cumulative number of intercepts
relative position along borehole (m)
0
200
400
600
800
1000
0
5
10
15
20
25
30
35
40
0
1000
2000
3000
4000
5000
6000
7000
8000
9000
10000
Quartz monzonite to monzodiorite
Granite to quartz monzodiorite
Granite, medium- to coarse-grained
Mafic rock, fine-grained
Granite,fine-to medium-grained
Diorite to gabbro
Pegmatite
Fine-grained dioritoid

KSH02

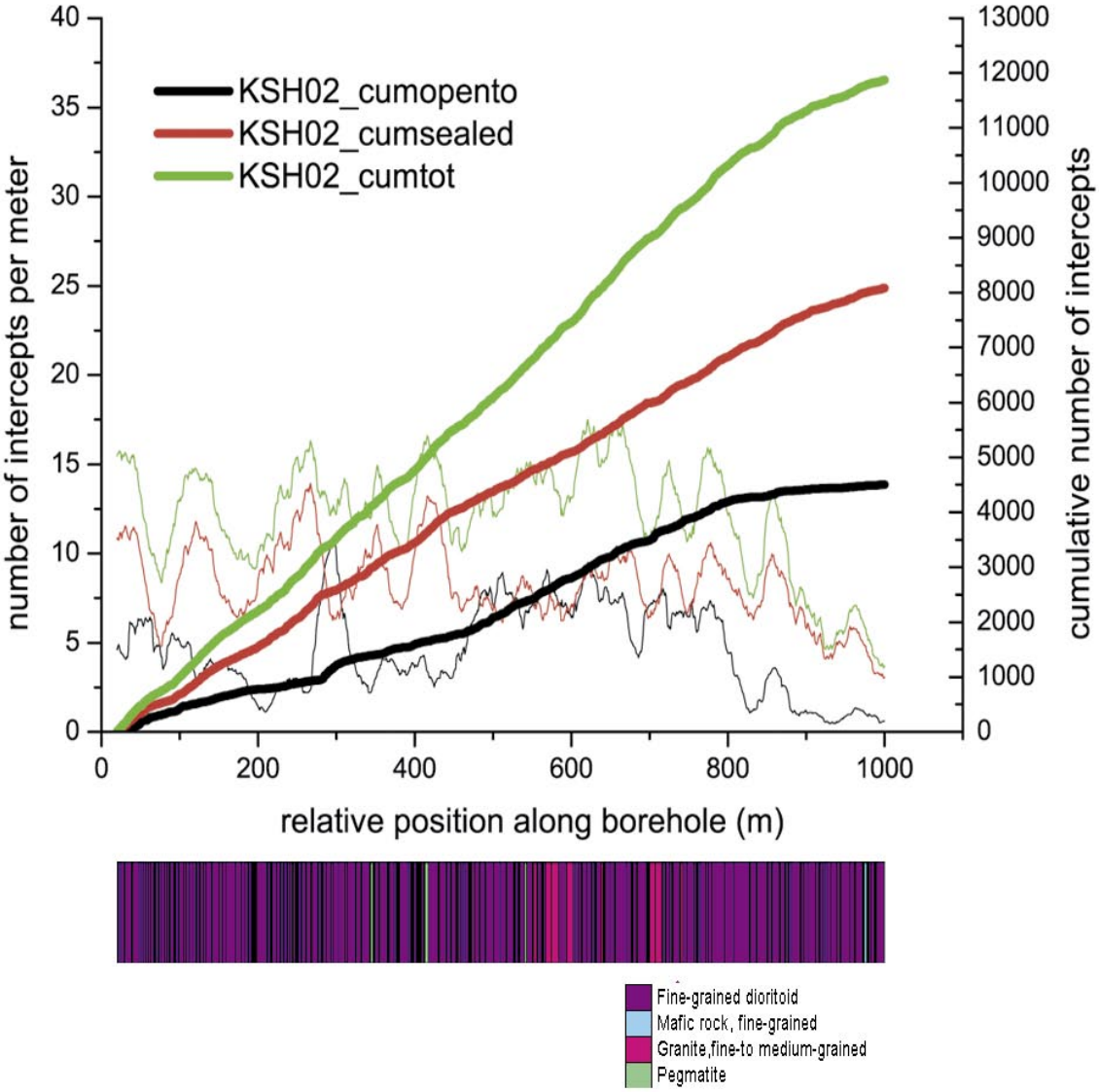
KSH02_cumopento
KSH02_cumsealed
KSH02_cumtot
number of intercepts per meter
cumulative number of intercepts
relative position along borehole (m)
0
5
10
15
20
25
30
35
40
0
1000
2000
3000
4000
5000
6000
7000
8000
9000
10000
11000
12000
13000
0
200
400
600
800
1000
Fine-grained dioritoid
Mafic rock, fine-grained
Granite,fine-to medium-grained
Pegmatite

KSH03A

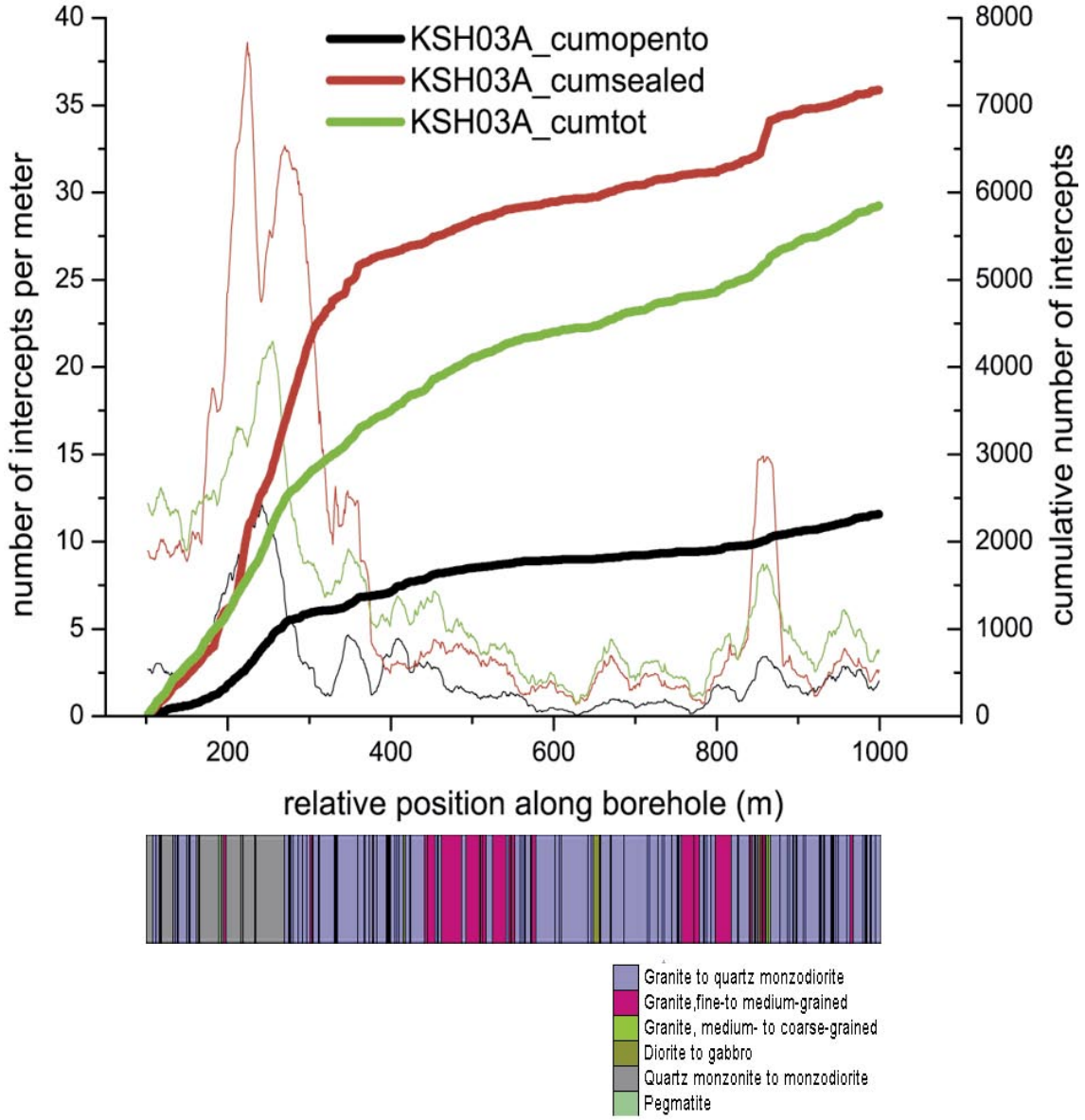
KSH03A_cumopento
KSH03A_cumsealed
KSH03A_cumtot
number of intercepts per meter
cumulative number of intercepts
relative position along borehole (m)
0
5
10
15
20
25
30
35
40
0
1000
2000
3000
4000
5000
6000
7000
8000
200
400
600
800
1000
Granite to quartz monzodiorite
Granite,fine-to medium-grained
Granite, medium- to coarse-grained
Diorite to gabbro
Quartz monzonite to monzodiorite
Pegmatite

Appendix 5

Fracture orientations for DFN generation

For the DFN simulations of validation performed in section **3d Scaling Model**, bootstrapped orientation distributions were used.

The bootstrapped orientations files can be used to assess numerically the role of specific orientations distributions extracted from the different datasets or to simply reproduce exactly local orientations distributions at local scales.

The bootstrapped orientation files encompass the orientation bias (Terzaghi correction is applied). One orientation dataset is sampled through regular bin sizes in (θ,φ), with a bin size equal to 15°. A weight is applied to each bin, as the mean Terzaghi correction to be applied over the bin. The bootstrapped distribution is finally normalized to one so that orientations can be directly picked up within the distribution.

Having a constant bin size in θ and φ (fracture poles expressed in spherical angles) lead to a bin size variation in solid angle. This effect does not entail however bias effect at a scale larger than the largest bin size.

Bootstrapped files for the *asm*000025, *asm*000026, *asm*0000205, *asm*0000206, KAV01, KSH01A, KSH02 and KSH0A are available under ASCII format, with the following format:

Column 1 (“strike”): strike coordinate of the bin middle.

Column 2 (“dip”): dip coordinate of the bin middle.

Column 3 (“pdf”): local value of the density probability function.

Note that the pdf functions can be simply combined.

Appendix 6

1*d* datasets, fractal correlation

What is in the appendix?

Here we simply put all the figures related to analyses performed to measure the fractal dimension, for each borehole. The classical representation is chosen to represent the integral of correlation C(r) (see main text for an explanation). Three figures per page summarize one borehole. All boreholes are represented (HSH01, HSH02, HSH03, KAV01, KLX01, KLX02, KSH01A, KSH01B, KSH02, KSH03A and KSH03B. General results about fractal dimensions D_{1d} measured on the fracture intercepts along boreholes are provided in the report.

Layout

The layout is organised as follows:

- top figure representing C(r) calculated for the all (= open + sealed, in green) and the all_randomized (blue) fractures intercepts,
- middle figure representing the ratio of $C(r)/C(r)_{randomized}$ for all fractures intercepts,
- bottom figure representing C(r) calculated for the open (black), sealed (red), and all (= open + sealed, in green) fractures intercepts.

HSH01

All-, all_randomized-

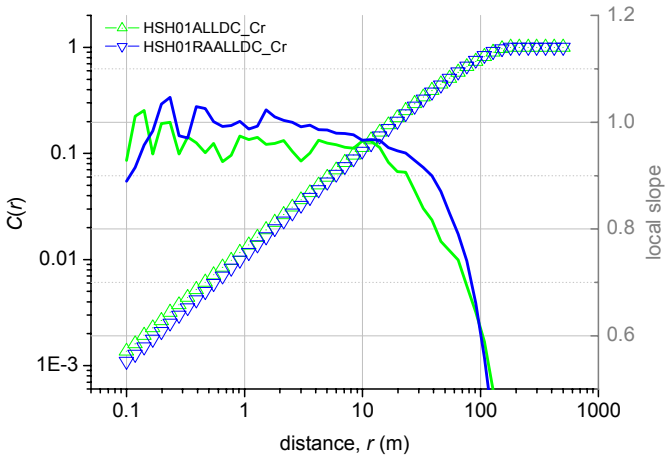

Ratios

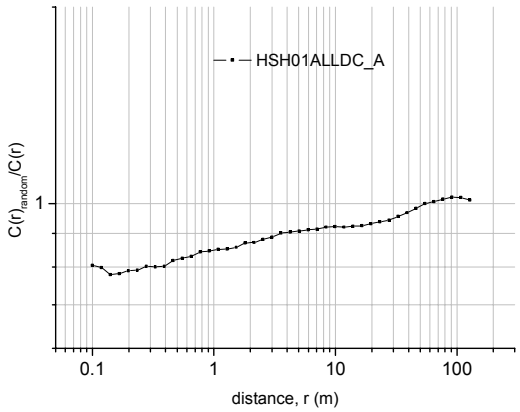

Open-, -sealed-, all-

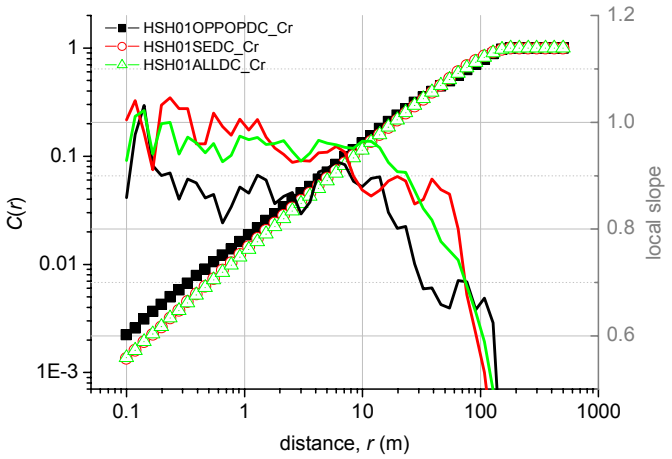

HSH02

All-, all_randomized-

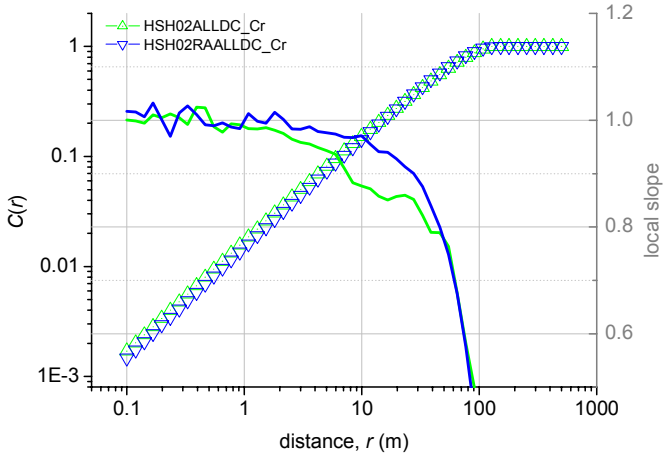

Ratios

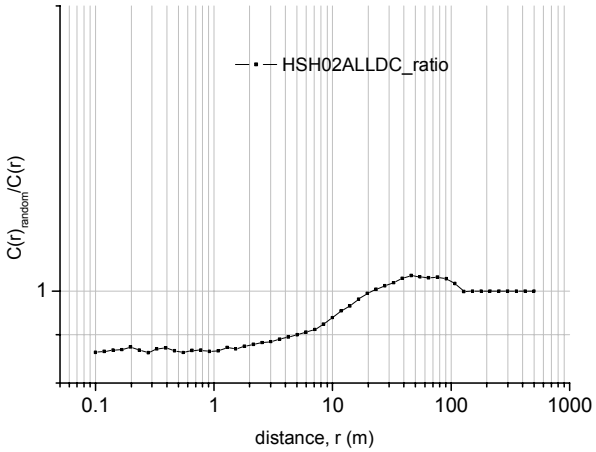

Open-, -sealed-, all-

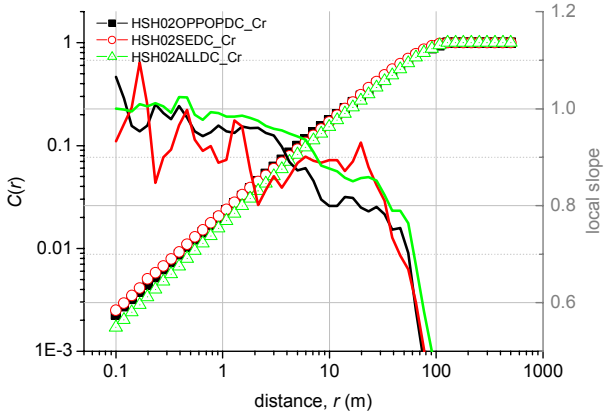

HSH03

All-, all_randomized-

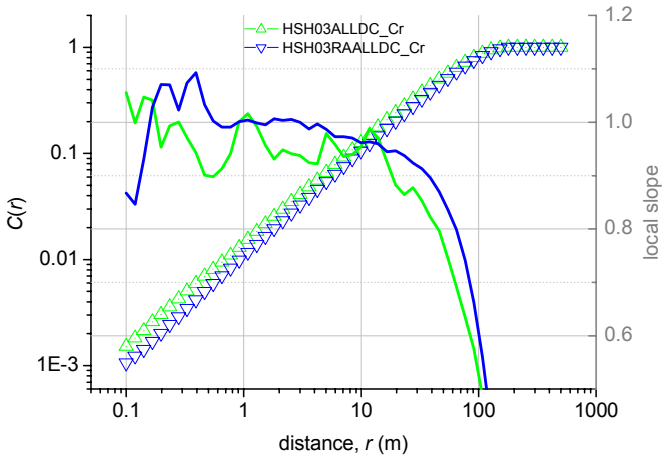

Ratios

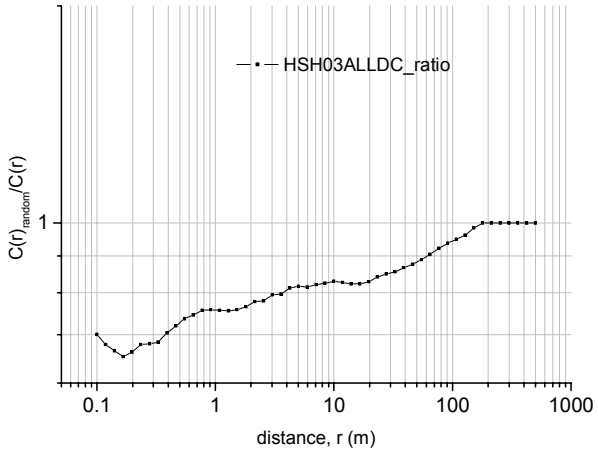

Open-, -sealed-, all-

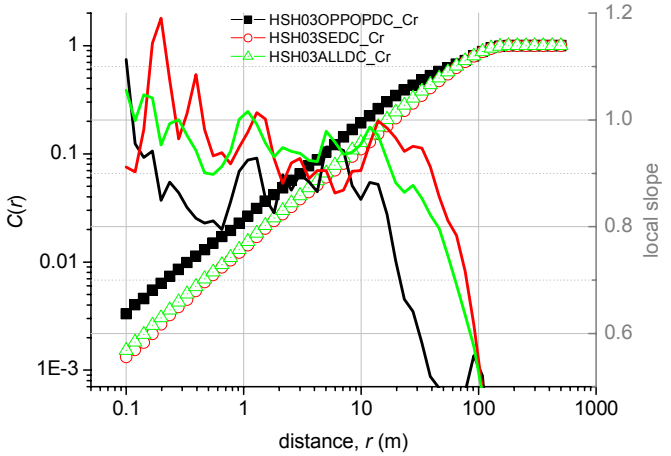

KAV01

All-, all_randomized-

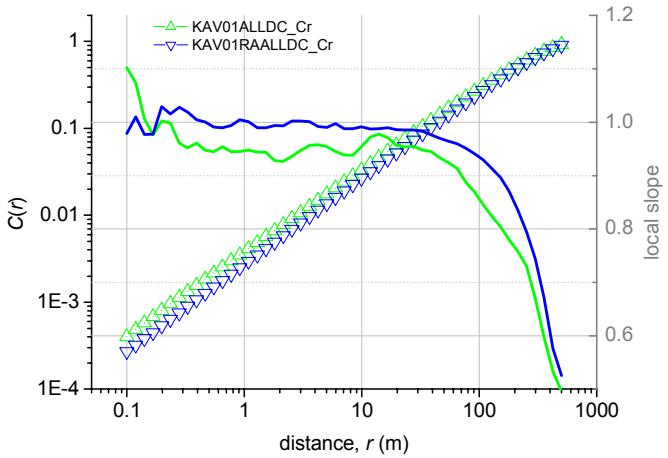

Ratios

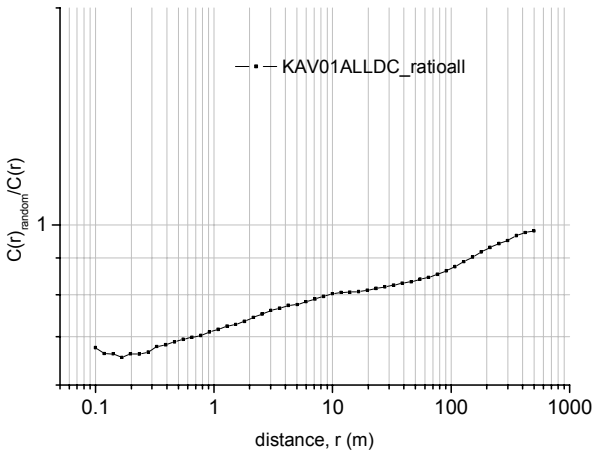

Open-, -sealed-, all-

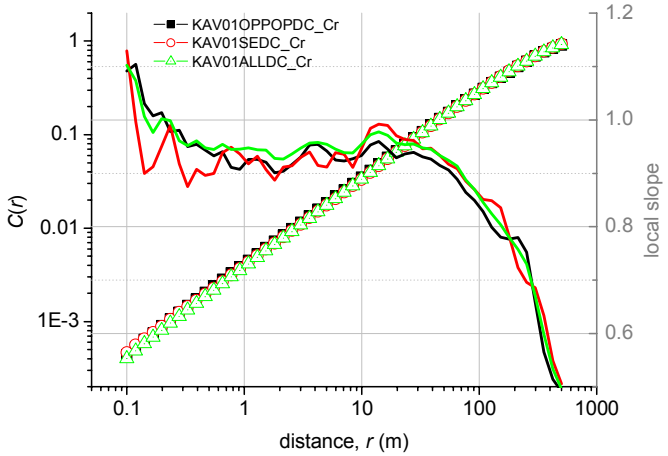

KLX01

All-, all_randomized-

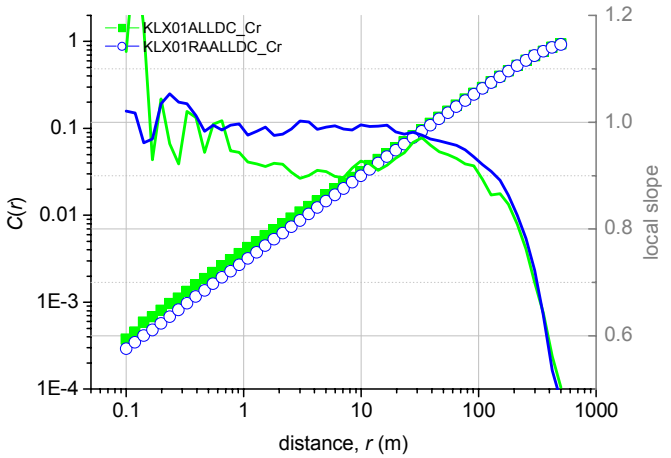

Ratios

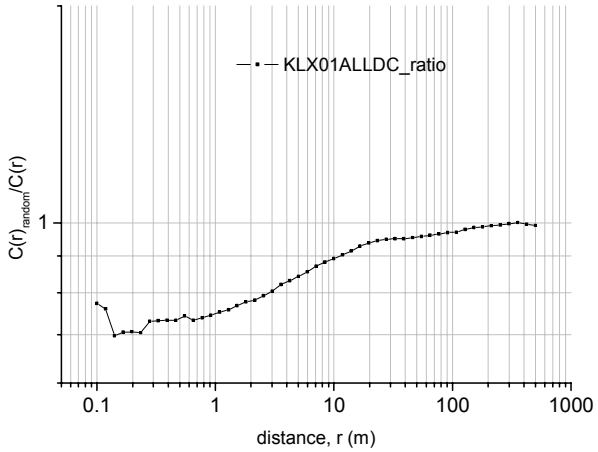

Open-, -sealed-, all-

No data.

KLX02

All-, all_randomized-

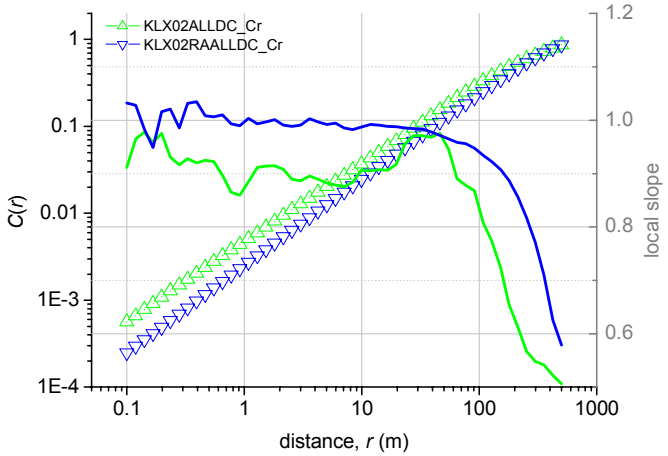

Ratios

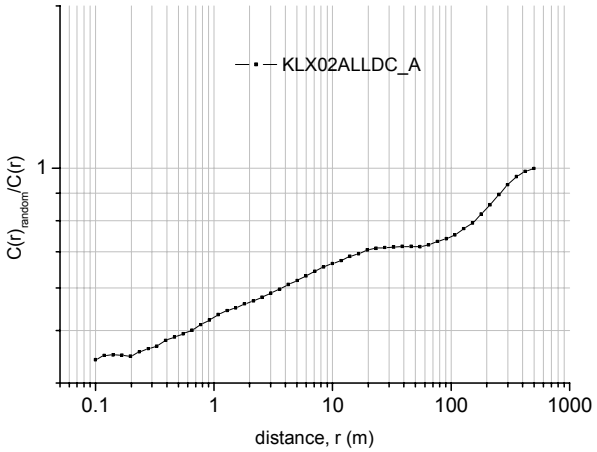

Open-, -sealed-, all-

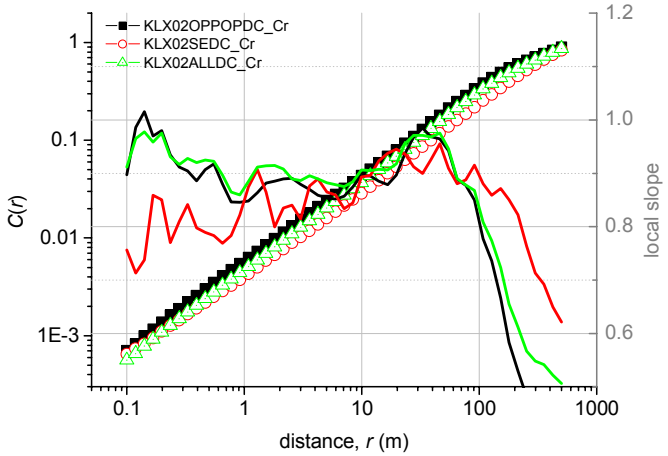

KSH01A

All-, all_randomized-

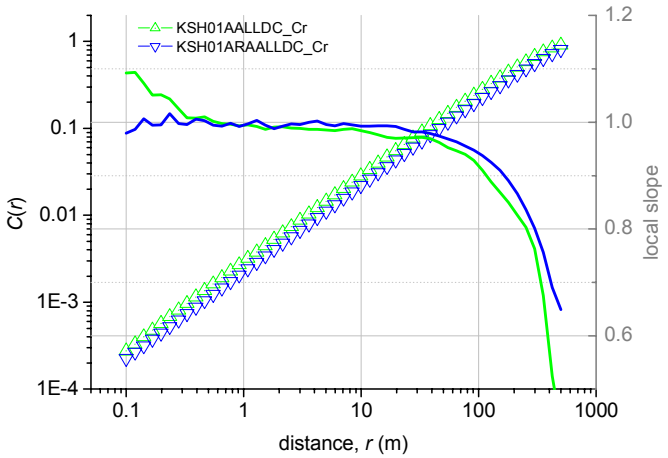

Ratios

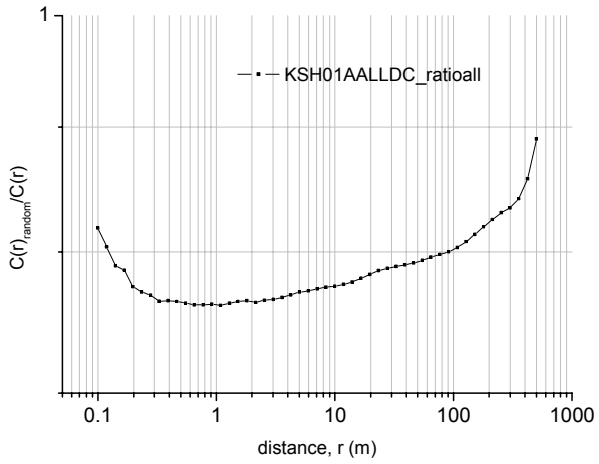

Open-, -sealed-, all-

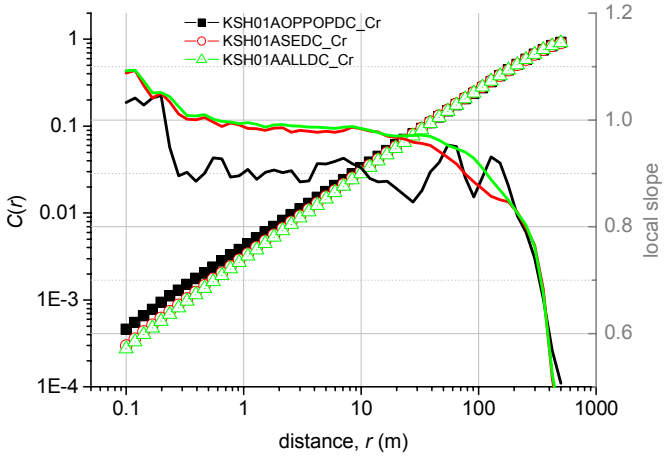

KSH01B

All-, all_randomized-

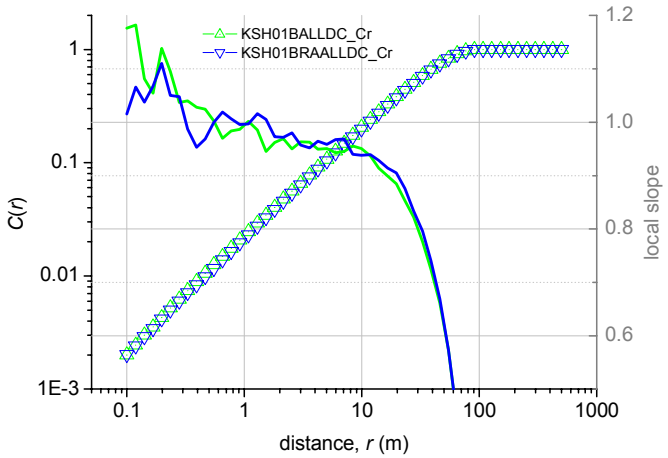

Ratios

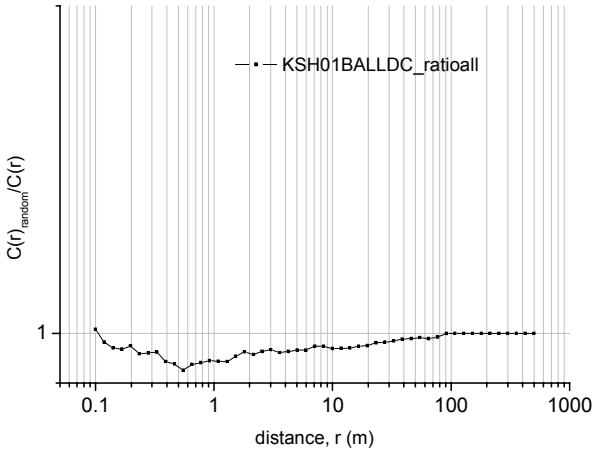

Open-, -sealed-, all-

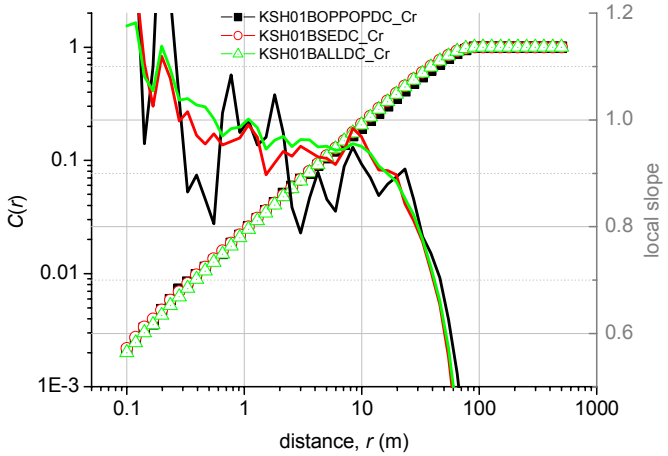

KSH02

All-, all_randomized-

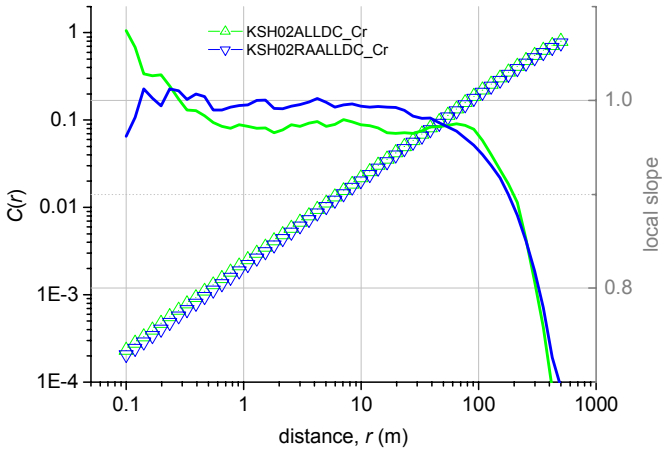

Ratios

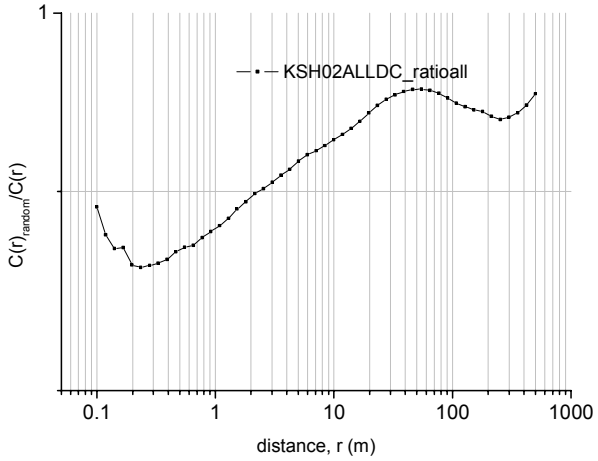

Open-, -sealed-, all-

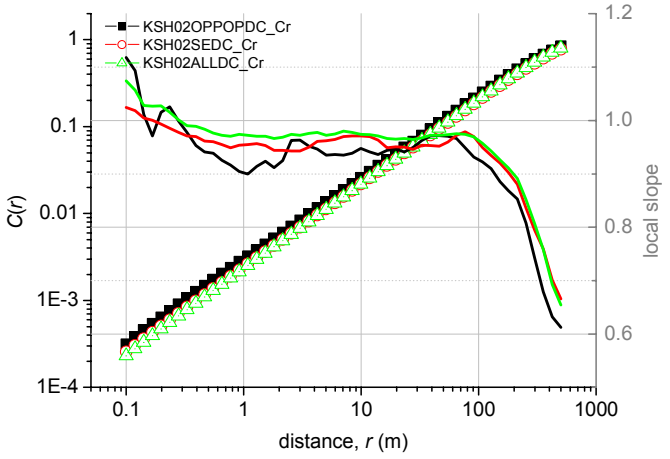

KSH03A

All-, all_randomized-

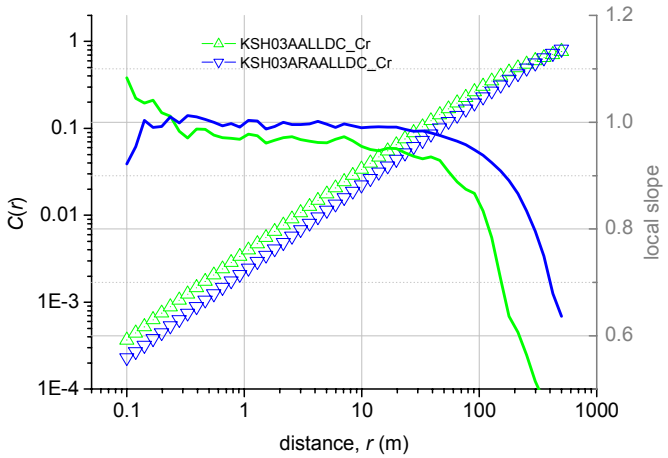

Ratios

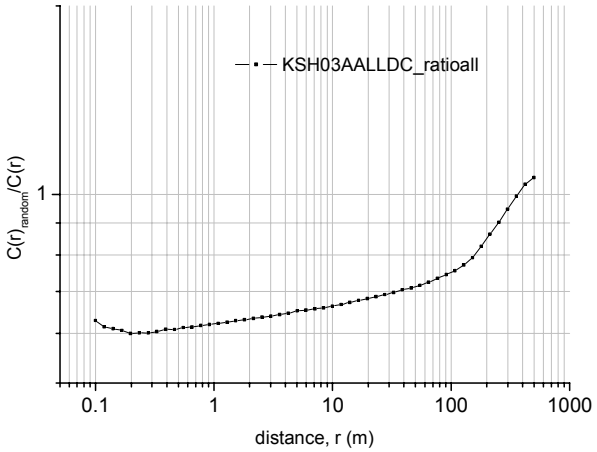

Open-, -sealed-, all-

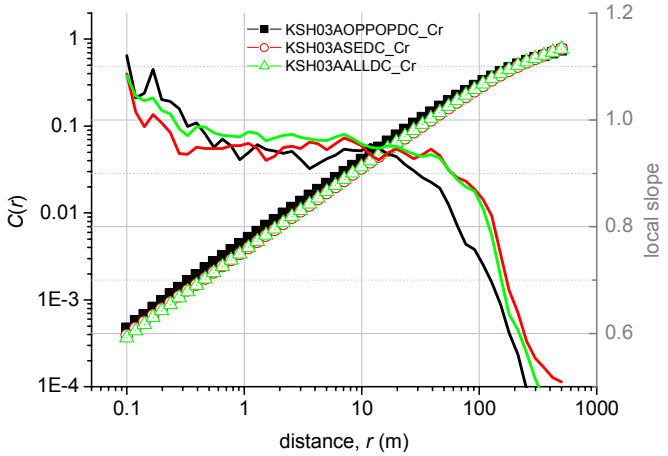

KSH03B

All-, all_randomized-

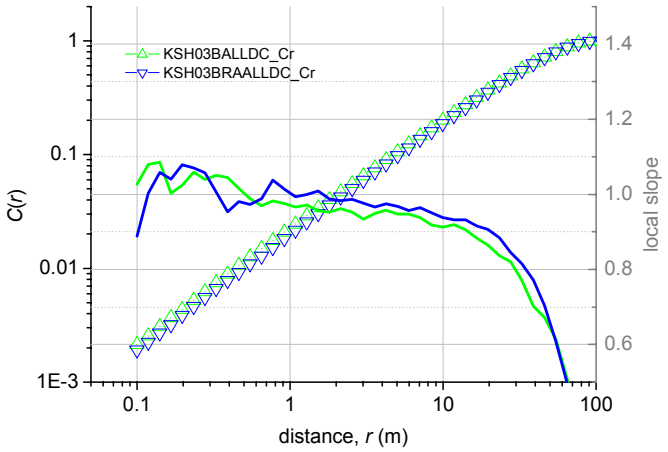

Ratios

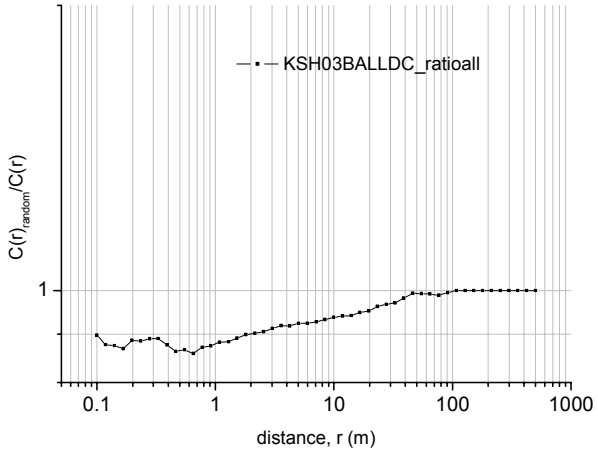

Open-, -sealed-, all-

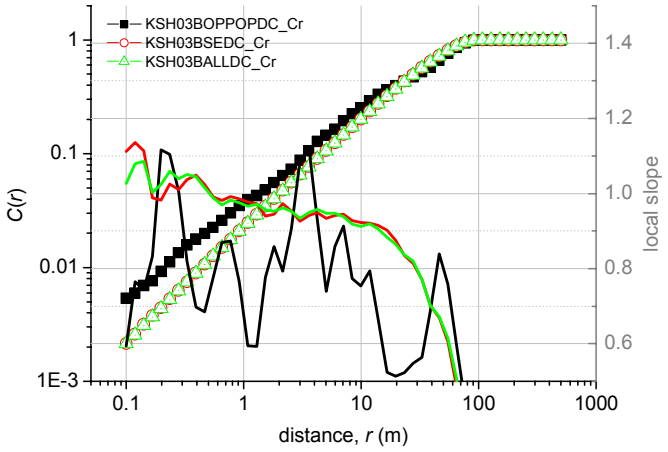

Appendix 7

Data “imprecision”

During the analysis, some data errors appeared, they are listed below:

Impossible values

File name and location	Id	
SDEADM_GOL_OH_GEO_1921	ASM000025582	strike: 1195
SDEADM_GOL_OH_GEO_1921	ASM000025347	strike: 386
SDEADM_GOL_OH_GEO_1918	ASM000026475	Strike: 382
SDEADM_GOL_OH_GEO_1918	ASM00002664	Strike: 784
SDEADM_GOL_OH_GEO_1918	ASM00002642	Strike: 362
SDEADM_GOL_OH_GEO_1915	ASM000205847	Dip: 777
Rock_modified.xls	KSH01B KSH02 KSH03A	”core-logging” is ok, but why the ”core-logging preliminary” are in the same file?
Rock_modified.xls	KSH02	Some zones have a zero thickness or some zones are missing. One line gives 526.01 526.01, in field ADJUSTEDSECUP (m) and ADJUSTEDSECLOW (m). And the rank 526.01 to 527.1 is missing. then remove the line 526.01 526.01. remove the line 98.97 98.97. remove the line 458 458,

Boreholes start and end positions

Boreholes lengths, at which depth/position exactly does the sampling initiate and finish, does this correspond to first and last intercept positions?

FEATURE rocktype, what is in rock_occur.xls.

In file rock.xls and rock_occur.xls.

Up to now we have been using rock.xls (containing the field FEATURE and value rock-type), is this bad? What is rock_occur.xls. (see some details below).

In the datafiles, I found a:

rock.xls file, with a field FEATURE = rocktype,

rock_occur.xls, with a field VARCODE = Rock occurrence,

the respective NAME_CODE fields share common values, but not exactly the same for a given borehole.

For instance, for HSH01 and NAME_CODE = 501058, both files provides different sections positions.

rock_occur.xls provides:

HSH01	Rock occurrence	112.97	113.07	0	Unspecified	501058	Granite, medium- to coarse-grained
HSH01	Rock occurrence	113.78	113.86	0	Unspecified	501058	Granite, medium- to coarse-grained
HSH01	Rock occurrence	115.81	115.87	0	Unspecified	501058	Granite, medium- to coarse-grained
HSH01	Rock occurrence	118.24	118.32	0	Unspecified	501058	Granite, medium- to coarse-grained

and

rock.xls provides:

Id code	Adjusted secup (m)	Adjusted seclow (m)	Feature	Name	Name_code
HSH01	104.41	108.63	RockType	Granite, medium- to coarse-grained	501058
HSH01	41.60	45.77	RockType	Granite, medium- to coarse-grained	501058
HSH01	109.64	118.05	RockType	Granite, medium- to coarse-grained	501058
HSH01	120.81	133.88	RockType	Granite, medium- to coarse-grained	501058

Core logging, preliminary – BOREMAP

In file rock.xls:

Core logging, preliminary – BOREMAP.

Core logging - BOREMAP/BIPS.

Why are the preliminary results provided?